

Fall 12-2021

Shipboard Lidar as a Tool for Remotely Measuring the Distribution and Bulk Characteristics of Marine Particles

Brian Leigh Collister
Old Dominion University, bcoll018@odu.edu

Follow this and additional works at: https://digitalcommons.odu.edu/oeas_etds



Part of the [Geographic Information Sciences Commons](#), [Oceanography Commons](#), [Physics Commons](#), and the [Remote Sensing Commons](#)

Recommended Citation

Collister, Brian L.. "Shipboard Lidar as a Tool for Remotely Measuring the Distribution and Bulk Characteristics of Marine Particles" (2021). Doctor of Philosophy (PhD), Dissertation, Ocean & Earth Sciences, Old Dominion University, DOI: [10.25777/bt06-xm51](https://doi.org/10.25777/bt06-xm51)
https://digitalcommons.odu.edu/oeas_etds/183

This Dissertation is brought to you for free and open access by the Ocean & Earth Sciences at ODU Digital Commons. It has been accepted for inclusion in OES Theses and Dissertations by an authorized administrator of ODU Digital Commons. For more information, please contact digitalcommons@odu.edu.

**SHIPBOARD LIDAR AS A TOOL FOR REMOTELY MEASURING THE
DISTRIBUTION AND BULK CHARACTERISTICS OF MARINE PARTICLES**

by

Brian Leigh Collister
B.S. December 2016, Old Dominion University
M.S. May 2019, Old Dominion University

A Dissertation Submitted to the Faculty of
Old Dominion University in Partial Fulfillment of the
Requirements for the Degree of

DOCTOR OF PHILOSOPHY

OCEANOGRAPHY

OLD DOMINION UNIVERSITY
December 2021

Approved by:

Richard C. Zimmerman (Director)

Victoria J. Hill (Member)

Charles I. Sukenik (Member)

William M. Balch (Member)

ABSTRACT

SHIPBOARD LIDAR AS A TOOL FOR REMOTELY MEASURING THE DISTRIBUTION AND BULK CHARACTERISTICS OF MARINE PARTICLES

Brian Leigh Collister
Old Dominion University, 2021
Director: Dr. Richard C. Zimmerman

Light detection and ranging (lidar) can provide remote estimates of the vertical distribution of optical properties in the ocean, potentially revolutionizing our ability to characterize the spatial structure of upper ocean ecosystems. However, challenges associated with quantifying the relationship between lidar measurements and biogeochemical properties of interest have prevented its adoption for routinely mapping the vertical structure of marine ecosystems. To address this, we developed a shipboard oceanographic lidar that measures attenuation (α) and linear depolarization (δ) at scales identical to those of in-water optical and biogeochemical measurements. The instrument's ability to resolve the distribution of optical and biogeochemical properties was characterized during a series of field campaigns in the Mid-Atlantic Bight (MAB) and Gulf of Maine (GoM). α resolved vertical and horizontal gradients in absorption and chlorophyll concentration associated with the Chesapeake Bay outflow and distinct water masses in the GoM. δ was related to the particulate backscattering ratio, an optical proxy for particle size and composition, suggesting that δ could provide information on the material properties of marine particles. After initial characterizations, we conducted a 13-day deployment in the GoM and western North Atlantic to sample a mesoscale coccolithophore bloom. Bloom features were mapped at sub-kilometer scales and δ was used to distinguish coccoliths/coccolithophores from non-calcified particles. Finally, a model parameterized with in-water optical measurements from the bloom and laboratory linear depolarization measurements was used to explore the influence of

multiple scattering and particle characteristics on measurements of δ . Single scattering measurements of δ exhibited a complex dependency on particle shape, size, and composition that was consistent with scattering calculations for non-spherical particles. Model results suggested that variability in δ was driven predominantly by shifts in particle concentration rather than their bulk characteristics. However, the behavior of δ when backscattering became decoupled from calcite could only be reproduced by including a separate coccolith particle class. Taken as a whole, this work provides new insights into the scattering nature of marine particles and the complex response of the lidar return signal to water column optical properties, and is an important demonstration of the sampling capabilities afforded by shipboard lidar.

Copyright, 2021, by Brian Leigh Collister, All Rights Reserved

To Ashlee, Sandwich, and Rufus

ACKNOWLEDGEMENTS

The work presented here and my advancement as a scientist and as a human being would not have been possible without the help of many important people. I would like to start out by expressing my deepest appreciation to Dr. Richard Zimmerman for his insightfulness and patience while serving as my mentor and advisor. From the first day that I walked into his office as a wandering undergraduate, Dick treated me as a colleague and gave me the confidence that I needed to grow as a scientist. Thank you for always leaving your door and your whiteboard open, for sharing your experience but giving me room to learn by trial and error, and for being patient when error resulted in trips to urgent care, overnight shipments, and instruments slipping their moorings. I have had a blast working with you, and I hope to continue doing so into the future.

I am also indebted to the members of my dissertation committee, Dr. Victoria Hill, Dr. Charles Sukenik, and Dr. William “Barney” Balch, for their valuable insight and support throughout my time as a graduate student. Victoria had a knack for pulling me out of the weeds whenever I was stuck on a problem and couldn’t see the bigger picture. Thank you for listening to me ramble about lidar when Dick was nowhere to be found, for being my seagrass counting buddy, and for always being in the perfect place to photograph that duck-face I always seem to make when I am diving. Charles provided a unique perspective on optics, electronics, and problem solving, and his excellent sense of humor cut through frustrating moments like a hot knife through butter. Thanks for putting up with the chaotic energy of us oceanographers and for trusting us to throw your shiny optics bits into the deep, dark, corrosive ocean. Barney was an inexhaustible fountain of knowledge and scientific energy throughout the entirety of my PhD work. His excitement for science is contagious, and he felt like my biggest fan every time we met to discuss results or to

plan a trip. Thank you for being so supportive of my work, for inviting me to participate in your field campaigns, and especially for “holding the boat” when I forgot to pack the lidar cables.

David Ruble deserves a special thanks for his work in constructing the wacky contraptions that we threw his way and for ensuring that we collected the highest quality optical data on all of our research excursions. Your attention to detail is unmatched by anyone I know, and I have learned so many practical skills from working with you. Thanks to the BORG crew Austin, Billur, Carmen, and Malee for your friendship and your thoughts, and for providing conversation and mental distraction when it was needed the most. Thanks especially to Malee for being an impeccable friend and neighbor, and for spoiling Sandwich when Ashlee and I caught the travel bug. I thank Adrien Flouros, Jacob Bushey, and Rhianne Cofer, and Jason Boynewicz for their assistance in the lab and for their patience with me as I developed my skills as a mentor.

Thanks goes out to the hard-working ships’ crew and research technicians that supported our science. Many thanks to Bruce Bowler and David Drapeau for ensuring the successful collection of discrete and underway optical data during the GNATS and CoccoMix expeditions. Thanks to Chris Powell, who played a critical role in packaging the lidar system, and to the crew of R/V *Fay Slover*, Richard Cox, Curtis Barnes, and Rebecca Ostman, for supporting the research expeditions into the Mid-Atlantic Bight. Thanks to the crew of R/V *Endeavor* for their support during the CoccoMix expedition, and especially to Oscar Sisson for his help with wrestling “the Beast” from the bow for repairs when our data were on the line.

None of this work would have been possible without my wife, Ashlee, who has loved and supported me unconditionally for the past 10 years. Ashlee has been a caring and unwavering source of positive energy and encouragement in my life, and she has guided me through some incredibly challenging times. I cannot thank you enough for the support that you have provided

me through this process and the sacrifices that you have made in doing so. Thank you for driving on road trips so that I could write in the car, for always reminding me to bring a lunch to the lab, for putting up with books and papers being strewn about the house, and for accompanying me to conferences even if I was working most of the time. I love you dearly.

I would also like to thank my friends and family for sticking by my side throughout this process. A special thanks goes out to Ric, Danya, and Rufus for keeping their door (and refrigerator door) open for Ashlee and me whenever we needed company or a break from the world. Thanks to Jeremy and Clayton for putting up with me as their weird science friend and for keeping me based in the real world all these years. Thanks goes out to Brett for being my early morning surf buddy and a dumping-ground for my stupid jokes, and for teaching me about the importance of a good red wine.

Financial support for this work was provided by the National Science Foundation (OCE-1635403, 1635748), the National Aeronautics and Space Administration (80NSSC19K0043, NNX14AL92G, NNX14AQ41G, NNX14AQ43A, NNX17AH01G, and NNX17AI77G), the National Oceanic and Atmospheric Administration Small Business Innovation Research Program (NA20OAR0210098, NA21OAR0210098), and the Virginia Research Investment Fund. The Old Dominion University Department of Ocean and Earth Science provided ship-time aboard R/V *Fay Slover* and supported me as a teaching assistant during my first year of graduate school. The work presented in Chapter II was conducted while I was supported in-part by the Neil and Susan Kelley Endowed Scholarship. Work presented in Chapters III and IV was conducted while I was supported in-part by the Virginia Space Grant Graduate Research Fellowship Program. The Dorothy Brown Smith travel scholarship administered by the Old Dominion University

Department of Ocean and Earth Sciences provided several excellent opportunities for me to present my research at national and global professional conferences.

TABLE OF CONTENTS

	Page
LIST OF TABLES.....	xi
LIST OF FIGURES	xii
 Chapter	
I. INTRODUCTION.....	1
BACKGROUND	1
STUDY OBJECTIVES.....	7
II. LIDAR CHARACTERIZATION IN THE MID-ATLANTIC BIGHT AND GULF OF MAINE	11
PREFACE	11
INTRODUCTION	11
METHODS	12
RESULTS	22
DISCUSSION	34
III. INSIGHTS FROM A MESOSCALE COCCOLITHOPHORE BLOOM.....	42
PREFACE	42
INTRODUCTION	42
METHODS	43
RESULTS	48
DISCUSSION	58
IV. THE INFLUENCE OF PARTICLE CONCENTRATION AND BULK CHARACTERISTICS ON POLARIZED OCEAN LIDAR MEASUREMENTS	67
INTRODUCTION	67
METHODS	70
RESULTS	81
DISCUSSION	93
V. CONCLUSIONS AND FUTURE WORK.....	103
CONCLUSIONS	103
FUTURE DIRECTIONS	106
REFERENCES	109
VITA.....	124

LIST OF TABLES

Table	Page
1. Definitions, symbols, and units of notation used throughout the document.....	8
2. Lidar system parameters	14
3. Fitting statistics	23
4. Summary ANCOVA table comparing the relationship between a_{pg} and α between the Mid-Atlantic Bight and the Gulf of Maine.	33
5. Summary of bisquare robust regression model.....	57
6. Model parameterizations.....	81
7. Morphological and optical characteristics of particle suspensions used in light scattering experiment.....	82
8. Model sensitivity experiment results	91

LIST OF FIGURES

Figure	Page
1. Locations and instrument configurations for the Mid-Atlantic Bight and Gulf of Maine deployments	15
2. Lidar signal processing	20
3. Examples of lidar α compared with <i>in situ</i> IOP and AOP measurements.....	24
4. Relation between a_{pg} and α measured in the Mid-Atlantic Bight.....	25
5. Particulate backscattering ratio and the total linear depolarization ratio	25
6. Lidar power and α measured during a crossing of the Gulf of Maine.....	26
7. Lidar depolarization and backscattering ratio	27
8. Sections generated from glider measurements made during a 13-day crossing of the Gulf of Maine which overlapped the October 8, 2015 ferry crossing	28
9. Chlorophyll concentration versus b_{bp} from glider measurements.....	29
10. Comparison of α and chlorophyll measurements	30
11. a_{pg} versus α relationships observed for the Mid-Atlantic Bight and the Gulf of Maine	33
12. Map of the CoccoMix expedition and picture of the lidar installed at the bow of R/V <i>Endeavor</i>	45
13. Time series plot of surface IOP measurements.....	51
14. Time series plot of lidar and diffuse attenuation coefficients.....	53
15. Plots of α vs. $K_{d,s}$	54
16. Time series plot of b_b'/b_b (black) and δ (red).....	55
17. A three-dimensional plot of δ versus \mathcal{L}_b and b_b'/b_b	57
18. Plan view schematic showing the benchtop optical configuration for the depolarization measurement	74
19. Microscope images of particle suspensions used in light scattering experiment.....	83

Figure	Page
20. Histograms showing particle size distributions, expressed as equivalent spherical diameter (ESD), for each particle suspension.....	84
21. Laboratory depolarization experiment results	86
22. Bar graph showing estimates of $\mathbf{M}_{22}(\pi)$ in the near backwards direction	87
23. Plots showing results from the single-particle model sensitivity experiment.....	89
24. Plots showing results from the two-particle model sensitivity experiment	90
25. Plot of $\mathbf{M}'_{22}(\pi):\mathbf{M}^{\text{acid}}_{22}(\pi)$ versus $\phi':\phi_{\text{acid}}$ for non-zero values of ϕ_{acid} that resulted in a non-zero optimum value of ϕ'	92

CHAPTER I

INTRODUCTION

BACKGROUND

Light detection and ranging (lidar) is an active remote sensing technique used to determine the range to a reflective target. In its most basic form, a short (nanoseconds) pulse of light is emitted, and the intensity of light reflected back to the instrument is recorded as a function of time. The distance to the object is determined from the time-of-flight of the return pulse (using the speed of light in the medium of interest) and the intensity of the return pulse is used to determine the object's reflectivity. Though conceptually similar to active remote sensing technologies such as radio detection and ranging (radar), sound detection and ranging (sonar), and active microwave sensing, lidar fills several important gaps in our ability to sense the world around us by exploiting the unique properties of near-ultraviolet, visible, and near-infrared electromagnetic radiation (typically between 250-1064 nm wavelength). Ultraviolet, visible, and infrared light is efficiently scattered by micron-sized particles that are of interest to atmospheric and marine scientists, making lidar a useful technology for probing earth-system processes that are driven by particle dynamics (van de Hulst 1957). Furthermore, light in the visible portion of the spectrum is readily absorbed by molecules that participate in photochemistry, allowing us to use changes in intensity to determine the concentration of photochemically active materials (Kirk 1994). Light in this portion of the spectrum is also readily transmitted across the air-water interface, unlike sound waves that are strongly reflected and long-wave radiation (e.g. infrared, microwave, and radio waves) that is strongly absorbed by water. The pulsed laser sources used in lidar applications can be made to produce small-diameter (centimeter scale), highly collimated, coherent beams that permit three-

dimensional, high-spatial resolution reconstruction of distant objects. Combined, these capabilities have made lidar a highly desirable technology for solving problems that require ranging capabilities, particularly across air and water.

The lidar technique has matured rapidly since its development in the late 1960s, owing to advances in high-speed electronics, laser miniaturization technology, high-speed/high-capacity computers, and satellite-based global navigation systems (Kovalev and Eichinger 2004). The first commercially available lidar systems were developed for topographic mapping, and were so-called “discrete return” systems that provided only a single backscattered echo per pulse. These systems were useful for basic ranging applications where a single hard target was encountered by the beam, but were of little use for mapping scenes where multiple reflective targets (including continuous scattering media) were encountered by the beam. Later, multi-echo and photon-counting discrete return lidar systems were employed to discriminate non-topographic features such as buildings and vegetation canopy structure, and to permit bathymetric mapping applications where returns from the water surface and the sea-floor below are required to permit accurate mapping of water depth. Today, discrete return lidar systems play a role in a variety of industrial and environmental applications including forestry and vegetation monitoring (Coops et al. 2007), topographic and bathymetric mapping (Wang et al. 2015), archaeology (Chase et al. 2017), and three-dimensional structural surveying (Vu et al. 2004).

Dramatic advances in high-speed electronics and data storage capacity have enabled the development of full waveform lidar systems that record the backscattered laser energy as a continuous function of time. In addition to providing information on the range to hard targets, full waveform lidar can provide range resolved information on the distribution of material within a continuous scattering medium. The full waveform lidar measurement approach is centered around

retrieving profiles of two coefficients from profiles of attenuated backscatter, the volume scattering coefficient at 180° [$\beta(\pi)$] and the lidar extinction coefficient (α), that can be used to map the vertical distribution of materials within a scattering medium. This technique has been exploited with great success in the atmospheric sciences to solve sampling resolution problems associated with studying atmospheric processes that occupy a large range of spatial and temporal scales. Ground based lidar systems provide high temporal resolution measurements required to study the evolution of fast-acting atmospheric processes such as ice nucleation (Ansmann et al. 2005) and cloud phase transitions (Ansmann et al. 2009). Profiling lidar systems installed on aircraft can cover larger spatial scales to generate high resolution lidar “curtains” of backscatter and attenuation to examine the spatial structure of atmospheric particles. For example, airborne lidar systems have been used to measure the spatial structure and transport of Saharan dust (Esselborn et al. 2009), generate maps of planetary boundary layer height (Davis et al. 2000), and measure the vertical structure and microphysical properties of cloud and aerosol particles (Burton et al. 2013). At a global scale, the Cloud Aerosol Lidar with Orthogonal Polarization (CALIOP) instrument orbiting on the CALIPSO satellite has provided repeat global profiles of aerosol, cloud, dust concentrations as well as their microphysical properties, dramatically expanding our understanding of the role of atmospheric particles in global chemical cycles and Earth’s radiative budget.

In addition to providing information on the spatial distribution of scattering particles, polarization sensitive lidar can provide information on the bulk characteristics of distant particles. Many successful applications of polarization lidar have also come from the atmospheric lidar community, where profiles of linear depolarization (δ) have been used to measure the thermodynamic phase and orientation of cloud particles, (Noel and Sassen 2005; Hu 2007),

discriminate between aerosol types (Vaughan et al. 2009), and characterize the size distribution of cloud droplets (Roy et al. 1999). Early atmospheric polarization techniques relied on a unique scattering property of spherical particles, the absence of linear depolarization in the exact backscattering direction to separate scattering returns from morphologically (i.e. spherical or non-spherical) and functionally distinct particles (Sassen 2005). The concurrent development of multiple scattering lidar radiative transfer models provided a pathway for characterizing the influence of multiple scattering on δ , and for extracting information on particle size and concentration contained in the multiply-scattered component of the depolarization signal (Platt 1981; Hutt et al. 1994). Recent advancements in light scattering theory [e.g. T-matrix and discrete dipole approximation (DDA)] have expanded our ability to simulate the light scattering properties of morphologically complex particles, leading to the development of more advanced polarization lidar algorithms that can be used to distinguish between non-spherical particles of varying size, shape, and composition (Gordon and Du 2001; David et al. 2013; Mehri et al. 2018).

The substrates and energy sources that fuel ocean biogeochemistry exhibit strong spatial and temporal gradients that play an important role in structuring marine ecosystems. Historically, it has been challenging to resolve the distribution of marine ecosystems and the resources they depend on at relevant spatial and temporal scales, limiting our understanding of the ocean's role in the global climate system (Munk 2000). In the last four decades, satellite ocean color remote sensing technology (OCRS) has provided repeat global measurements of phytoplankton distributions across the ocean's surface, revolutionizing our ability to test hypotheses related to physical, chemical, and biological controls on ocean productivity and to model the ocean's role in Earth's climate (Jamet et al. 2019). However, ocean color techniques are limited in scope by their reliance on the sun as a passive radiation source. Ocean color measurements represent a daytime,

surface-weighted average over the ocean's top two optical depths (Gordon and McCluney 1975), missing deep phytoplankton populations and providing no information on their vertical structure. This “missing” vertical information introduces systematic error in primary production estimates, as the vertical distribution of biomass plays a key role in determining its exposure to factors controlling growth (e.g. light, nutrients, and temperature) and mortality (e.g. grazing pressure) (Behrenfeld 2010; Hill and Zimmerman 2010; Schulien et al. 2017).

Oceanographic lidar is the only currently available above-water remote sensing technology with the potential to fill the need for repeat, high spatial resolution measurements of the vertical distribution of upper ocean ecosystems. Capitalizing on the success of lidar in the atmospheric sciences and advances in full-waveform bathymetric lidar systems, Hoge et al. (1988) were the first to demonstrate the utility of lidar for measuring the vertical distribution of subsurface scattering layers using the NASA Airborne Oceanographic Lidar. In the time since this formative investigation, the capacity for oceanographic lidar to describe the distribution of marine particles in a quantitative manner has improved, owing to progress in modeling and interpretation of the lidar return signal (Gordon 1982; Churnside 2008; Churnside and Marchbanks 2015; Liu et al. 2019b) and development of hardware solutions to problems of signal inversion (Zhou et al. 2017; Hostetler et al. 2018). These advancements have facilitated high resolution measurements of phytoplankton biomass across the vertical and horizontal dimensions, providing insight into the influence of physical and biogeochemical processes on their distributions (Churnside et al. 2005; Churnside and Donaghay 2009; Churnside and Marchbanks 2015; Schulien et al. 2017; Moore et al. 2019). In certain cases, this capability can improve models of upper ocean primary production by permitting a more accurate representation of biomass distributions (Hill and Zimmerman 2010; Schulien et al. 2017). Oceanographic lidar has also been used to measure the distribution of upper

trophic level aquatic organisms (Churnside and Thorne 2005; Shaw et al. 2008; Churnside et al. 2011; Roddewig et al. 2017; Behrenfeld et al. 2019a). While these capabilities are in their early stages of development, they have major implications for our ability to explore interactions between “top-down” and “bottom-up” ecosystem processes, and to apply quantitative management practices to critical fisheries. Water penetrating lidar systems, which can simultaneously profile the atmosphere and ocean, offer a mechanism for characterizing the links between upper ocean ecosystem processes and atmospheric processes such as cloud and aerosol formation (Behrenfeld et al. 2019b). Furthermore, as demonstrated with CALIOP, spaceborne lidar can penetrate through optically thin clouds to improve our ability to characterize the distribution of high-latitude ocean ecosystems that are often obscured by cloud cover (Behrenfeld et al. 2017). If implemented at a global scale, spaceborne oceanographic lidar would thus close a major gap in our ability to characterize upper ocean processes important for predicting global climate dynamics.

Despite successful demonstrations of its utility for measuring the distribution of ocean ecosystems, several aspects of the lidar technique and its development have prevented its adoption by the ocean science community as a routine technology for characterizing marine ecosystems. Lidar signals exhibit complex dependencies on the optical properties of the water column as well as on geometric and electronic instrument characteristics that have made it difficult to develop robust quantitative techniques for relating lidar returns to the optical and biogeochemical properties of natural waters. To complicate the matter, very few lidar systems exist that were designed specifically for retrieving optical properties of the water column, and many of these are large, expensive airborne systems that are not widely available to the research community. Operational airborne systems such as the NASA AOL, the NASA High Spectral Resolution Lidar (HSRL) family of instruments, and the NOAA Fish Lidar are well positioned to provide wide scale

mapping of the vertical distribution of materials in the ocean as well as to demonstrate the technology for use in future satellite missions. However, validating airborne lidar measurements with traditional in-water optical and biogeochemical measurements is logistically challenging due to inherent differences in the spatial and temporal sampling scales of aircraft and seagoing research vessels and difficulties associated with coordinating research flights with in-water sampling programs. These challenges have prevented the generation of matchup datasets between lidar and in-water measurements that are sufficient for exploring the complexity of the lidar return signal and for developing and assessing new lidar techniques.

STUDY OBJECTIVES

In this dissertation, I address the problem of using oceanographic lidar as a routine technique for measuring the distribution and bulk characteristics of particles in the ocean by developing a shipboard lidar system that permits measurements of lidar attenuation (α) and linear depolarization (δ) at spatial scales identical to traditional in-water oceanographic measurements (refer to Table 1 below for a complete list of symbols and their definitions). In Chapter II, I focus on the development and characterization of such a lidar system in the context of several test deployments in the Mid-Atlantic Bight off the coast of Virginia and across the Gulf of Maine. Lidar profiles were validated against simultaneous measurements of *in situ* optical and biogeochemical properties and empirical relationships were established to retrieve biogeochemical properties related to the concentration and composition of materials in the upper water column. Chapter III explores the unique capabilities of shipboard lidar for measuring the distribution and characteristics of particles in the ocean and for characterizing the response of the lidar return to changes in particle concentration and composition. Specifically, the chapter focuses on the

potential to use polarized oceanographic lidar to identify a coccolithophore bloom based on the unique polarized light scattering properties of calcite and to map the distribution of fine-scale optical features at high spatial resolution. Chapter IV details a bio-optical modeling exercise used to quantify the sensitivity of δ to multiple scattering and changes in bulk particle characteristics. Lidar and *in situ* optical measurements from Chapter III were combined with laboratory measurements of δ for several compositionally and morphologically distinct marine particles to parameterize the model, revealing that the behavior of δ is not truly independent of particle concentration and that its behavior with respect to the intensive properties of marine particles is more complex than previously suggested. The success of this modeling study depended critically on the large number of matchups between lidar profiles of δ and *in situ* IOP measurements afforded by the shipboard lidar sampling scheme (> 1000 ; two orders of magnitude larger than any previous study), highlighting the important niche filled by compact shipboard lidar systems for the future development of the ocean lidar technique.

Table 1. Definitions, symbols, and units of notation used throughout the document

Definition	Symbol	Units
Inherent Optical Properties (IOPs)		
Absorption coefficient ($= a_{pg} + a_w$)	a	m^{-1}
Colored dissolved organic matter	a_g	m^{-1}
Particulate matter	a_p	m^{-1}
Particulate and colored dissolved organic matter	a_{pg}	m^{-1}
Pure water	a_w	m^{-1}
Scattering coefficient ($= b_p + b_{sw}$)	b	m^{-1}
Particulate matter	b_p	m^{-1}
Seawater	b_{sw}	m^{-1}
Backscattering coefficient	b_b	m^{-1}
Acid-labile particles	b_b'	m^{-1}
Particulate matter	b_{bp}	m^{-1}
Seawater	b_{bsw}	m^{-1}
Beam attenuation coefficient ($= a + b$)	c	m^{-1}
Particulate matter	c_p	m^{-1}

Table 1. *Continued*

Definition	Symbol	Units
Particulate and colored dissolved organic matter	c_{pg}	m^{-1}
Normalized scattering matrix element in row-x, column-y and at θ	$M_{xy}(\theta)$	dimensionless
$M_{22}(\pi)$ for acid-labile particles	$M'_{22}(\pi)$	dimensionless
$M_{22}(\pi)$ for acid-stable particles	$M_{22}^{acid}(\pi)$	dimensionless
$M_{22}(\pi)$ for all particles	$M_{22}^p(\pi)$	dimensionless
$M_{22}(\pi)$ for seawater	$M_{22}^{sw}(\pi)$	dimensionless
Volume scattering coefficient at θ	$\beta(\theta)$	$m^{-1} sr^{-1} \beta(\theta)$
Scattering phase function at θ	$\tilde{\beta}(\theta)$	sr^{-1}
Conversion factor between b_b and $\beta(\pi)$ [$b_b = 2\pi\chi(\pi)\beta(\pi)$]	$\chi(\pi)$	sr
acid-labile particulate matter	$\chi'(\pi)$	sr
acid-stable particulate matter	$\chi_{acid}(\pi)$	sr
particulate matter	$\chi_p(\pi)$	sr
Seawater	$\chi_{sw}(\pi)$	sr
Apparent optical properties (AOPs)		
Diffuse attenuation coefficient	K_d	m^{-1}
Diffuse attenuation coefficient estimated from surface IOPs	$K_{d,s}$	m^{-1}
Remote sensing reflectance	R_{rs}	sr^{-1}
Radiometric quantities		
Spectral downwelling planar irradiance	$E_d(\lambda)$	$W m^{-2} nm^{-1}$
Lidar parameters		
Degree of linear polarization	$DoLP$	dimensionless
Range along the lidar beam	R	m
Total photomultiplier voltage ($S = S_{ } + S_{\perp}$)	S	V
Co-polarized	$S_{ }$	V
Cross-polarized	S_{\perp}	V
Acid-labile particles	S'	V
Acid-stable particles	S_{acid}	V
Maximum value of S for each profile	S_{max}	V
Lidar attenuation coefficient	α	m^{-1}
Linear depolarization ratio ($= S_{\perp} / S_{ }$)	δ	dimensionless
Particulate linear depolarization ratio	δ_p	dimensionless
Decay of linear polarization with scattering optical depth as measured by lidar	ϕ	dimensionless
Acid-stable particle matter	ϕ_{acid}	dimensionless
Acid-labile particle matter	ϕ'	dimensionless
Particulate depolarization factor, dimensionless	ϕ_p	dimensionless
Depolarization factor for pure seawater, dimensionless	ϕ_{sw}	dimensionless
Total depolarization ratio ($= S_{\perp} / S$)	ρ	dimensionless
Biogeochemical properties		
Colored dissolved organic matter	CDOM	acronym
Chlorophyll a concentration	[Chl a]	$mg m^{-3}$
Shipboard fluorometer	[Chl a] _f	$mg m^{-3}$
Glider mounted fluorometer	[Chl a] _g	$mg m^{-3}$

Table 1. *Continued*

Definition	Symbol	Units
MODIS-aqua	$[\text{Chl } a]_{\text{MODIS}}$	mg m^{-3}
Ship-mounted radiometry	$[\text{Chl } a]_{\text{SAS}}$	mg m^{-3}
Particulate inorganic carbon	[PIC]	mg m^{-3}
Particulate organic carbon	[POC]	mg m^{-3}
Particle properties (Chapter IV)		
Surface area	A_s	μm^2
Average projected area	A_p	μm^2
Equivalent spherical diameter; diameter of a sphere with a projected area equivalent to A_p	ESD	μm
Fundamental properties		
Wavelength in a vacuum	λ	nm
Polar scattering angle	θ	rad
Depth	z	m

CHAPTER II

LIDAR CHARACTERIZATION IN THE MID-ATLANTIC BIGHT AND GULF OF MAINE

PREFACE

A modified version of this chapter was published by Elsevier in the journal *Remote Sensing of Environment* (<https://doi.org/10.1016/j.rse.2018.05.032>). The right to reproduce this article in theses or dissertations is retained by the author as per the Elsevier author rights agreement.

INTRODUCTION

Several demonstrations of the potential for oceanographic lidar to remotely map the vertical structure of the upper ocean and identify important features (sediment plumes, thin layers, fish aggregations, etc.) have been presented in the oceanographic literature. These studies have revealed the capability of oceanographic lidar to remotely map the vertical distribution of important features in the upper water column as a semi-quantitative product of lidar scattering and/or attenuation, but could not always relate lidar signals to *in situ* measurements of optical properties. The next important step in the development of this technology for oceanographic applications involves rigorously quantifying the vertical distribution of optical properties (a , c , K_d), and, by proxy, biogeochemical quantities (e.g., phytoplankton, suspended sediment, and detritus) from the lidar signals. The ability to measure profiles of lidar attenuation, backscatter, and depolarization contemporaneously with standard in-water optical and biogeochemical measurements is critical for characterizing the complex response of the lidar return to water column and instrument characteristics and for developing and assessing new lidar retrieval

algorithms. The purpose of this study was to (i) develop a portable ship-based lidar system, (ii) characterize its return signal, and (iii) explore its ability to remotely characterize the spatial structure of optical and biogeochemical properties of the water column from stationary platforms and moving vessels.

METHODS

Instrument Design

Our lidar system used a Litron Q-switch pulsed Nd:YAG laser (1064 nm), frequency doubled to 532 nm, emitting a 20 mJ pulse of linearly polarized light with a full angle beam divergence of < 2 mrad, and a full-width half-max (FWHM) pulse width of 4 ns. The emitted pulse was directed through a beam expander telescope and a pair of laser line mirrors (Thorlabs Model NB1-K13) that oriented the beam parallel to the viewing geometry. After exiting the beam steering assembly, the emitted pulse had a spot diameter of 1 cm, and a full angle divergence of < 0.5 mrad. The laser pulse exited through an acrylic window in the bottom of a watertight anodized aluminum housing, allowing the lidar to be deployed either below the water surface or above water from a floating or moving platform (Figure 1). The return pulse travelled through a 532 nm narrow-band interference filter positioned at the front-end of the collection optics assembly (Semrock LL01-532-12.5; 2.0 nm FWHM bandwidth; 12.5 mm diameter) to exclude background light. An anti-reflection coated polarizing beam splitter cube (CVI PBS-532-050; 1000:1 T_p/T_s extinction ratio; $T_p > 95\%$, $R_s > 99.9\%$) was used to separate the co-polarized and cross-polarized signals that were directed onto fast (< 1 ns pulse width, narrow spread in transit time) photomultiplier tubes (PMTs, Hamamatsu Model H10721-20). No additional collection optics (lenses or mirrors) were used in the system receiver. Stray capacitance in the detector signal circuitry broadened the apparent

instrument pulse width to 7 ns. For these deployments, the system field of view (FOV) was constrained by the acceptance angle of the interference filter to be 14° (full angle). The detector axis was oriented biaxial to the laser source with a 3.5 cm offset. According to this geometry, the range to complete overlap between the detector field of view and the laser source occurred at 29 cm when deployed above water, and 38 cm when deployed below the sea surface. This distance is sufficiently short that we opted to exclude data within this region from the analysis rather than to correct it for the overlap function given that the overlap function exhibits complex dependencies on a variety of instrument and water column properties.

The co-polarized and cross-polarized return signals were recorded digitally at a sampling rate of 1 GHz per channel with 8-bit resolution using a National Instruments (NI) PXI-5154 digitizer in conjunction with an NI data acquisition module (PXI-5154) and chassis (PXI-1042) operating under Microsoft Windows. Aspects of the lasing system (laser power and repetition rate) were controlled using Litron's proprietary laser control system (Litron Laser Control Client). The detector and data acquisition systems were controlled using custom software written in LabView® that allowed for adjustment of sample frequency and PMT gain via a graphical user interface. For a detailed list of lidar instrument parameters, refer to Table 2.

Table 2. Lidar system parameters

Parameter	Value
Transmitter	
Laser	Frequency doubled Nd-YAG
Pulse rate	10 Hz
Wavelength	532 nm
Pulse energy	20 mJ
Pulse width	4 ns FWHM
Beam diameter	1 cm
Beam divergence	< 2 mrad
Polarization	Vertical linear polarization
Receiver Optics	
Interference Filter	
Diameter	12.5 mm
Filter bandwidth	2 nm FWHM
Polarizing beamsplitter	
Extinction ratio ($T_p:T_s$)	> 1000:1
Transmission P-Polarization (T_p)	> 95%
Reflectance S-Polarization (R_s)	> 99.9%
Detector	
Type	Photomultiplier tube
Collection mode	Current
Rise time	0.57 ns
System geometry	Biaxial
Field of view (full angle)	14° in-water 10° in-water
Detector configuration	29 cm (above-water)
Optical axis offset	38 cm (in-water)
Data acquisition	
Sampling rate	1 GSamples s ⁻¹ channel ⁻¹
Resolution	8 bit
Channels	2

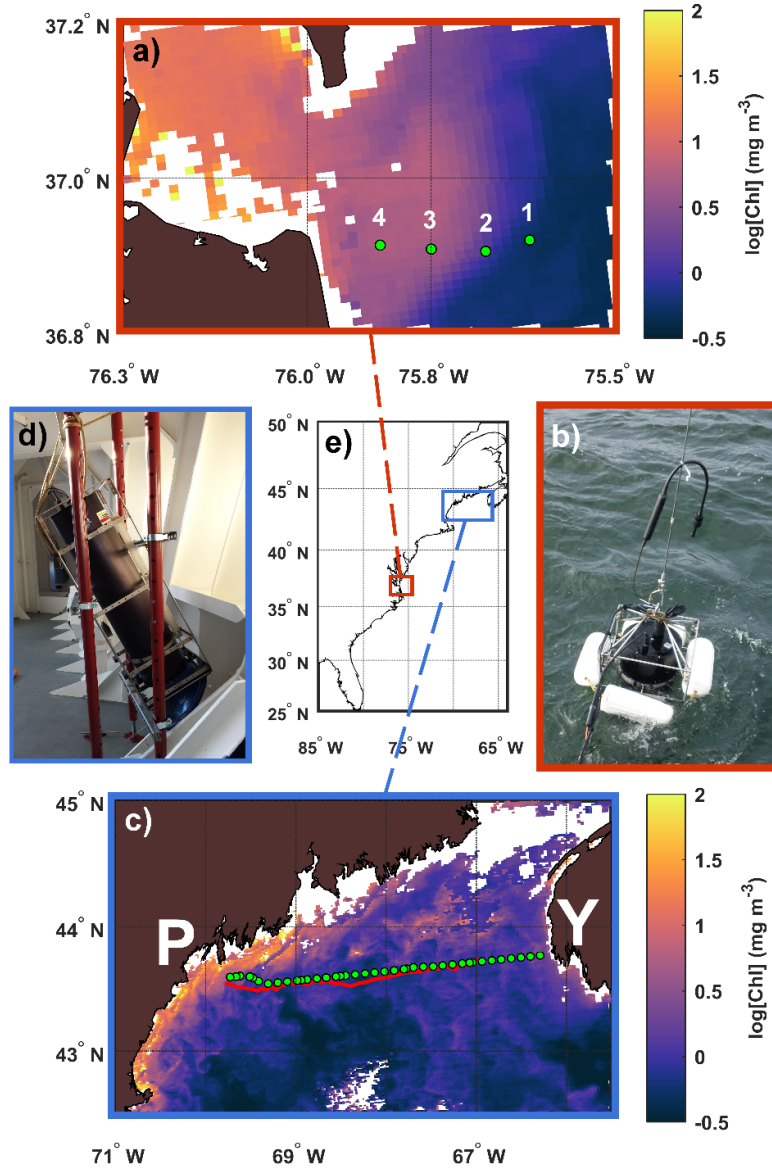


Figure 1. Locations and instrument configurations for the Mid-Atlantic Bight and Gulf of Maine deployments. a) The lidar was deployed at four stations (green dots) off the Virginia coast during two day-cruises in 2015. Stations are plotted over the June 30, 2015 MODIS chlorophyll product. b) Photograph showing *in situ* deployment scheme used for the coastal Virginia deployment. c) Lidar cruise track (green dots) across the Gulf of Maine from Portland, ME (P) to Yarmouth, NS (Y). The red line indicates the track of the Slocum glider. Tracks are plotted over the October 8, 2015 MODIS chlorophyll product. d) Photograph showing lidar mounted to ferry point through a fairlead near the bow. e) Map of the US/Canada eastern seaboard for orientation.

Mid-Atlantic In-Water Deployments

The lidar was initially field tested during two day-cruises (May 4, 2015 and June 30, 2015) into the Mid-Atlantic Bight aboard the R/V *Fay Slover*. These cruises were characterized by strong horizontal gradients in optical properties ranging from clear oceanic water at the offshore region to highly turbid estuarine water close to the mouth of the Chesapeake Bay (Figure 1a). The water column in this region can exhibit complex stratification patterns resulting from salinity fronts associated with the estuarine outflow from the Chesapeake Bay as well as heat-related stratification in summer (Johnson et al. 2001). These conditions resulted in vertical gradients in water column optical properties as well, providing a challenging environment in which to test the capability of the lidar to resolve these vertical features. Four stations were occupied along a 30 km transect running from Cape Henry, Virginia, USA, eastward into the Mid-Atlantic Bight (Figure 1a). The instrument was deployed at the sea surface using the ship's A-frame, such that the acrylic window was 1 m beneath the water (Figure 1b).

Inherent optical properties (IOPs) were measured directly at each station using a profiling package consisting of two *ac-9* (WET Labs) *in situ* spectrophotometers (one filtered for 0.2 μm ; one unfiltered), a Hydroscat-6 (HOBI Labs) backscatter meter, and an SBE 37-SI CTD (Seabird). The pair of *ac-9* spectrometers were used to measure profiles of the absorption coefficient due to dissolved material (a_g = CDOM only; filtered *ac-9*), the total non-water absorption coefficient (a_g = particles + CDOM; unfiltered *ac-9*), and the total non-water attenuation coefficient (c_{pg} = particles + CDOM; unfiltered *ac-9*) at 9 wavelengths (412, 440, 488, 510, 532, 555, 650, 676 and 715 nm). The total particulate scattering coefficient (b_p) and single scattering albedo (ω_o) were calculated as $b_p = c_{pg} - a_{pg}$ and b_p/c_{pg} , respectively for each wavelength measured by the unfiltered *ac-9*. Profiles of the particulate backscattering coefficient (b_{bp}) were measured using the

Hydroscat-6 (HOBI Labs) at wavelengths of 420, 442, 470, 510, 590, and 700 nm and interpolated using a cubic spline to produce estimates of the particulate backscattering ratio (b_{bp}/b_p) at 532 nm. All *in situ* vertical profiles were then interpolated to a regular depth interval of 0.5 m using a cubic spline. Unless otherwise specified, all optical properties presented below refer to measurements at 532 nm.

A Hyperpro (Satlantic) profiling radiometer was deployed at each station to measure vertical profiles of downwelling irradiance (E_d). The diffuse vertical attenuation coefficient at 532 nm (K_d), an apparent optical property (AOP), was then calculated by a linear regression of the natural log-transformed profile of E_d against depth. Calculations of K_d were performed for separate vertical layers when *ac*-9 or CTD profiles showed evidence of vertical stratification in optical and/or physical properties.

Gulf of Maine Above-Water Deployments

The lidar system was deployed aboard the M/V *Nova Star* ferry in an above-water configuration, allowing continuous sampling during a crossing of the Gulf of Maine (GoM) from Yarmouth, NS to Portland, ME on October 8, 2015 (Figure 1c). The lidar was mounted on the vehicle deck approximately 10 m above the sea surface at an angle of 26° from nadir, pointed through a fairlead near the bow (Figure 1d) that provided a view of the ocean surface undisturbed by the ship's wake. Lidar measurements were taken at 15-minute intervals, and in conjunction with 9 expendable bathythermograph (XBT) deployments that measured vertical temperature profiles across the 316 km cruise track, as the ship steamed continuously, resulting in 39 lidar observations separated by 7 to 9 km each. Each observation was completed within a horizontal

distance of approximately 0.6 km assuming a 1-minute sampling period and average ship speed of 20 knots.

A variety of discrete and continuous measurements were made coincident with lidar measurements. Surface water IOPs were measured using a flow-through system installed on the M/V *Nova Star*. A pair of *ac-9* (WET Labs) spectrophotometers (one filtered $<0.2 \mu\text{m}$; one unfiltered) were plumbed into the flow-through system to measure a_g , a_{pg} , and c_{pg} ; and calculate b_p as described above. Chlorophyll *a* (Chl *a*) fluorescence was measured continuously using a WET Labs flow-through fluorometer ($[\text{Chl } a]_f$), and the data were post-calibrated to extracted Chl *a* concentrations by acetone extraction of samples taken at discrete hourly intervals (Knap et al. 1996) using $0.45 \mu\text{m}$ pore size HA nitrocellulose filters to sample the picoplankton efficiently (Phinney and Yentsch 1985). All flow-through data were corrected for a 6-minute lag induced by the sample volume transit time through the flow-through system. Normalized water-leaving radiance was measured using a SAS Above Water Radiometer (Satlantic) mounted at the bow of the ship, and the NASA OC-4 algorithm was applied to derive remote sensing Chl *a* concentrations ($[\text{Chl } a]_{\text{SAS}}$) (O'Reilly et al. 1998).

A Teledyne Slocum electric glider (model G2) operated by the Bigelow Laboratory for Ocean Science, was deployed to sample along the transect, making a 13 day (October 7, 2015 – October 19, 2015) eastbound crossing from $\sim 40 \text{ km}$ east of Portland, ME ($43.550^\circ\text{N } 69.783^\circ\text{W}$) to $\sim 65 \text{ km}$ west of Yarmouth, NS ($43.742^\circ\text{N } 66.964^\circ\text{W}$). Water column density was calculated from measured profiles of temperature and salinity. Chl *a* fluorescence measurements were made using an on-board fluorometer, and measurements of b_{bp} were made using a WET Labs ECO-triplet optical sensor. Chlorophyll *a* fluorescence was converted to glider estimates of extracted Chl *a* concentration ($[\text{Chl } a]_g$) based on a comparison of parallel glider and discrete measurements

(with extractions) made upon glider deployment and retrieval. Measurements of b_{bp} were determined from factory calibrations of the ECO-triplet.

Lidar Signal Processing

At each station, 100 lidar profiles were collected at each of five PMT gain settings (500 total profiles per station), requiring approximately 1 min to cycle through the gain settings. Data logging was triggered by the laser Q-switch, however the time between the Q-switch trigger and the generation of the laser pulse fluctuated in time making it an unreliable determinant of time-zero. Consequently, time-zero of the lidar pulse was defined by strong backscattering off the acrylic window at the face of the lidar housing. The 100 shots taken at each gain setting were averaged and the averages stitched together in vertical segments where the signal was neither saturated nor suboptimal with respect to signal-to-noise, increasing the effective dynamic range of the instrument (Figure 2a). Stitching was performed by re-scaling each waveform to the profile measured using the highest gain setting such that coincident regions of unsaturated signal decay overlap (Figure 2b) and merging the portions of each signal that were > 0 but not saturated (Figure 2c). The non-saturated signal measured with the highest signal-to-noise was used when multiple overlapping signals were all below saturation (Figure 2c). The vertical geometry of the in-water deployments allowed the depth range to be calculated as half the return time multiplied by the speed of light in seawater (0.225 m ns^{-1}) to account for the round trip of each photon. A vertical offset of 1 m was added to the corresponding geometric depth to account for the position of the optical window beneath the sea surface.

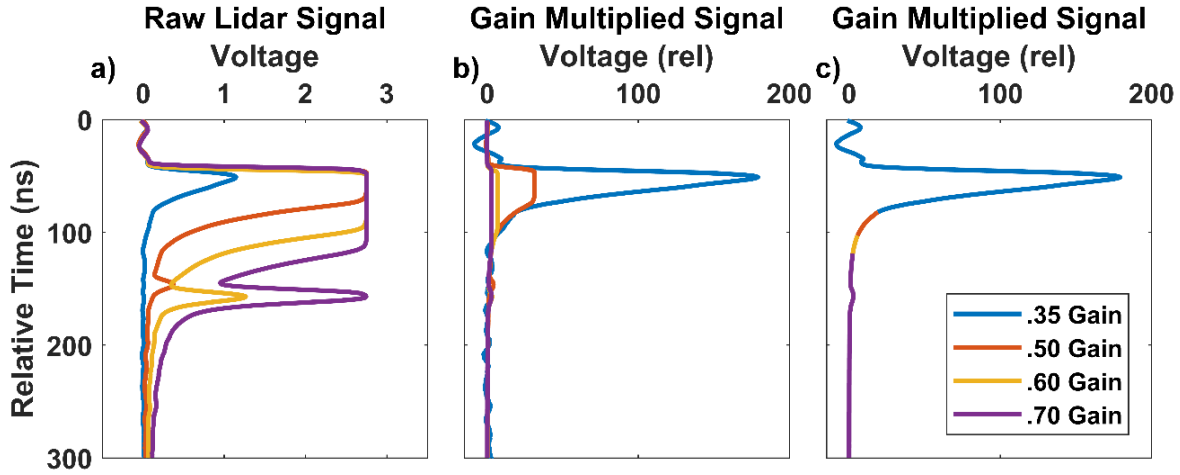


Figure 2. Lidar signal processing. a) Raw lidar signals from a single station, collected at multiple PMT gain settings indicated by the colored lines. b) Lidar signals re-scaled to a single PMT gain setting, showing signal quality and saturation of the digitizer at 2.75 V. c) Lidar signal at a single station created by eliminating the saturated portions and merging the signals measured at each gain setting.

For above-water deployment aboard the *M/V Nova Star*, the signal was further separated into in-air and in-water segments by the strong backscatter return from the surface of the water. The range to the water's surface R_{air} was calculated as half the time between the window backscattering peak, and the water's surface peak, and multiplied by the speed of light in air (0.300 m ns^{-1}). The in-water beam angle was calculated to be 19° from nadir using Snell's Law assuming the beam struck the water at an incident angle of 26° (in air), a flat sea surface, and a seawater refractive index of 1.33. The in-water range (as calculated above for the in-water deployment) was corrected to vertical depth as the cosine of the resulting 19° angle of beam propagation in water.

After merging the 500 shots from each station into a single profile of return power for the co-polarized signal (S_{\parallel}), and the cross-polarized signal (S_{\perp}), the co-polarized and cross-polarized

signals were summed to obtain a total signal (S), and the total depolarization ratio (ρ) was calculated as:

$$\rho = \frac{S_{\perp}}{S_{\parallel} + S_{\perp}} = \frac{S_{\perp}}{S} \quad \text{Eq. 1}$$

For the MAB deployments, vertical profiles of ρ were interpolated to 0.5 m intervals to allow for comparison with vertical profiles of optical properties made *in situ*. The depolarization ratios presented here are uncorrected for instrumentation effects on the detection of the return signal polarization state (e.g. beam splitter efficiency, polarization effects at the acrylic window, and detector efficiency) and thus are specific to this instrument. However, our laboratory measurements of the return from a totally depolarizing target (Spectralon Model SRT-99-100, (Sanz et al. 2013) suggest that these instrument effects amount to <10% error in the magnitude of ρ . The system attenuation coefficient (α) was calculated using the slope method (Kovalev and Eichinger 2004) for regions of constant decay as:

$$\alpha = -\frac{1}{2} \frac{d}{dR} \ln [P_r(R) * R^2] \quad \text{Eq. 2}$$

where R was the range or distance along the beam, and the multiplication of the return signal by R^2 corrects for the decrease in solid angle subtended by the detector with range. In the case of the above water measurements, R_{air} is added to each range bin prior to range correction in order to account for the position of the lidar above the water's surface. Regions of the signal that were contaminated by detector saturation or by the bright specular reflection off of the acrylic window or sea surface were excluded from the analysis, setting the upper range from which α was calculated. The range was then converted to depth according to the view angles (0° for in-water deployments, 26° in-air, 19° in-water for above-water deployments) described above.

RESULTS

Mid-Atlantic Deployments (In-Water Measurements)

In general, α measured in the clear offshore water of the Mid-Atlantic Bight (Stations 1 & 2) was lower than at the more turbid stations (Stations 3 & 4) close to shore (Figure 3). Vertical differences in α at Stations 3 & 4 were spatially consistent with the vertical structure in optical properties measured using the *in situ* instrumentation (Figure 3 c,d). The magnitude of α was most consistent with measurements of a_{pg} (Figure 3), and lower than a ($= a_{pg} + a_{water}$), K_d , or c . α was linearly related to a_{pg} measured during the transects into the Mid-Atlantic Bight [see Table 3. for all regression statistics] (Figure 4).

The linear depolarization ratio (ρ) was related non-linearly to b_{bp}/b_p measured *in situ* (Figure 5) that could be approximated empirically by a second-order exponential function (Figure 5, Table 3). The data gap for $\rho = 0.26$ to 0.34 resulted from the transect crossing a discrete front between Stations 2 & 3 that separated the Chesapeake Bay outflow plume from the oceanic water of the Mid-Atlantic Bight.

Gulf of Maine Deployment (Above-Water Measurements)

When deployed above-water on the Gulf of Maine ferry, the lidar signal peaked at ~ 2 m depth due to the Gaussian shape of the specular return from the sea surface, after which it decayed exponentially to a detection limit at about 20 m (Figure 6a). The peak P_r signal was highest in the coastal waters of the western GoM near Portland (68.58°W to 70°W), decreased eastward into the central GoM, and rose again as the track approached the eastern shore near Yarmouth (66°W to 66.7°W , Figure 6a). The lidar signal showed no vertical structure in the upper 20 m, as was evident from the linear decrease of the natural log corrected signal with depth across the transect (Figure

6a). This observation suggests that the upper water column was vertically homogenous with respect to optically active components during the October 2015 deployment, at least within the detection limits of the lidar system. As with the peak value of S (S_{\max}), α decreased eastward across the Gulf of Maine to a minimum of 0.075 m^{-1} at 66.83°W , then increased dramatically in the waters near Yarmouth, NS (Figure 6b). Measurements of α were positively related to S_{\max} along the transect (Figure 6c, Table 3).

Table 3. Fitting statistics

Regression Model: $f(x,y) = jx + k$						
Figure	j (\pm 95% CI)	k (\pm 95% CI)	r^2	df	p	
Figure 4	0.77 (\pm 0.27)	0.011 (\pm 0.020)	0.81	10	< 0.001	
Figure 6c	0.038 (\pm 6.96 x 10 ⁻³)	-0.20 (\pm 0.054)	0.77	37	< 0.001	
Figure 10b	47.8 (\pm 14.4)	-2.90 (\pm 1.25)	0.61	30	< 0.001	
Figure 11 (red)	1.69 (\pm 0.49)	-0.094 (\pm 0.045)	0.55	35	< 0.001	
Figure 11 (black)	0.77 (\pm 0.27)	0.011 (\pm 0.020)	0.81	10	< 0.001	
Regression Model: $f(x,y) = je^{kx} + le^{mx}$						
Figure	j (\pm 95% CI)	k (\pm 95% CI)	l (\pm 95% CI)	m (\pm 95% CI)	r^2	df
Figure 5	0.0044 (\pm 2.57 x 10 ⁻³)	1.47 (\pm 7.63)	1.011 x 10 ⁻⁴ (\pm 5.31 x 10 ⁻⁴)	15.2 (\pm 12.7)	0.98	69

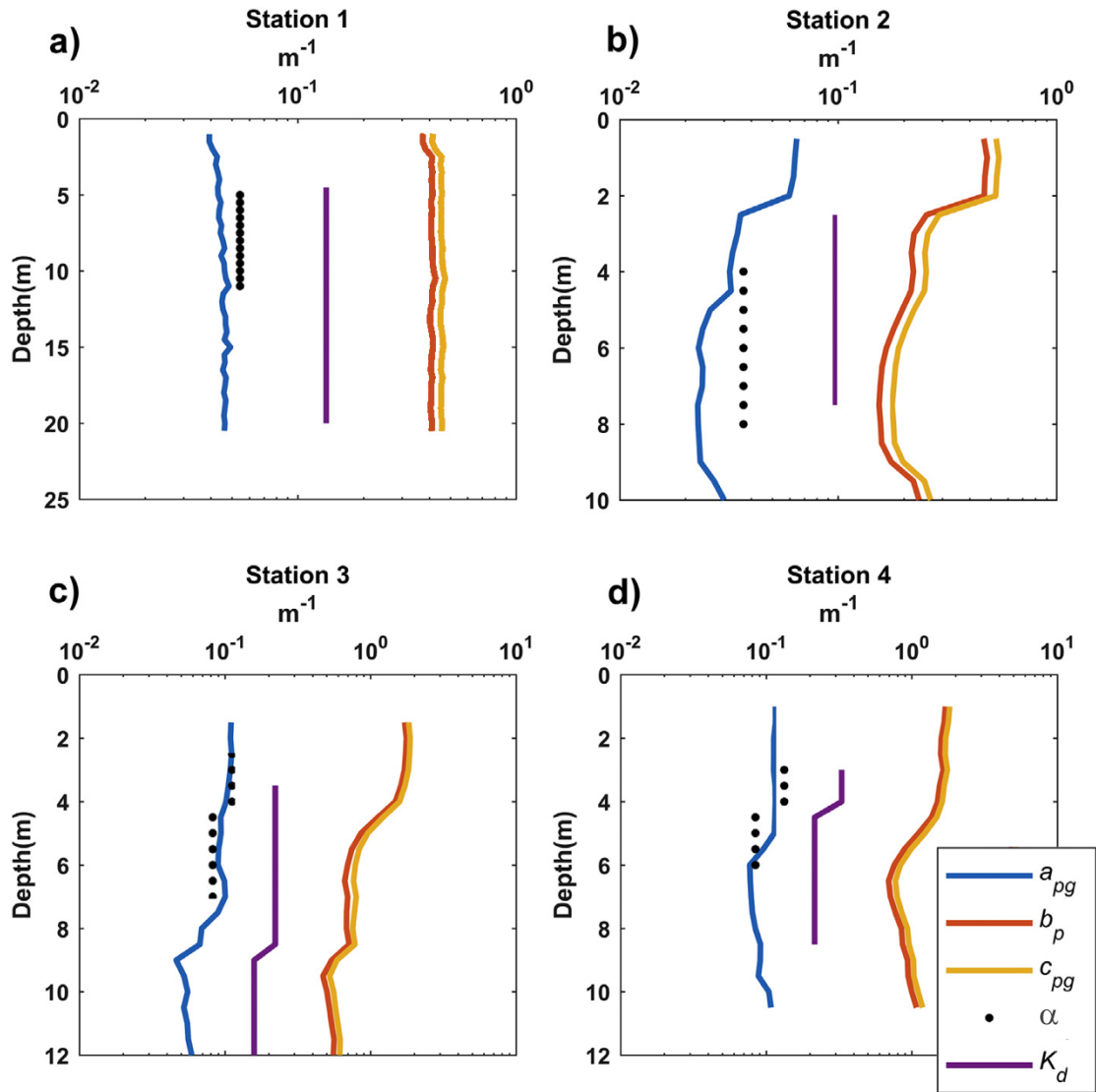


Figure 3. Examples of lidar α compared with *in situ* IOP and AOP measurements. Plots showing depth profiles of IOPs and AOPs measured simultaneously with lidar profiles in the Mid-Atlantic Bight. Stations ranged from clear, oceanic waters at the furthest station offshore (a) to highly turbid coastal waters at station 4 (d). Variations in a with depth can be seen at stations 3 and 4 (c, d). Refer to Figure 1a for station locations.

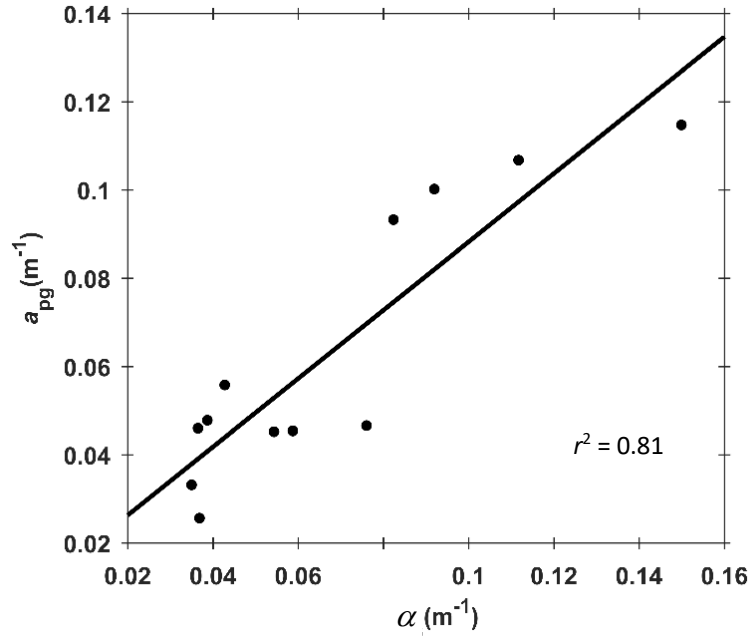


Figure 4. Relation between a_{pg} and α measured in the Mid-Atlantic Bight.

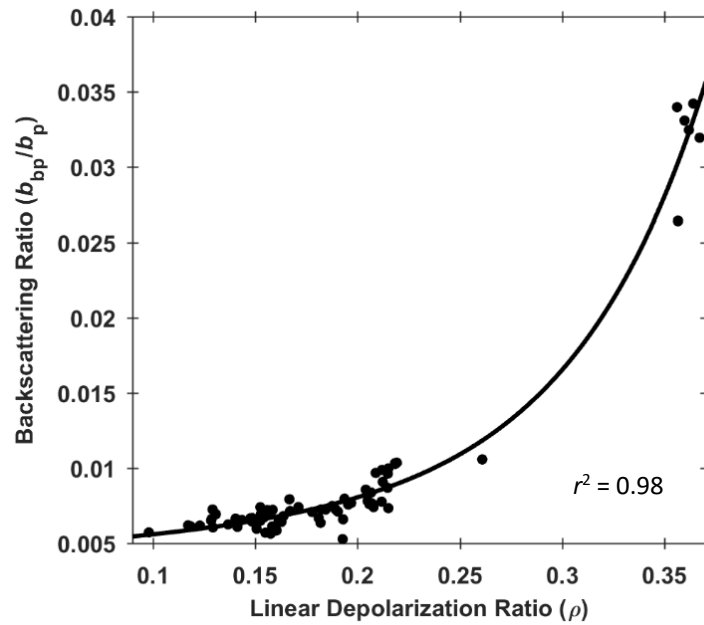


Figure 5. Particulate backscattering ratio and the total linear depolarization ratio. The linear depolarization ratio (ρ) of the lidar signal was fitted to coincident *in situ* measurements of b_{bp}/b_p using a least squares exponential regression (black line).

Linear depolarization ratios from depths shallower than 1.5 m were excluded from the analysis due to signal artifacts caused by the strong surface reflection. Similarly, values of ρ retrieved below 7.5 m were excluded from the analysis due to a low signal in the cross-polarized channel. Values of ρ ranged from 0.05 to 0.14 along the transect (Figure 7). Using the relationship developed between ρ and b_{bp}/b_p from the Mid-Atlantic deployments (Figure 5), these depolarization ratios produced estimates of b_{bp}/b_p from 0.0048 to 0.0063 across the GoM transect.

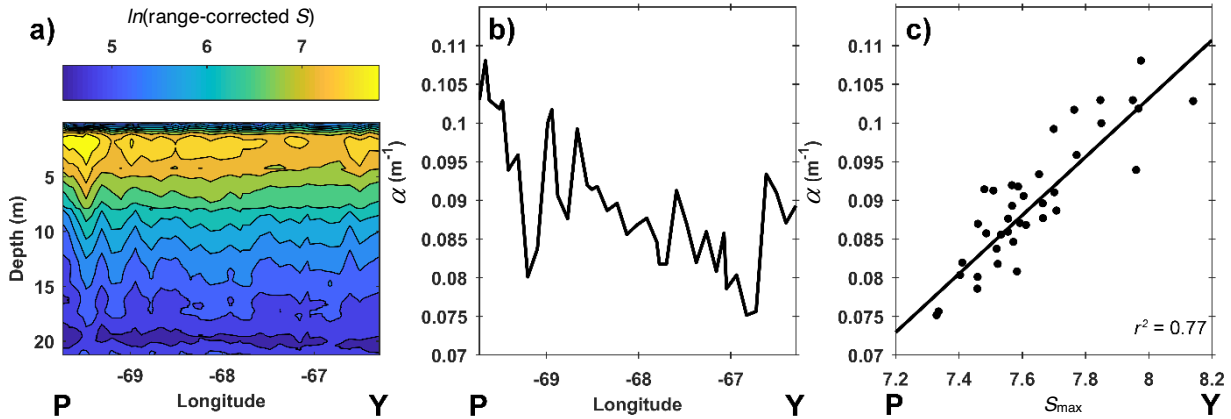


Figure 6. Lidar power and α measured during a crossing of the Gulf of Maine. a) Vertical section across the GoM illustrating the range corrected lidar return power along the transect, with a maximum peak value near Portland, ME and Yarmouth, NS. b) α resulting from the lidar profiles plotted as a function of position along the transect. c) Relationship between S_{\max} and α for the GoM transect.

Spatial patterns of water column properties measured from the Slocum Glider were consistent with those derived from lidar measurements. Water column density measured along the

eastbound glider track showed a pycnocline located at approximately 80 m depth on the western portion of the Gulf, which shoaled eastward to a depth of approximately 50 m just west of Yarmouth, NS (Figure 8a). This suggests that the upper water column was well-mixed within the 20 m depth of the lidar retrieval and is consistent with the lack of vertical structure in the measurements of α (compare Figure 8a with Figure 6a).

Chlorophyll *a* concentrations were patchy on the westernmost portion of the track (69.8°W to 69°W), became more uniform eastward toward the center of the crossing (69°W to 67.5°W), and rose sharply on the east end of the section (67.5°W to 67°W) (Figure 8b). Although the section map suggests some vertical structure in Chl *a* across the GoM, the oscillation likely resulted from fluorescence quenching, as the low concentrations occurred around noon each day (Figure 8b).

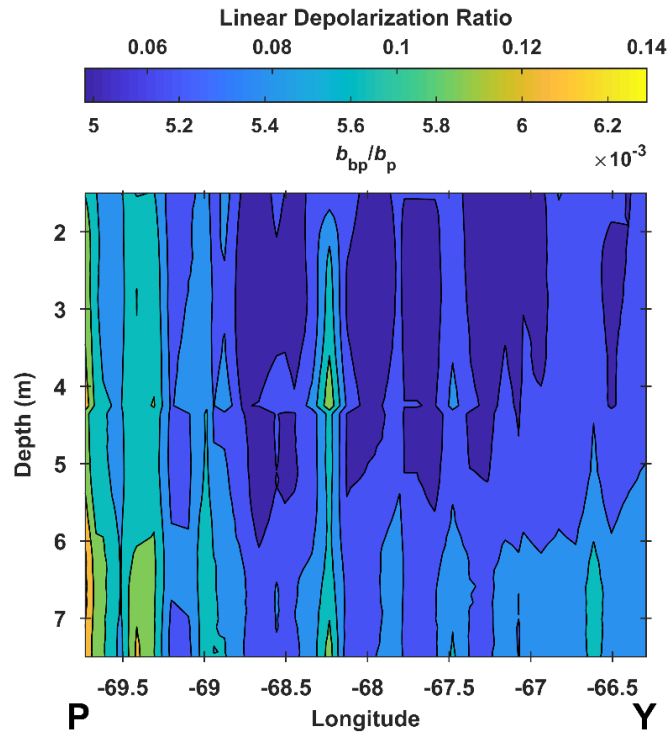


Figure 7. Lidar depolarization and backscattering ratio (from the relationship described in Figure 5) sections across the GoM transect.

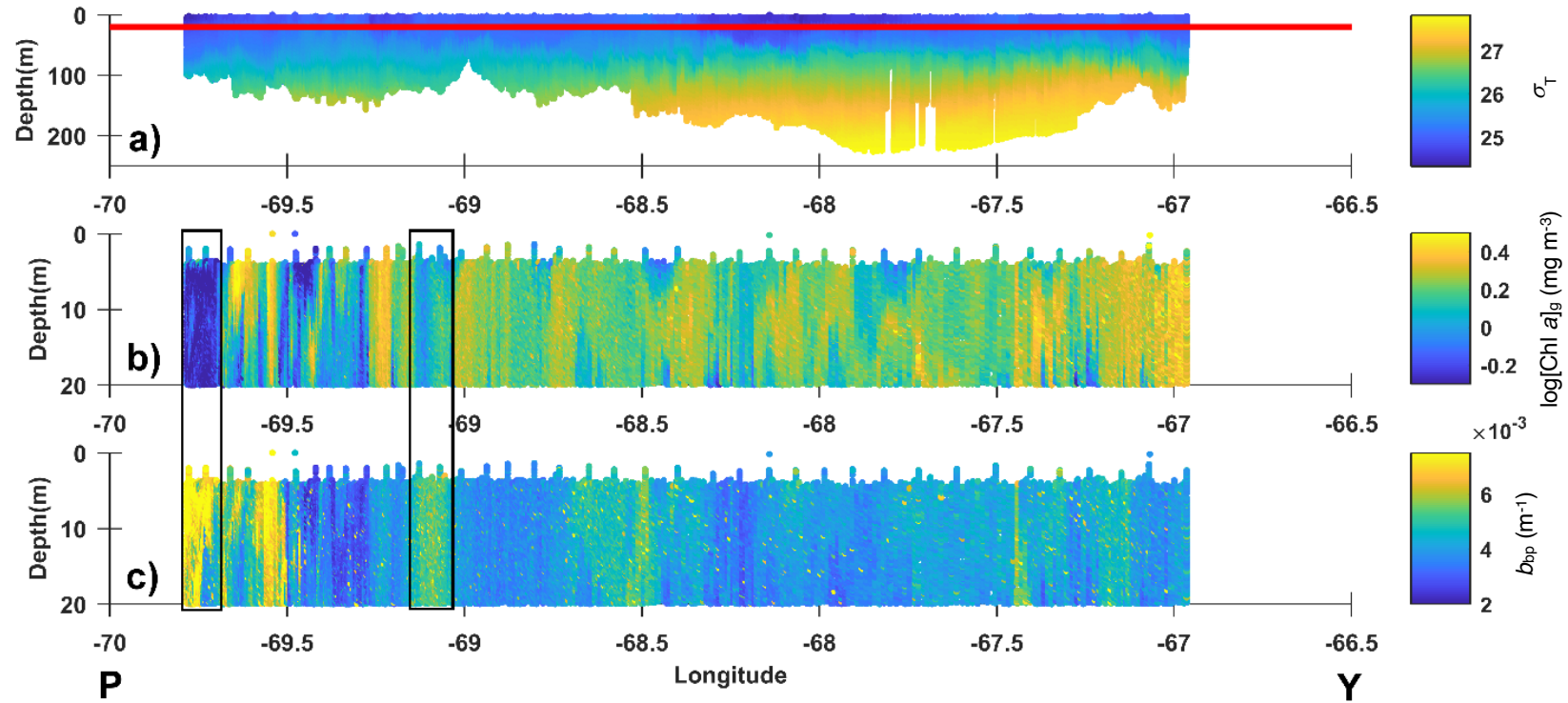


Figure 8. Sections generated from glider measurements made during a 13-day crossing of the Gulf of Maine which overlapped the October 8, 2015 ferry crossing. a) Measurements of density (as σ_T) calculated from glider measurements of temperature and salinity. Maximum depth of lidar signal included in analysis indicated by red line. b) Glider section showing measurements of fluorescence derived $[\text{Chl } a]_g$. c) Glider section showing measurements of b_{bp} . Regions corresponding to measurements of increased b_{bp} and decreased $[\text{Chl } a]_g$ are highlighted by black boxes

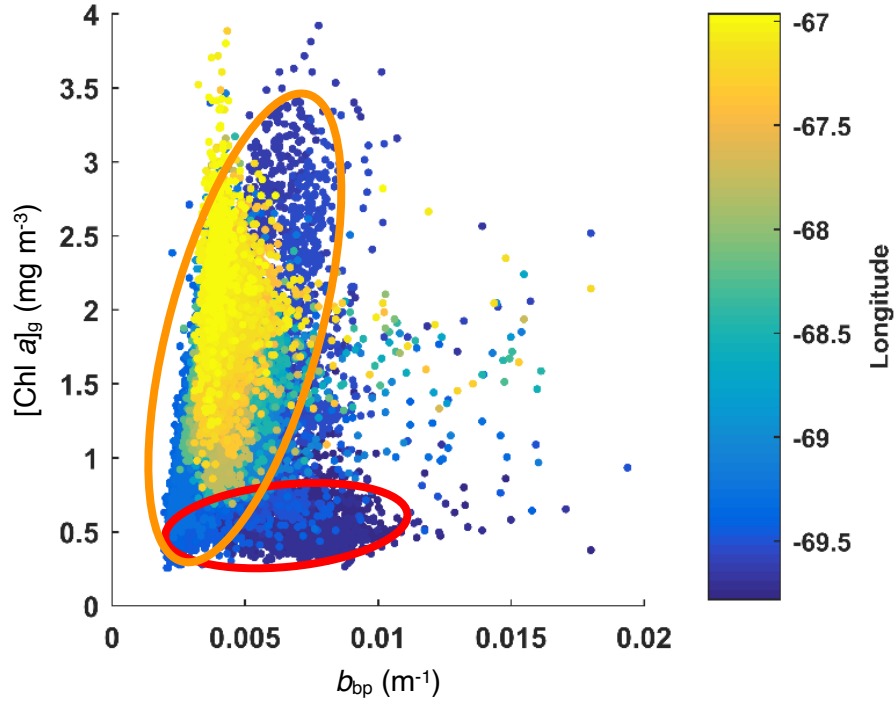


Figure 9. Chlorophyll concentration versus b_{bp} from glider measurements. $[\text{Chl } a]_g$ and b_{bp} measurements made at depths relevant to the lidar depolarization ratio depth range (1.5 - 7.5 m). On the eastern portion of the crossing (highlighted by orange ellipse), $[\text{Chl } a]_g$ measurements were distributed over a relatively small range of b_{bp} . On the western portion of the transect, the range of both b_{bp} and $[\text{Chl } a]_g$ increases. On the western margin of the transect, a shift in the backscattering material can be seen as a decrease in the range of $[\text{Chl } a]_g$, and an increase in the range of b_{bp} (red ellipse).

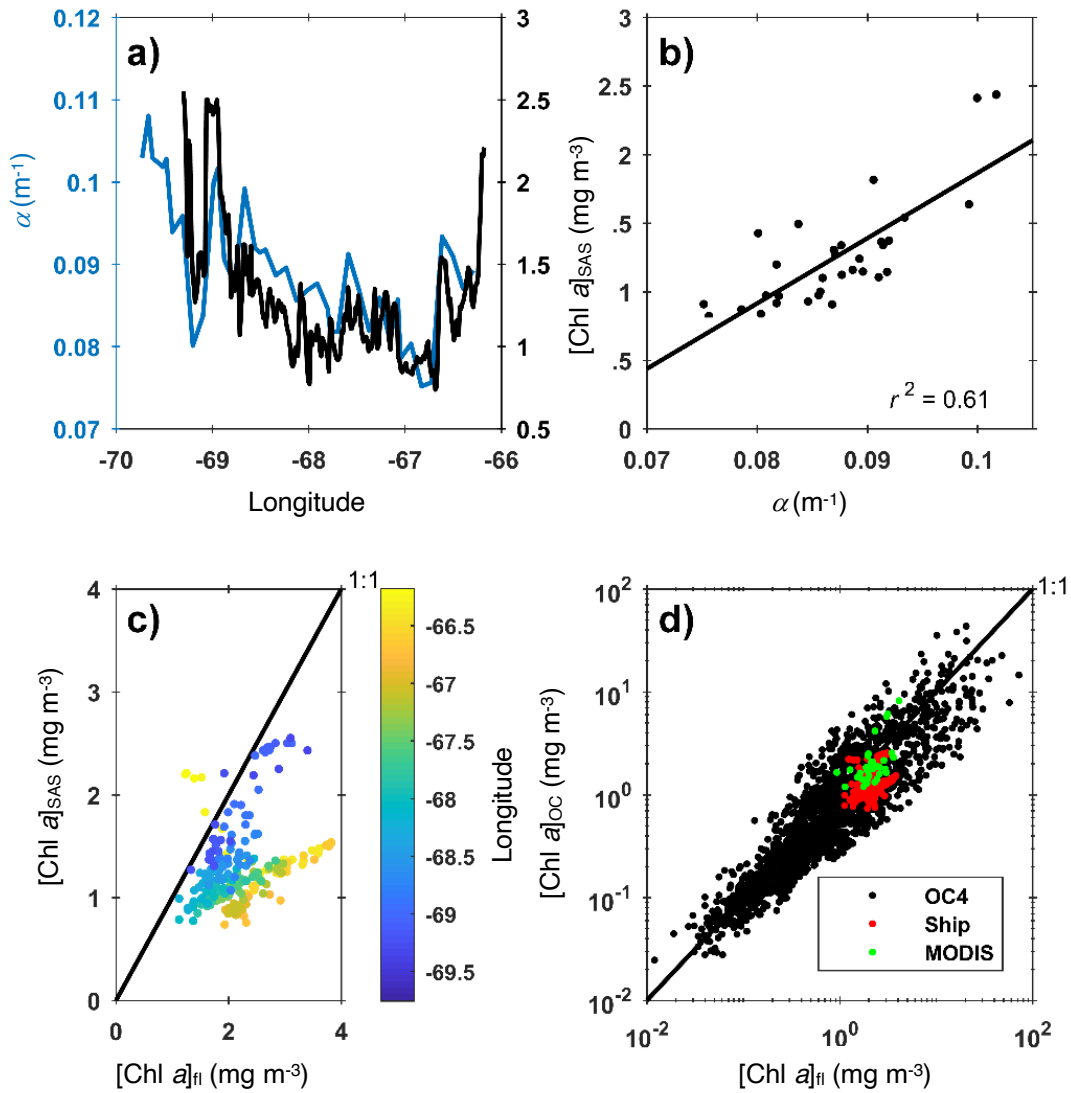


Figure 10. Comparison of α and chlorophyll measurements. a) Plot of α (blue) and $[\text{Chl } a]_{\text{SAS}}$ (black) versus longitude along the GoM ship track. b) Coincident measurements of α and $[\text{Chl } a]_{\text{SAS}}$ were linearly related. c) Plot of $[\text{Chl } a]_{\text{SAS}}$ vs. $[\text{Chl } a]_{\text{fl}}$ overlaid on a 1:1 line (black). Plotted symbols were color-coded based on longitude along the transect. d) Plot of both $[\text{Chl } a]_{\text{MODIS}}$ (green) and $[\text{Chl } a]_{\text{SAS}}$ (red) vs. $[\text{Chl } a]_{\text{fl}}$ overlaid on a plot of the NOMAD ocean color validation dataset places our measurements into the context of the typical error of remote sensing algorithms.

Values of b_{bp} along the upper 20 m of the glider section ranged from 0.002 to 0.011 m⁻¹, and were highest near the surface on the easternmost portion of the section, with patches of increased b_{bp} eastward from -68.7° to -67° (Figure 8c). Along the eastern portion of the section, patches of high b_{bp} were spatially consistent with patches of high chlorophyll, suggesting that variability in backscatter was driven by changes in phytoplankton biomass (cf. Figure 8b, c). West of -69°, patches of increased b_{bp} were spatially inconsistent with patches of increased $[Chl\ a]_g$, suggesting a shift in the nature of the backscattering source material from phytoplankton to minerogenic sediment on the western margin of the GoM (cf. Figure 8b, c). The portion of the glider section where this shift occurred (-69.5° to -69.8°) coincided with the region of increased lidar depolarization (cf. Figure 7, Figure 8b, c). The shift in the nature of the scattering particles contributing to the lidar signal became further evident by plotting glider measurements of $[Chl\ a]_g$ vs. b_{bp} for the range of depths where the lidar depolarization ratio was obtained (3 m to 15 m) (Figure 9). The eastern portion (Figure 9, yellow symbols) of the glider section (longitude -67° to -68°) was characterized by a narrow range of b_{bp} values that were distributed across a wide range of $[Chl\ a]_g$, while the westernmost portion (Figure 9, dark blue symbols) of the glider section (longitude -69° to -70°) was characterized by a wider range of b_{bp} values distributed over a wider range of $[Chl\ a]_g$ values.

The spatial patterns of α and $[Chl\ a]_{SAS}$ were similar across the GoM transect, with high values near the coastal waters of Maine and Nova Scotia that decreased toward the center of the GoM (Figure 10a). There was a positive linear relationship between α and $[Chl\ a]_{SAS}$ across the entire transect (Figure 10b; Table 3). Although the MODIS chlorophyll product ($[Chl\ a]_{MODIS}$) also revealed high values near the coasts of Maine and Nova Scotia (Figure 1c), $[Chl\ a]_{MODIS}$ failed to capture much of the fine-scale variability in $Chl\ a$ across the transect and showed no correlation

with either α or $[\text{Chl } a]_{\text{SAS}}$ (not shown). Although there was a strong relationship between $[\text{Chl } a]_{\text{SAS}}$ and α , the relationship between $[\text{Chl } a]_{\text{SAS}}$ and *in situ* $[\text{Chl } a]_{\text{fl}}$ was poorly described by a linear relationship within the range of chlorophyll concentrations sampled (Figure 10c), and the relationship between α and $[\text{Chl } a]_{\text{fl}}$ was much worse (not shown). Two regimes existed in the cross-plot of $[\text{Chl } a]_{\text{SAS}}$ and $[\text{Chl } a]_{\text{fl}}$ which could be differentiated by their location along the transect, suggesting water masses of differing bio-optical properties (Figure 10c). The observations of $[\text{Chl } a]_{\text{SAS}}$ values derived from the OC-4 algorithm were consistently lower than the shipboard fluorometric measurements of chlorophyll concentration. Despite the relatively poor relationship between $[\text{Chl } a]_{\text{SAS}}$ and $[\text{Chl } a]_{\text{fl}}$, these measurements represent a small portion of the complete range of ocean chlorophyll concentrations used to generate OC-4, and were well within the error of the algorithm as determined from the NOMAD validation dataset (Figure 10d).

Similar to our observations in the Mid-Atlantic Bight, the relationship between α and a_{pg} measured during the Gulf of Maine transect was linear (Figure 11, Table 3). However, the slope of this relationship was significantly different than the relationship observed between α and a_{pg} measured during the Mid-Atlantic cruises (ANCOVA, $p = 0.0046$, Table 4).

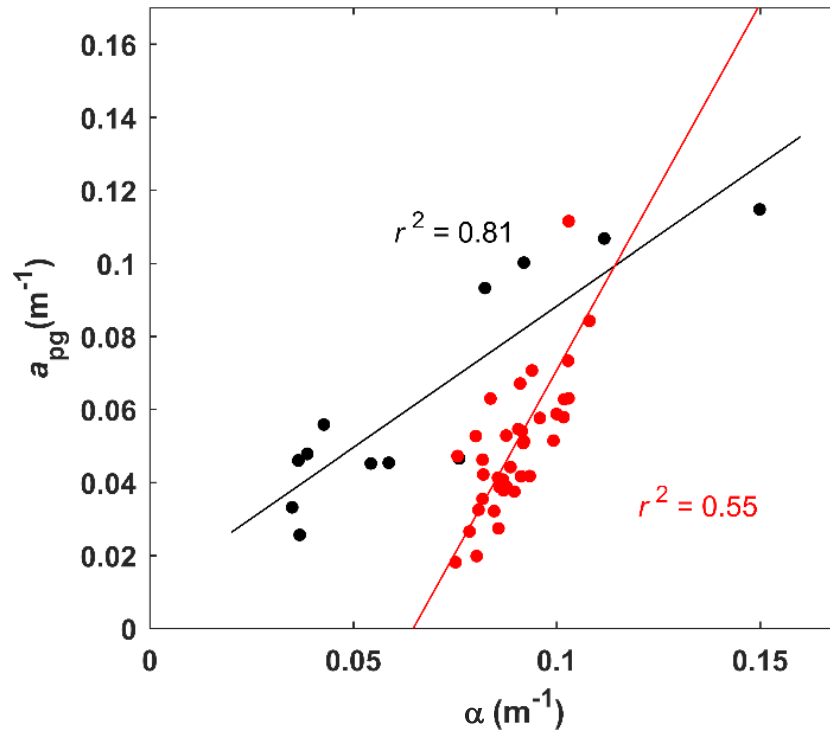


Figure 11. a_{pg} versus α relationships observed for the Mid-Atlantic Bight and the Gulf of Maine. Black symbols and line refer to the Mid-Atlantic Bight measurements, red symbols and line refer to the Gulf of Maine measurements.

Table 4. Summary ANCOVA table comparing the relationship between a_{pg} and α between the Mid-Atlantic Bight and the Gulf of Maine.

Dependent Variable	Source of Variation	df	SS	MSS	F	p
a_{pg}	Location	1	0.00805	0.00805	49.18	< 0.001
	α	1	0.0136	0.0136	82.95	< 0.001
	Location * α	1	0.00146	0.00146	8.91	0.0046
	Error	45	0.00736	0.00016		

DISCUSSION

The findings presented here demonstrate that ship-based oceanographic lidar can remotely map the vertical and horizontal distribution of important optical and biogeochemical properties in productive coastal waters. Similar to the early investigations of oceanographic lidar by Hoge et al. (1988), our lidar system resolved horizontal and vertical gradients in α from a variety of water types. Furthermore, coincident observations of water column properties measured via a suite of *in situ* (ship flow-through, profiling package, and glider) and remote sensing (shipboard radiometer, MODIS) tools showed that the features observed by the lidar were spatially consistent with measured gradients in both water column optical and biogeochemical properties.

The correlation between α and $[\text{Chl } a]_{\text{SAS}}$ along the GoM transect demonstrated the potential for the use of shipboard lidar in mapping phytoplankton distributions in the upper ocean. However, the lack of a significant relationship between α and coincident estimates of $[\text{Chl } a]$ from MODIS and the flow-through fluorometer highlight some important considerations to be made when reconciling data products derived from remote sensing (e.g. α , $[\text{Chl } a]_{\text{SAS}}$, $[\text{Chl } a]_{\text{MODIS}}$) in the context of *in situ* oceanographic measurements. The variety of $[\text{Chl } a]$ measurements employed here were characterized by very different spatial and temporal scales, none of which were truly representative of the sampling scale of the lidar. The MODIS estimates relied on a signal integrated over the upper ~ 2 optical depths and averaged across a 1 km^2 pixel, while α represents the average lidar signal decay over a range of relatively constant attenuation, in this case ~ 2 optical depths (Gordon and McCluney 1975; Kovalev and Eichinger 2004) and horizontal distance averaging of 0.6 km during the 1 minute of lidar sampling at 37 km h^{-1} (20 kts). The upper water column across the GoM transect was found to be relatively vertically homogenous, and thus each α value represents an average over the entire sampling range (~ 2 optical depths), likely explaining the

similar behavior of α and the shipboard remotely sensed chlorophyll (SAS). Had vertical layers of different chlorophyll a concentrations been encountered across the GoM transect, the relationship between α and $[\text{Chl } a]_{\text{SAS}}$ may have deteriorated significantly from what we observed here (Hill and Zimmerman 2010; Zimmerman et al. 2013). Since the MODIS chlorophyll product is derived from the same principles as the shipboard radiometer, the strong relationship between α and $[\text{Chl } a]_{\text{SAS}}$, but not between α and $[\text{Chl } a]_{\text{MODIS}}$ is likely due to the disparity between the spatial sampling scales of the two systems (1 km^2 for MODIS vs $\sim 0.0022 \text{ km}^2$ for SAS). The relatively small range and low concentrations of chlorophyll a (~ 1 to 5 mg m^{-3}) observed over our sampling region further contributed to the lack of correlation, as the 0.15-0.25 RMSLE (root mean square logarithmic error) of typical ocean color algorithms can produce an order of magnitude of uncertainty in chlorophyll estimates at these concentrations (O'Reilly et al. 1998).

As developed above, α from a single-wavelength lidar may be valuable as a proxy for chlorophyll concentration in systems where light attenuation and chlorophyll concentration are tightly coupled. However, this relationship will likely break down in waters where light attenuation by other absorbing and scattering components (CDOM, suspended sediment, detritus, etc.) does not co-vary with chlorophyll concentration. Passive remote sensing techniques typically approach the deconvolution of the remote sensing reflectance signal into the contribution of absorbing and scattering components by analysis of the spectral shape of the return signal (Garver and Siegel 1997), an approach that works well in the open ocean, but tends to overestimate chlorophyll concentrations in optically complex waters (Harding et al. 2005). However, the observed covariation of the lidar depolarization measurements with *in situ* measurements of $b_{\text{bp}}/b_{\text{p}}$, an IOP that can serve as a proxy for the bulk composition of scattering particles in the water column, may provide a method for attributing changes in single wavelength lidar attenuation to changes in both

bulk particle concentration and composition without the use of a multi-wavelength system (Twardowski et al. 2001; Boss et al. 2004).

The angular distribution of scattering by particles in the ocean is related to both the particle size distribution (PSD) and refractive index, where particle assemblages of elevated refractive index and decreased PSD slopes tend to produce higher b_{bp}/b_p (van de Hulst 1957). Since organic particles tend to have lower refractive indices than inorganic mineral particles, measurements of b_{bp}/b_p can serve as a proxy for the relative contribution of organic and inorganic particles to light scattering (Aas 1996; Twardowski et al. 2001; Boss et al. 2004). The extent of depolarization of incident linearly polarized light also tends to increase with increased particle refractive index due to an increase in the occurrence of multiple internal reflections within non-spherical particles (Sassen 2005). Thus, it may be possible to develop a relationship between the depolarization ratio and the bulk refractive index of the particles in the water column, allowing for determination of the relative contribution of organic particles to the backscattering signal (Twardowski et al. 2001). However, the scattering of a single photon off multiple particles in the water column can also contribute significantly to depolarization, complicating our interpretation of the depolarization signal for the retrieval of the material properties when particle concentrations are high (Bissonnette 2005). Thus, the relative contribution of the sources of multiple scattering to the signal depolarization must be understood in order to fully exploit lidar depolarization as a proxy for the material composition of scattering particles.

Developing robust relationships between α and water column optical properties has long been a goal of oceanographic lidar research. Previous modeling and experimental efforts aimed at developing these relationships show that the value of α can lie anywhere between a and c owing to the complex dependency of α on the FOV, lidar beam width, the depth of retrieval, and the

water column optical properties; (Gordon 1982; Walker and McLean 1999; Allocca et al. 2002). This simultaneous dependence of the lidar return signal on a variety of water column and system variables has plagued historical attempts at developing robust relationships between α and water column optical properties, and the results presented here are a further example of this variable property of the lidar return signal. The similarity in magnitude of α and measured a_{pg} at each station is consistent with the idea that the relatively large FOV of our lidar system (14° full-angle) should result in values of α approaching a , especially for shallow optical depths (Walker and McLean 1999). The relationship between α and a_{pg} held significant predictive power in each of the two testing regimes, however the slope of this relationship was specific its sampling scheme. This result is likely due to differences in deployment geometries (height above water & nadir angle), which can affect the behavior of α through their influence on the instrument field of view, beam diameter, overlap function, and the range to the sampling volume. The sensitivity of lidar systems to the manner in which they are deployed has major implications for the development of lidar algorithms for multi-platform instruments, as they are likely to be specific to the geometry of the deployment as well as the instrument's source/detector geometry.

Although the lidar system proved useful for retrieving a variety of interesting water column optical and biogeochemical properties, the α measurements made in this study were systematically lower than a_{total} ($= a_{pg} + a_{water}$), violating what is thought to be the lower limit on the magnitude of lidar attenuation values (Walker and McLean 1999; Allocca et al. 2002). The design, packaging, and deployment constraints associated with the lidar developed here impose some unique sensitivities on the system which may account for this discrepancy. Given that the solid angle subtended by a detector decreases as a negative exponential function of range, the return signal from a near-field lidar system such as this one is much more sensitive to the range-squared

correction than systems deployed from airborne or spaceborne platforms. This characteristic of the lidar system makes the accurate determination of time-zero a critical effort, since a small error in the determination of range can lead to a large error in the magnitude of range-corrected α . In order to make useful sense of return signals from near-field lidar systems such as this, it is also critical to either characterize the instrument's overlap function or to design the system such that the range to complete overlap is minimized. Characterization of the lidar overlap function is a non-trivial exercise due to the complex dependencies of the function on system alignment, the energy distribution in the laser spot, and spreading of the beam and field of view due to refraction at the sea surface and multiple scattering within the water column (Sassen and Dodd 1982). As was presented here, the range to complete overlap can be significantly reduced by minimizing the laser divergence and using a detector that has a sufficiently large FOV. Finally, space charge build-up in the PMTs in response to strong return signals can induce a noise tail in the decay signal, systematically depressing retrieved values of α (Pettifer 1975; Cairo et al. 1996). The simultaneous dependence of this "signal induced noise" (SIN) on both signal strength and duration makes it difficult to characterize and correct for the contribution of this response to the total return signal (Acharya et al. 2004). However, the contribution of SIN to the return signal could be minimized through a variety of hardware modifications such as the addition of a pre-amplifier at the PMT output, physical or electrical gating of the PMT to exclude strong return signals from the instrument window or sea surface, or through the use of detectors that are designed to minimize the effects of signal induced noise on the return signal.

Despite its utility in reducing the range to complete overlap, the relatively large FOV of the lidar system described here allows for the increased contribution of multiply scattered photons to the return signal, violating the single scattering assumption that is implicit in the lidar equation.

This complicates the determination of range from the signal time of flight since the pathlength of a photon is only directly proportional to range from the lidar in a single scattering regime. Multiple scattering leads to an overestimate of range and an apparent decrease in attenuation known as “pulse stretching” (Miller and Stephens 1999; Walker and McLean 1999; Bissonnette 2005). In general, the return signal can be considered to violate the single scattering time-of-flight assumption as the FOV footprint increases to greater than the mean free path of the photon ($1/c$), which equates to a distance of less than 1 m from the lidar face at our most turbid station and 14 m for our clearest station. Thus, the inclusion of multiply scattered photons in the return signal likely plays some partial role in lowering the magnitude of α measured during these field campaigns. Decreasing the lidar FOV will minimize the detector footprint, decreasing the multiple scattering contribution to the signal and reducing the effects of pulse-stretching on the interpretation of the signal, consequently increasing α .

Despite the uncertainty introduced by the inclusion of multiply scattered photons in the interpretation of α , the multiple scattering signal contains some potentially valuable information on the material properties of the water column. As we showed above, the depolarization ratio may provide some valuable information on the composition of scattering particles in water column, as the relationship found between b_{bp}/b_p and ρ shows promise for the application of this theory to the remote sensing of bulk particle composition. In order to exploit the information contained in the depolarization signal, however, it will be necessary to separate the multiply scattered photons from those directly backscattered to the detector by the medium. The multiple field of view (MFOV) lidar technique offers a potential solution to this problem. Successive reduction of the lidar FOV minimizes the contribution of multiply scattered photons to the return signal. Thus signal depolarization results increasingly from changes in the material properties of the scattering volume

as FOV decreases (Bissonnette 2005). Further, the relationship between range-gated signal strength and FOV can be related to the particle size distribution and forward scattering phase function of the scattering medium (Bissonnette 2005). Inversion of polarized MFOV lidar measurements thus can be used to explore particle size and material properties, a method which has been successfully applied in atmospheric studies but has been under-investigated for use by the oceanographic community. The requirement for the MFOV lidar technique to make multiple measurements of the same water parcel makes it particularly well suited for lidar systems deployed on static moorings or relatively slow-moving vessels, as opposed to airborne or orbiting platforms that must operate at high ground speeds.

Large-scale observing systems are becoming fundamental to addressing the current goals of the oceanographic community, and the rapid development of sensor and sampling platform technology for improving the quality and scope of these systems has been a highly active area of research (Doney et al. 2004; Siegel et al. 2016). Due to the active nature of lidar, integration of these systems into routine ocean sampling regimes can lead to cost-effective improvements in sampling resolution, especially when sampling constraints often limit data retrieval to surface measurements (“ships-of-opportunity”, buoys, surface AUVs) (Schofield et al. 2002; Codiga et al. 2012; Cross et al. 2015). The ability to retrieve real-time vertical information while underway could also prove useful in optimizing adaptive sampling campaigns aimed at studying temporally and spatially transient oceanographic features. As lidar technology becomes increasingly rugged, compact, energy efficient, and inexpensive, regular deployment of these systems on a variety of platforms becomes increasingly practical, allowing for continuous remote sensing of the vertical and horizontal distribution of particles in the ocean. This has the potential to resolve the large errors in remotely sensed estimates of primary production and carbon flux associated with the

integration of the upper water column signal, an intrinsic property of passive ocean color remote sensing systems (Weston et al. 2005; Hill and Zimmerman 2010; Schulien et al. 2017).

CHAPTER III

INSIGHTS FROM A MESOSCALE COCCOLITHOPHORE BLOOM

PREFACE

A modified version of this chapter was published by the Optical Society of America (OSA) in the journal Applied Optics (<https://doi.org/10.1364/AO.389845>). The right to reproduce this article in theses or dissertations is retained by the author under the OSA author rights agreement.

INTRODUCTION

Shipborne lidar systems, such as the one developed in the previous chapter, have the potential to fill two important roles in the ocean sciences: (i) the ability to directly characterize the relationship between lidar return signals and water column properties with *in situ* measurements makes them ideal development platforms for advancing airborne and spaceborne lidar technology, and (ii) the ability to measure the vertical distribution of optical properties remotely from underway surface vessels makes them ideal for studying small-scale features where station-based profiling would restrict horizontal sampling resolution. Several examples of the former application have been presented in the literature, where shipboard lidar measurements have been used in conjunction with station-based sampling techniques to develop relationships between lidar and in-water measurements (Lee et al. 2013; Collister et al. 2018; Liu et al. 2019a). However, the ability of lidar to supplement continuous underway surface sampling efforts with vertical profiles and information on the polarized light scattering properties of particles has not yet been fully explored. The goal of this Chapter was to explore the ability of lidar for describing the distribution of upper ocean optical and biogeochemical properties over a wide range of oceanographic conditions.

METHODS

The CoccoMix Expedition

The shipboard oceanographic lidar system that was developed in (Collister et al. 2018) was deployed from 4 to 15 July 2018, as part of the 2018 CoccoMix expedition aboard R/V *Endeavor* (cruise number EN616). Although the primary research objective of the expedition was to investigate the trophic modes of coccolithophores and to complete a section of the Gulf of Maine North Atlantic Timeseries, the expedition provided us with a unique opportunity to explore the oceanographic lidar return signal from a variety of optically and biogeochemically distinct water masses. These included sediment and diatom-rich coastal waters, clear waters south of the New England Shelf Break, and a dense mesoscale coccolithophore bloom that occurred in the southern half of the Gulf of Maine (Figure 12a). The oceanographic lidar system was mounted looking downward through the portside bow chock of the ship at a mean angle of 35° from the vertical and a height of 4.3 m above the waterline (Figure 12b), providing a laser spot and receiver field of view (FOV) that were undisturbed by the ship's wake.

Lidar Sampling

Lidar profiles were collected at five-minute intervals along the track, except for periods when the instrument was taken offline for maintenance or instrument malfunctions prevented data acquisition (Figure 12a). Each lidar profile was constructed by averaging 100 laser pulses at each of a series of six increasing PMT gain settings, totaling 600 measurements per sequence obtained in about one minute. The multiple gain settings allowed us to extend the depth range of the instrument, which was limited by the digital resolution and 0V to -2.5V to input range of the high-speed digitizer. The lowest PMT gain setting was set to well below the threshold for signal

detection, and was used as a dark correction to account for electrical noise. The maximum gain setting was set manually, and was periodically adjusted to prevent the digitizer from being overloaded. The remaining gain settings were fixed across all measurement sequences. At the sampling interval of five minutes and the average underway ship speed of 13 km hr^{-1} , the horizontal spacing between consecutive lidar measurements was on the order of 1 km. At that average speed, the ship covered a horizontal distance of $\sim 0.2 \text{ km}$ during each measurement sequence. Each lidar pulse was time-tagged and matched with GPS position data provided by the ship's navigation system.

Lidar profiles were reconstructed from measurements made at multiple gain settings as described in Collister et al. (2018). For regions of approximately homogenous optical properties, the lidar attenuation coefficient (α) was calculated using the slope method (Kovalev and Eichinger 2004). Due to the limited dynamic range of the system, there was very little overlap between regions of co-polarized signal [$S_c(r)$] and cross-polarized [$S_x(r)$] that were both unsaturated and above the SNR threshold. For this reason, values of α were calculated using only the co-polarized channel. The signal depolarization ratio (δ) was calculated at a single PMT gain setting which was held constant throughout the expedition as:

$$\delta = 1.052 \frac{S_x}{S_c} \quad \text{Eq. 3}$$

where the constant 1.052 corrected for the split-ratio of the beam splitter ($T_p:R_s = 0.95$). Due to the limited spatial overlap of $S_c(r)$ and $S_x(r)$, calculations of δ were made at a single range along the beam from the sea surface of 6.5 m, where signal fidelity and overlap between $S_c(r)$ and $S_x(r)$ at the common gain setting was maximum.

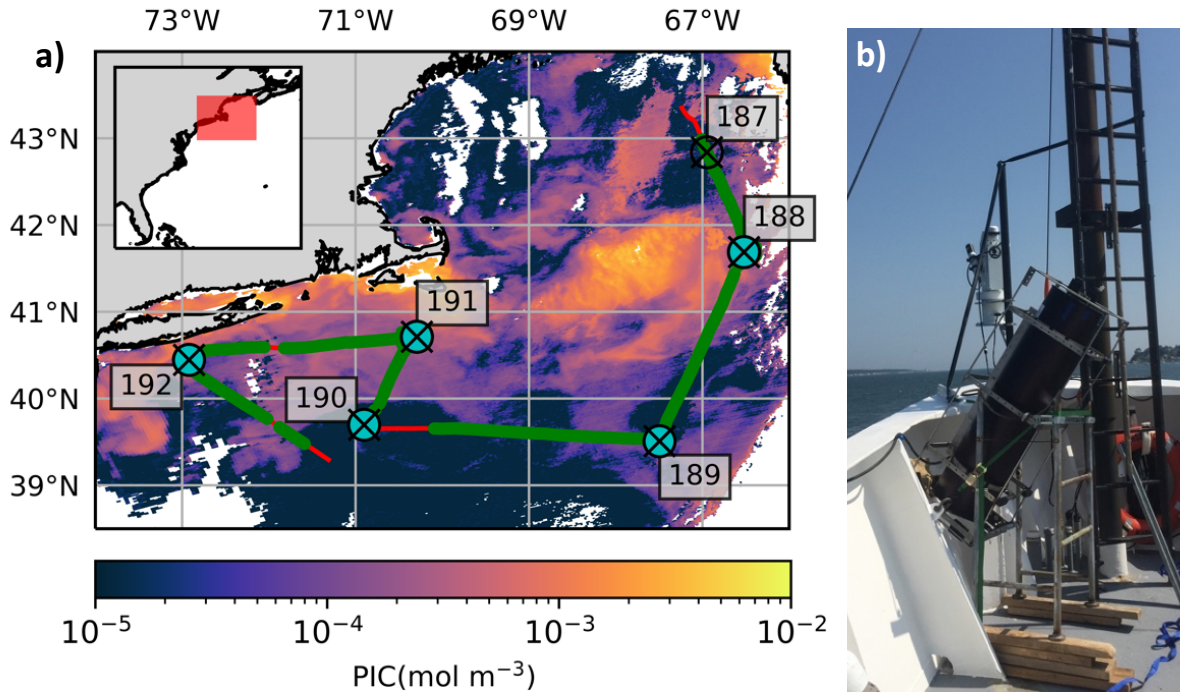


Figure 12. Map of the CoccoMix expedition and picture of the lidar installed at the bow of R/V *Endeavor*. Track of the 2018 CoccoMix expedition plotted over a heat map of particulate inorganic carbon concentration based on the NASA two-band/three-band merged PIC algorithm (Gordon et al. 2001; Balch et al. 2005) from a 13 July 2018 MODIS-Aqua image. Green segments of the track indicate where lidar data were collected; no lidar data were collected along the red segments. Hydrographic stations are indicated by the symbols and identified by their calendar day in gray boxes. The symbols at each station denote measurements that were made at each station. CTD stations are denoted by open circles, HyperPro casts by filled blue circles, and lidar stations by an “X”. To orient the reader, the inset map shows the United States/Canada Eastern Seaboard with the study region delimited by a red box. b) Photograph of the oceanographic lidar system installed at the bow of R/V *Endeavor*.

Underway water sampling

Bio-optical and hydrographic properties of the surface waters were measured continuously while underway using a flow-through sampling system installed in a portable lab fixed to the back deck of the R/V *Endeavor*. This sampling system has been described extensively in previous publications (Balch et al. 2004), but aspects relevant to this investigation are worth repeating here for clarity. The flow-through system was plumbed into the ship's flowing seawater system, which draws water through an intake in the hull located at 5 m depth. One *ac-9* spectrophotometer (WETLabs), was used to measure the spectral absorption and attenuation coefficients of dissolved material (a_g and c_g) and particulate + dissolved material (a_{pg} and c_{pg}), sequentially, as a solenoid valve alternated between filtered $<0.2 \mu\text{m}$ and unfiltered, raw seawater, respectively. The difference between consecutive $a_{pg}(\lambda)$ and $a_g(\lambda)$ measurements provided an estimate of $a_p(\lambda)$, and similarly, the difference between consecutive $c_{pg}(\lambda)$ and $c_g(\lambda)$ provided $c_p(\lambda)$. The particulate scattering coefficient [$b_p(\lambda)$] was then calculated as $b_p = c_p - a_p$. The symbol λ denotes wavelength and unless otherwise stated, all optical measurements presented here refer to the value at the lidar wavelength of 532 nm. The total seawater absorption coefficient (a) was calculated as $a = a_{pg} + a_w$, where a_w refers to the absorption coefficient for pure water (Pope and Fry 1997), and the total seawater scattering coefficient (b) was calculated as $b = b_p + b_{sw}$, where b_{sw} is the scattering coefficient of pure seawater modeled from underway measurements of temperature and salinity (Zhang et al. 2009). The single scattering albedo was then calculated as $\omega_0 = b/c$, where c is the total attenuation coefficient including absorption and scattering by pure seawater ($c = a + b$). Measurements of the volume scattering function (VSF) were made at 18 discrete angles using a DAWN EOS (Wyatt Technology Corporation) multi-angle light scattering meter. The backscattering coefficient (b_b) was calculated by integrating over the VSF in the backward

direction, and the total backscattering ratio (\tilde{b}_b) was calculated as $\tilde{b}_b = b_b/b$. Acid-labile backscattering (b_b'), an optical proxy for the concentration of suspended particulate inorganic carbon ([PIC]), was calculated from the loss of b_b upon dissolution of suspended PIC by acidification below the dissociation point of calcite (Balch et al. 2004). For comparison with lidar measurements, all underway measurements were interpolated to the lidar sampling interval using a cubic spline.

To allow for comparison with underway lidar measurements of α , K_d at 532 nm was estimated from the underway IOP measurements as:

$$K_{d,s} = (1 + 0.005\theta_z)a + 4.18b_b [1 - 0.52\exp(-10.8a)] \quad \text{Eq. 4}$$

where $K_{d,s}$ refers to the underway surface estimate of K_d and θ_z is the solar zenith angle in degrees (Lee et al. 2005). Similar to previous comparisons between α and K_d , we assumed θ_z to be at zenith for calculations of $K_{d,s}$ (Gordon 1982). The theoretical lower bound on values of K_d for optically pure seawater (K_{dw}) was calculated using the radiative transfer model *HydroLight* [Sequoia Scientific, Ver. 4.2, Mobley (1989)] over the upper 15 m of an optically homogenous, infinitely deep water column, using the pure water absorption coefficient of Pope and Fry (1997).

Hydrographic Stations

Ten hydrographic stations were occupied over the course of the expedition, six of which were concurrent with measurements made using the oceanographic lidar system (Figure 12a). Vertical profiles of temperature and salinity were measured using a CTD (Sea-Bird Scientific; SBE-911+) deployed on the ship's rosette system, and used to characterize the density structure of the upper water column. A free-falling, profiling radiometer package (Satlantic HyperPro) was used to measure profiles of spectral downwelling irradiance [$E_d(z)$] through the upper water

column at all stations except for Station 187, where the sea state prohibited deployment. A reference irradiance sensor (Satlantic HyperOCR) mounted to a mast on the 01-level of the ship provided a simultaneous record of the downwelling irradiance above the sea surface (E_s) to correct for transient cloud effects. The diffuse attenuation coefficient (K_d) was calculated from the slope of a linear regression as:

$$K_d = -\frac{d}{dz} \ln [E_d(z)] \quad \text{Eq. 5}$$

Each profile of $E_d(z)$ was measured within an hour of local noon to control for the influence of the solar zenith angle on K_d . For comparison with α , the depth range over which $K_d(\lambda)$ was calculated was taken to be the range of depths at which the corresponding lidar profile was both unsaturated and above the signal-to-noise limit cutoff. In cases where $\ln(E_d)$ remained linear beyond the lidar depth limit, K_d was calculated over the entire linear region in order to improve the statistical power of the measurement.

RESULTS

The Optical Context

After departing Rhode Island and transiting across the Gulf of Maine, the cruise track turned south and crossed through a dense coccolithophore feature that was confirmed using polarized microscopy of live samples aboard the ship using the filter-freeze-transfer technique (Hewes and Holm-Hansen 1983), post-cruise coccolithophore enumeration using polarized microscopy of samples on Millipore HA filters (Poulton et al. 2010), as well as post-cruise scanning electron microscopy of samples to identify coccolithophore species (Goldstein et al. 2017). Station 188 was within this feature which was situated over Georges Bank (Figure 12a). The track across the coccolithophore feature (7 to 8 July 2018) was characterized by high values

of b and ω_o , and a slight increase in the total backscattering ratio over values measured in the region just prior to the coccolithophore feature (Figure 13a, b). Moreover, the coccolithophore feature was clearly delineated by elevated values of acid-labile backscattering (b_b') that were an order of magnitude higher across the coccolithophore feature than anywhere else along the track (Figure 13e). The acid labile fraction of backscattering (b_b'/b_b) increased from ~ 0.15 along the Gulf of Maine portion of the track to as high as 0.52 within the coccolithophore feature, accounting for over half of the total b_b (Figure 13f).

After crossing the dense coccolithophore feature, the track headed west at Station 189, crossing through waters just south of the New England shelf break that were characterized by low PIC concentrations (Figure 12a). Much of the optical variability along this portion of the track was associated with mesoscale features that developed along the northwest boundary of the Gulf Stream (Figure 12a). Values of b within this region ranged from 0.10 m^{-1} to 0.30 m^{-1} , with the highest values occurring within two features (~ 45 and 15 km wide respectively) west of Station 189, and the lowest values occurring around Station 190 (Figure 13a). The increase in scattering within the two mesoscale features west of Station 189 was associated with an increase in both ω_o and b_b , and a decrease in \tilde{b}_b (Figure 13b-e). The region of decreased scattering around Station 190 showed a distinct decrease in ω_o and an increase in the backscattering ratio ($\tilde{b}_b = \frac{b_b}{b}$), with small-scale features apparent in each of these measurements. The lowest values of b_b' measured along the track occurred within the region, where b_b'/b_b ranged from 0.03 to 0.06 (Figure 13e, f).

Values of b , ω_o , and b_b' increased as the track turned northeast from Station 190 onto the shelf just south of Martha's Vineyard (Figure 12a, Figure 13). Although the values of b and ω_o in the shelf region were similar to values observed within the Georges Bank coccolithophore feature astride Station 188, there were distinct differences in the angular distribution of scattering as well

as the nature of the particle assemblage (Figure 13). In general, \tilde{b}_b was lower on the shelf region than within the Georges Bank coccolithophore feature (Figure 13d). The highest values of b_b' in the shelf region corresponding to Stations 191 and 192 were only 13% of the peak b_b' values measured within the coccolithophore feature. Although the values of b_b' were similar at Stations 191 and 192, the fractional contribution of PIC to b_b was greater at Station 191 ($b_b'/b_b \approx 0.20$) than at Station 192 ($b_b'/b_b \approx 0.08$) (Figure 13f). Unlike the coccolithophore feature, increases in b and ω_b measured within the shelf region were not always associated with increases in b_b' , suggesting fundamental differences in the nature of the particles within the shelf region and the coccolithophore feature (Figure 13a, e). The lack of an association between b_b' and b is especially evident in the region between Stations 191 and 192, where a large increase in b occurred in the absence of any increase in b_b' (Figure 13a, b, e, f).

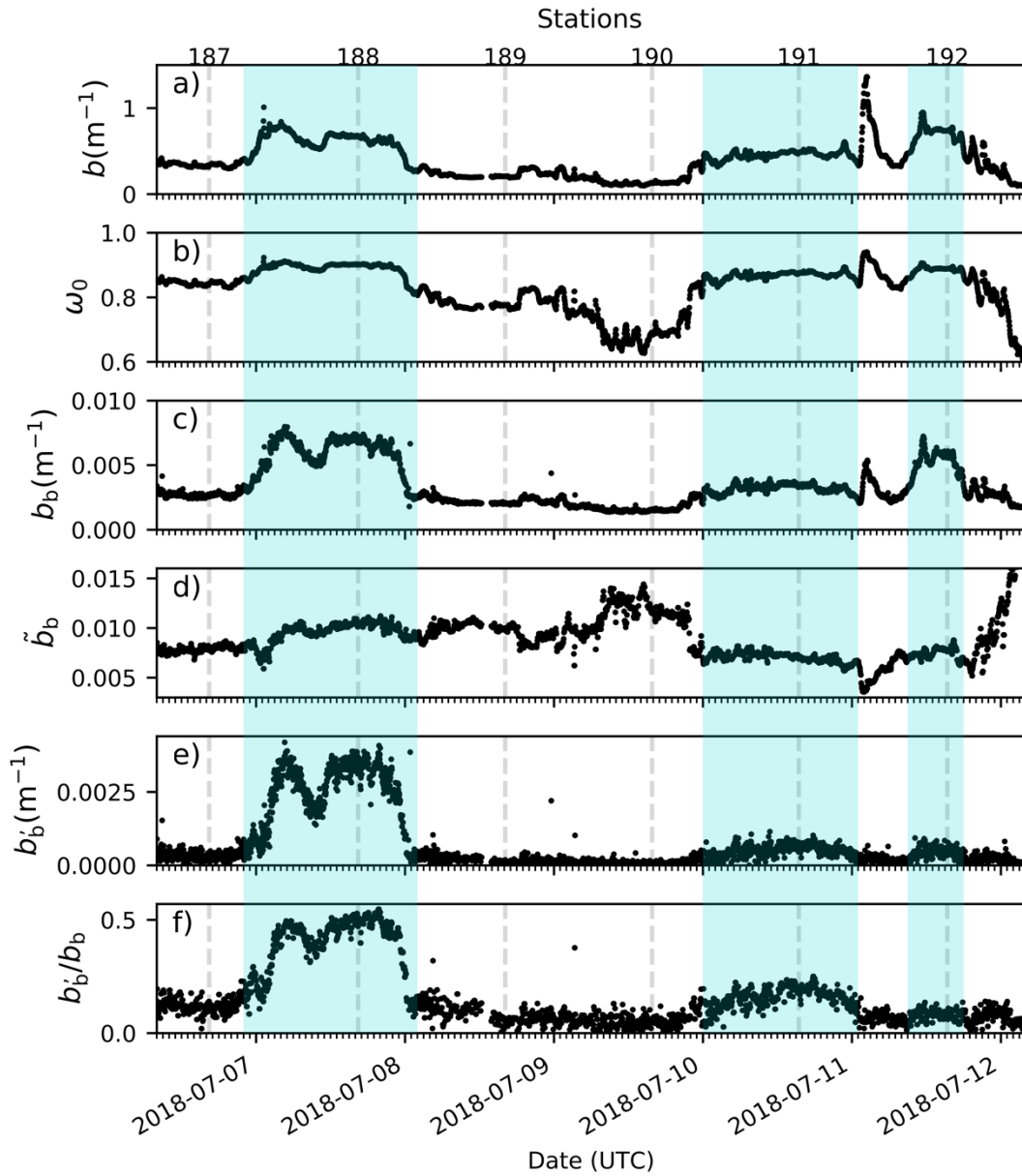


Figure 13. Time series plot of surface IOP measurements. a) scattering coefficient, b) single scattering albedo, c) backscattering ratio, d) acid-labile backscattering coefficient, and e) the fraction of backscattering attributed to PIC. Vertical dashed lines denote the temporal location of each hydrographic station, which are labeled above the top axis. Dates on the lower axis mark the beginning of each day in Coordinated Universal Time (UTC).

Lidar attenuation coefficient, α

Over the course of a 6-day period (6 to 12 July 2018), 1350 oceanographic lidar records were obtained at spatial and temporal scales comparable to those of the underway IOP measurements described above (Figure 12). Within the uncertainties of each measurement, *in situ* profiles of $E_d(z)$ and profiles of lidar signal exhibited constant logarithmic decay over the first optical depth at every station, suggesting that IOPs were vertically homogenous within the surface layer, and resulting in a single estimate of K_d and α from each profile. Vertical profiles of b_{bp} were also invariant within the first optical depth, further indicating the vertical homogeneity of the surface layer IOPs.

Consistent with *in situ* and underway measurements of optical properties described above, values of α were elevated within the Georges Bank coccolithophore feature and in the Mid-Atlantic Bight region near Long Island (around Station 192). Values of α were lowest in the offshore region south of the New England shelf break (Figure 12a, Figure 14). Patterns in α along the cruise track closely mirrored patterns in $K_{d,s}$ derived from underway IOP measurements and *in situ* HyperPro measurements of K_d performed at the individual stations (Figure 14), as well as the [PIC] heat map derived from the MODIS image (Figure 12a). The magnitude of α was also fairly consistent with both the *in situ* measurements of K_d and the underway measurements of $K_{d,s}$ (Figure 14). Note that measurements of α and $K_{d,s}$ do not include sun angle/diffuse skylight effects which are inherent in measured values of K_d , likely explaining some of the disparity between measured values of K_d and values of α and $K_{d,s}$. Although strongly correlated (Pearson $r = 0.86$), a cross-plot of lidar α against $K_{d,s}$ revealed the non-linearity of this relationship (Figure 15). The relationship between $K_{d,s}$ and α occurred along a range of ω_0 from 0.63 to 0.94, where ω_0 increased with increasing values of α and $K_{d,s}$ (Figure 15a). The α vs. $K_{d,s}$ relationship showed no consistent

response to large changes in either \tilde{b}_b or b_b/a (an indicator of “brightness”) associated with distinct optical regimes (Figure 15b, c). This was the case even within the coccolithophore feature, where local maxima in both \tilde{b}_b and b_b/a were associated with a large increase in b_b' over background levels, and produced discernable changes in the relationship between α and $K_{d,s}$ (Figure 15).

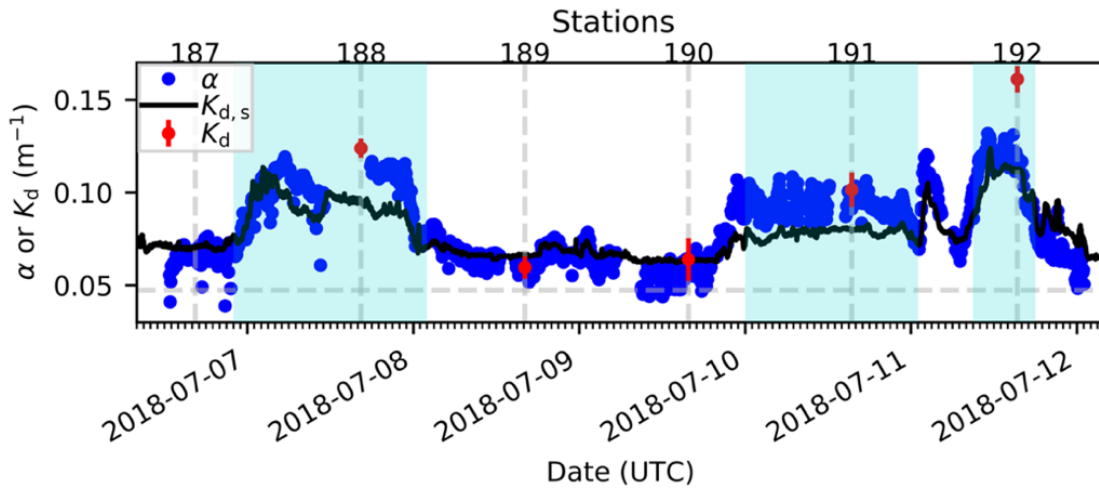


Figure 14. Time series plot of lidar and diffuse attenuation coefficients. The lidar attenuation coefficient (α) is denoted by (blue dots), diffuse attenuation derived from surface IOPs ($K_{d,s}$) by the black line, and diffuse attenuation estimates from profiles of $E_d(z)$ (K_d) by red symbols. Vertical red lines for K_d measurements represent 95% confidence interval of the regression slope between $E_d(z)$ and z . Vertical dashed lines denote the temporal location of hydrographic stations identified above the top axis. Dates on the lower axis mark the beginning of each day in Coordinated Universal Time (UTC). The horizontal grey line denotes the theoretical value of K_d for pure seawater as calculated using HydroLight (Sequoia Scientific) (Mobley 1989).

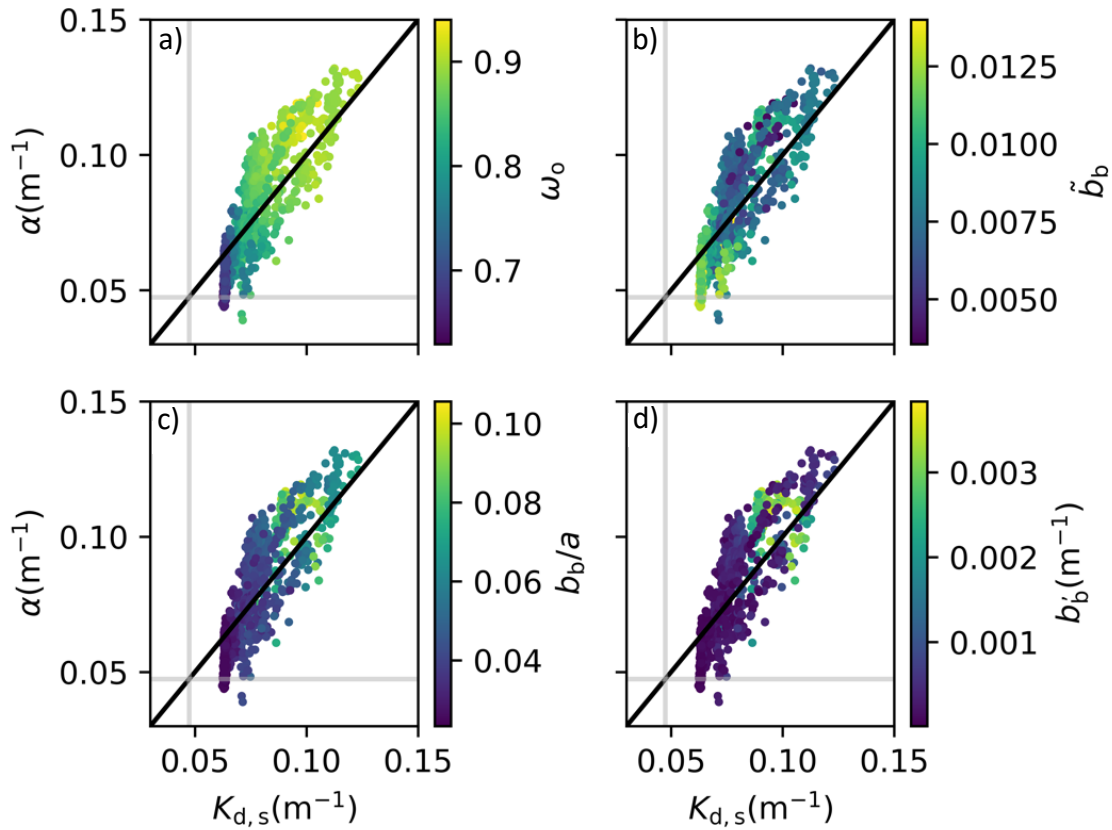


Figure 15. Plots of α vs. $K_{d,s}$. Color maps correspond with coincident values of a) ω_0 , b) \tilde{b}_b , c) b_b/a , and d) b'_b . The vertical and horizontal gray lines denote the theoretical value of K_d for pure seawater as calculated using *Hydrolight* (Sequoia Scientific, Mobley 1989).

Lidar depolarization ratio, δ

The lidar depolarization ratio (δ) closely followed the pattern of b'_b/b_b , reproducing even many small-scale features in the acid labile backscattering ratio (Figure 16). Measurements of δ were highest (~ 0.35) within the Georges Bank coccolithophore feature and were lowest (~ 0.11) in the region between the coccolithophore feature and the shelf waters (Figure 12a, Figure 16). A local maximum in both b'_b/b_b and δ also occurred within the shelf waters (10-11 July 2018), though

this peak in δ was at most 50% of the values measured within the Georges Bank coccolithophore feature. A secondary peak in δ also occurred after b_b'/b_b decreased back to values of ~ 0.1 (Figure 16). This increase in δ was associated with a sharp increase in b and ω_0 between Stations 191 and 192 and a shift in the nature of the particle assemblage away from calcified particles (Figure 13a, b, Figure 17).

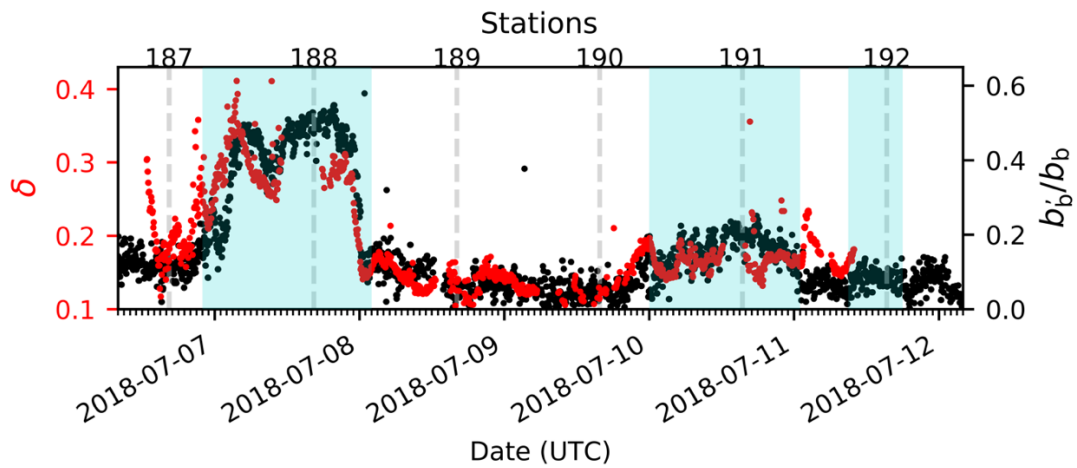


Figure 16. Time series plot of b_b'/b_b (black) and δ (red). Vertical dashed lines denote the location of each hydrographic station, which are labeled above the top axis. Dates on the lower axis are in Coordinated Universal Time (UTC).

To explore the combined effects of particle composition and multiple scattering on measurements of δ , I constructed a three-dimensional plot of δ versus b_b'/b_b , and δ vs. the scattering optical depth ($\ell_b = br$) to each measurement of δ (Figure 17). Measurements of b were converted to ℓ_b to emphasize that the contribution of multiple scattering to the signal increases with the number of scattering optical depths travelled by photons detected at some range. Depolarization

was linearly related to b_b'/b_b as illustrated by the δ vs. b_b'/b_b panel ($r^2 = 0.77$; RMSE = 0.031). However, the relationship between δ and ℓ_b displayed a clear bifurcation explained by one domain in the coccolithophore laden waters where b and b_b'/b_b were strongly correlated, and the other domain outside the coccolithophore laden waters where b was uncorrelated with b_b'/b_b (cf. Figure 13. and Figure 17). This separation of δ versus ℓ_b into two domains suggests that the relationship between δ and b_b'/b_b cannot be explained simply by multiple scattering effects, and that the intrinsic polarized light scattering properties of coccolithophores/coccoliths has a stronger effect on δ than multiple scattering alone. A bisquare robust multiple linear regression (two linear terms and an interaction term) of δ versus b_b'/b_b and ℓ_b returned an r^2 of 0.87 and an RMSE of 0.023, which is an improvement over a bisquare linear fit to δ versus b_b'/b_b ($r^2 = 0.77$; RMSE = 0.031) (Figure 17, Table 5). The interaction term of the regression was positive, where an increase in b_b'/b_b led to an increase in the slope of the δ vs. ℓ_b relationship, and an increases in ℓ_b led to an increase in the response of δ to b_b'/b_b (Table 5, Figure 17).

Table 5. Summary of bisquare robust regression model

Regression Model:	
$f(x,y) = j + kx + ly + mxy$; $x = b'_b/b_b$; $y = \ell_b$	
Model Parameter	Value \pm 95% CI
j	0.130 ± 0.0060
k	-0.123 ± 0.049
l	0.00859 ± 0.0020
m	0.0967 ± 0.012
Regression Statistic	Value
r^2	0.87
df	947
RMSE	0.0234
SSE	0.518

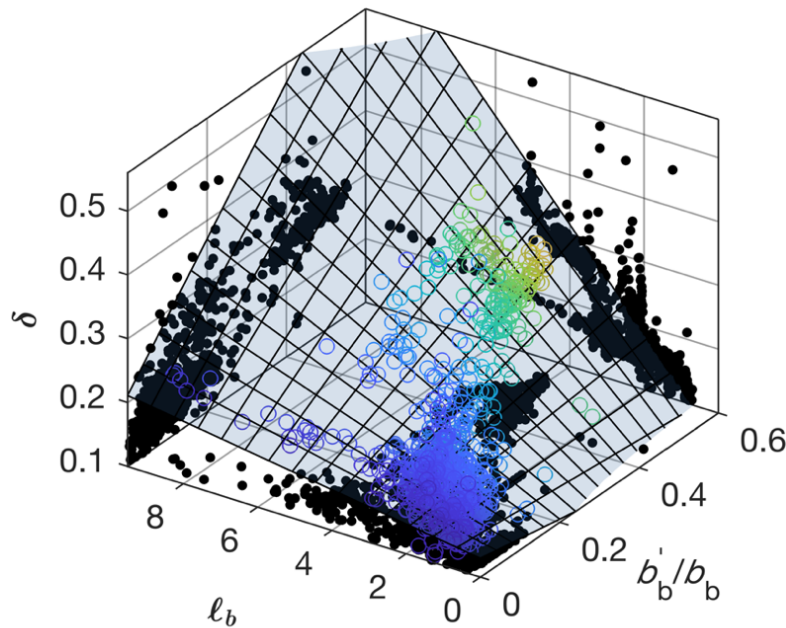


Figure 17. A three-dimensional plot of δ versus ℓ_b and b'_b/b_b . The color map corresponds with values of b'_b/b_b . Black dots represent projections of the data onto the δ versus b'_b/b_b (left), δ versus ℓ_b (right), and ℓ_b versus b'_b/b_b (bottom) planes. The mesh plane represents the results of a multiple regression of the form $f(x,y) = j + kx + ly + mxy$; $x = b'_b/b_b$; $y = \ell_b$. The resulting regression statistics are presented in Table 5.

DISCUSSION

The results presented here highlight the unique capability of polarized oceanographic lidar to map the distribution of biogeochemically relevant materials in the ocean at high spatial resolution. Spatial patterns in α were consistent with those of K_d whether measured directly or derived theoretically from IOP measurements. Understanding the relationship between α and K_d is critical for developing lidar into a useful oceanographic tool, and the shipboard lidar scheme allowed us to examine this behavior with an unprecedented number of coincident *in situ* observations. Consistency in the spatial patterns of δ and b_b'/b_b suggests that polarized oceanographic lidar can be used to map the abundance of scattering particles in the upper ocean and provide insight into the material nature of the scattering particles, all from a single measurement. The ability to make lidar and *in situ* optical measurements with identical spatial and temporal resolution revealed complexity in the behaviors of both α and δ that may not have otherwise been apparent, highlighting perhaps the greatest advantage of the ship-based lidar scheme. Exploring the complexity of these behaviors will improve our ability to meaningfully interpret the return signals from oceanographic lidar system and may allow for the development of new algorithms to retrieve optical properties related to the intensive (i.e. concentration independent) and extensive (i.e. concentration dependent) properties of upper ocean particle assemblages. Spatiotemporal mismatch between airborne lidar measurements and ship-based *in situ* measurements has been a major limiting factor in previous efforts to constrain this complexity (Lee et al. 2013; Schulien et al. 2017), and ship based lidar systems offer to bridge the gap between *in situ* measurements and those made from airborne/spaceborne platforms.

The curvilinear relationship found here between α and K_d adds to a growing body of literature that highlights the complex dependency of α on both the optical properties of the water

column and the characteristics of the lidar system (Gordon 1982; Walker and McLean 1999; Montes et al. 2011; Liu et al. 2018; Liu et al. 2019a; Zhou et al. 2019). The magnitude of ω_0 appeared to play a role in controlling the behavior of α , as evidenced by the large gradient in ω_0 that occurred across α - K_d space and the lack of a response to the large increases in \tilde{b}_b and b_b/a associated with the coccolithophore feature (Figure 15). These results are consistent with Gordon's original investigation into the effects of multiple scattering on the behavior of α , which showed a strong dependence on ω_0 , and a significant but much weaker dependence on the shape of the volume scattering function (Gordon 1982). Another possible explanation for this behavior is a non-ideal transient recovery of the PMT detectors, an effect which results in a slowly decaying noise tail, and an apparent decrease in attenuation at low signal-to-noise ratios (Williamson and De Young 2000; Acharya et al. 2004; Lu et al. 2014). However, a similar curvilinear relationship between α and $K_{d,s}$ was observed in a separate shipboard lidar study, which compared measured values of α with a model parameterized from concurrent IOP measurements [see Ref. (Liu et al. 2019a)]. Although the study by Liu et al. did not present the IOP measurements explicitly, the strong linear agreement between measured and modeled values of α provides some confidence that α is responding to changes in the IOPs, and is not simply an instrumentation effect (Liu et al. 2019a). The similarity in the behavior of α and K_d described in these two shipboard lidar studies begs the question of whether this is a unique characteristic of shipboard lidar, or if airborne systems display similar dependencies.

For airborne lidar systems with receiver spot sizes that are $> 1/c$ at the sea surface, the Gordon study (Gordon 1982) is commonly cited as rationale for neglecting the complex dependency of α on water column IOPs and assuming an equivalence between α and K_d (Gordon 1982; Lee et al. 2013; Schulien et al. 2017; Hostetler et al. 2018). This simplification relies on the

assumption that the FOV is large enough over the range of detection to account for photons which have been spread from the beam due to multiple scattering. While a variety of investigations have shown this to be a reasonable approximation, the model from which it is derived is specific to airborne lidar systems with narrow FOVs that do not diverge appreciably over the range of detection (Gordon 1982; Lee et al. 2013; Schulien et al. 2017; Hostetler et al. 2018). Having fairly small detector spot sizes ($< 1\text{m}$) and large FOV angles, the measurement geometry of a typical shipboard lidar system is fundamentally different than that of an airborne or spaceborne system, precluding them from this simplifying assumption. Although one could reason that shipboard measurements of α should approach K_d as the divergence of the FOV exceeds the angular spread of the beam, the parameter space describing the response of shipboard lidar measurements to changes in the FOV and water column IOPs has not been explored completely. This has important implications for the use of shipboard lidar systems for algorithm development and calibration/validation efforts, as differences between shipboard, airborne, and spaceborne lidar measurement geometries are likely to lead to different responses of α to changes in water column IOPs. As the oceanographic lidar community pushes toward a space-based oceanographic lidar system, characterization of these differences will be an important effort, as shipboard lidar systems are set to play a major role in laying the groundwork for algorithm development (Jamet et al. 2019).

The positive correlation between δ and b_b'/b_b suggests that scattering by coccolithophores and their detached coccoliths results in a distinct depolarization signature that can be detected using polarized oceanographic lidar. While these results show some promise for the use of polarized oceanographic lidar for distinguishing between calcified and non-calcified marine particles, δ exhibits a complex dependency on both the intensive and extensive properties of the scattering medium, complicating the interpretation of the δ versus b_b'/b_b relationship (Vasilkov et

al. 2001). Photons that are detected after a single backscattering event will be depolarized according to the normalized 2,2 Mueller matrix element of the medium [$\mathbf{M}_{22}(\pi)$], making δ sensitive to the nature (i.e. shape, size, and composition) of the particle assemblage (Kouzoubov et al. 1999; Vasilkov et al. 2001; Gimmestad 2008). Multiple forward scattering also contributes to depolarization, leading to a characteristic increase in δ with increasing scattering optical depth as photons are rotated out of the co-polarized plane of the detector and depolarized according to the forward scattering Mueller matrix of the medium (Sassen and Petrilla 1986; Kouzoubov et al. 1999; Zege and Chaikovskaya 1999; Vasilkov et al. 2001; Churnside 2008; Liu et al. 2019b). Thus, the influence of multiple scattering makes δ sensitive to the extensive properties of the particle assemblage, that must be accounted for prior to using δ as a proxy for particle intensive properties (Sassen and Petrilla 1986; Kouzoubov et al. 1999; Zege and Chaikovskaya 1999; Vasilkov et al. 2001; Churnside 2008; Liu et al. 2019b). This effect is especially relevant for wide-angle FOV systems such as the one described here, as an increase in FOV leads to an increase in the relative contribution of multiple scattering to the return signal (Sassen and Petrilla 1986; Kouzoubov et al. 1999; Zege and Chaikovskaya 1999; Vasilkov et al. 2001; Bissonnette 2005; Liu et al. 2019b). Although techniques exist to separate the multiple scattering component of δ from the single scattering component, they typically rely on analysis of the change in δ with depth, information which could not be retrieved here due to the sensitivity and noise characteristics of our current lidar system (Vasilkov et al. 2001; Hu et al. 2007; Churnside 2008). Nonetheless, the response of δ to changes in the material and optical properties of particles provides some insight into the processes controlling its behavior.

The relationship between δ , b_b'/b_b , and ℓ_b shows a clear dependence of δ on both the polarized scattering properties of coccolithophores/coccoliths and the relative contribution of

multiple scattering to the return signal. If patterns in δ were driven solely by the geometric effect of multiple scattering, δ should have been similar in regions with comparable magnitudes of c and ω_b (Kouzoubov et al. 1999; Churnside 2008). However, this was not the case. Measurements of δ within the Georges Bank coccolithophore feature were almost double those measured in the shelf region where b_b' was a much smaller component of b_b . The behavior of δ in the region where changes in b became uncoupled from changes in b_b' is further evidence for the distinct influence of scattering by coccolithophores/coccoliths on δ . If the behavior of δ was driven solely by changes in the contribution of multiple scattering to the return signal, δ should have responded proportionally to the large increase in b that occurred in this region (Vasilkov et al. 2001). Instead, the slope of the relationship between δ and \mathcal{L}_b was much lower in this region, and showed a strong dependence on the magnitude of b_b'/b_b across the entire field campaign. Although these results suggest that measurements of δ may provide a path for quantifying biogeochemical properties related to coccolithophores/coccoliths (e.g. [PIC], PIC:POC), the polarized scattering properties of these unique marine particles remain poorly characterized, limiting our ability to interpret the results mechanistically.

Calcite, the mineral that composes coccoliths, is strongly birefringent, owing to the anisotropic arrangement of molecules in its crystalline structure (Bragg 1924). This property leads to a strong depolarization of incident linearly polarized light, an effect which has been exploited with great success for discriminating between calcified and non-calcified particles in applications of polarized light microscopy and flow cytometry (Olson et al. 1989; Balch et al. 1999; Guay and Bishop 2002; Beaufort 2005; von Dassow et al. 2012). Unfortunately, these investigations have been mostly empirical in nature, providing no path forward for quantifying the influence of scattering by birefringent particles on the propagation of polarized light in the ocean (Olson et al.

1989; Balch et al. 1999; Guay and Bishop 2002; Beaufort 2005; von Dassow et al. 2012). Polarized light scattering calculations performed for the coccolithophore *Emiliana huxleyi* and its detached coccoliths predict a wide range of single scattering values for δ (0.03 - 0.36), with a strong dependence on the size and morphology of the particle model used in the calculation (Zhai et al. 2013; Bi and Yang 2015). However, the birefringent nature of calcite was left unaccounted for in these studies, owing at least in part to the difficulty of including birefringence in exact calculations of light scattering (Zhai et al. 2013; Bi and Yang 2015). While our measurements of δ , which undoubtedly contain some influence of multiple scattering, are not directly comparable to values predicted from calculations of polarized light scattering, the highest values of δ measured here are at the upper limit of the range presented in the aforementioned studies, despite the fact that scattering by PIC contributed to at most 52% of our measurements of b_b . Scattering calculations performed for birefringent atmospheric particles, such as ice crystals and calcareous dust, suggest that excluding the influence of birefringence can lead to large differences in the polarization sensitive elements of the Mueller matrix (Takano and Liou 1989; Sassen 2005; Nousiainen et al. 2009; Dabrowska et al. 2013; Nousiainen and Kandler 2015). It would not be unreasonable to suggest that the omission of birefringence effects from models of light scattering by coccolithophores would lead to similar errors when interpreting measurements of δ from waters enriched in these distinct marine particles, but barring a few preliminary studies, this area of research remains unexplored.

Direct measurements of the 4x4 Mueller matrix have been made for sea water and a select few phytoplankton cultures, however they generally do not extend beyond a scattering angle of 160° in the backwards direction, and 15° in the forward direction (Voss and Fry 1984; Fry and Voss 1985; Quinby-Hunt et al. 1989; Lofflus et al. 1992; Svensen et al. 2011; Chami et al. 2014).

This limits their utility for interpreting polarized lidar measurements, as photons which are scattered at oblique angles are strongly attenuated from the lidar return. In general, the Mueller matrix for seawater displays the symmetries that one would expect from a medium consisting of randomly distributed, axially symmetric, non-spherical particles (van de Hulst 1957; Voss and Fry 1984). The \mathbf{M}_{22} matrix element deviates from unity at larger angles, leading to non-zero values of depolarization upon scattering. Measurements of the normalized \mathbf{M}_{22} matrix element from a variety of morphologically distinct phytoplankton cultures suggest that \mathbf{M}_{22} is fairly invariable and well represented by the average \mathbf{M}_{22} value for seawater, at least for the few measurements that have been made (Voss and Fry 1984; Fry and Voss 1985; Quinby-Hunt et al. 1989; Svensen et al. 2011). Interestingly, the zero-order term of the regression model presented here predicts a value of δ for non-calcified particles of $0.13 \pm 6.0\text{E-}3$ which is consistent with the value of δ predicted by extrapolating the Voss and Fry seawater \mathbf{M}_{22} element to a scattering angle of π radians ($\delta = 0.12$) (Voss and Fry 1984; Kokhanovsky 2003). Unfortunately, coccolithophores are represented by only two measurements of \mathbf{M} presented in the literature, and their calcification states at the time of measurement were either undescribed (Fry and Voss 1985), or were described as being poorly calcified (Svensen et al. 2011). As a result, the influence of birefringence on polarized light scattering by marine particles remains weakly characterized in both the theoretical and experimental literature.

The functional form of the relationship between δ , b_b'/b_b , and ℓ_b points to a forward scattering mechanism to explain the enhancement in δ associated with scattering by coccolithophores/coccoliths, a mechanism which is at least qualitatively consistent with observations of polarized forward scattering by birefringent particles (Olson et al. 1989; Balch et al. 1999; Guay and Bishop 2002; Beaufort 2005; von Dassow et al. 2012). If the relationship

between δ and b_b'/b_b was driven solely by an enhanced cross-polarized fraction of backscattering from coccolithophores/coccoliths, δ should have responded strongly to changes in b_b'/b_b in regions where the return signal was dominated by single scattering (i.e. low values of ℓ_b) (Kouzoubov et al. 1999). Instead, the statistical fit to our measurements predicts a decrease in the response of δ to changes in b_b'/b_b at decreased values of ℓ_b . This behavior could be explained if forward scattering by coccolithophores/coccoliths leads to an increase in the decay of linear polarization with depth due to enhanced forward scattering depolarization. Since the detection of forward scattered light by lidar is inherently coupled to multiple scattering, this mechanism would lead to a dependence of δ on both the relative contribution of multiple scattering to the return signal as well as the relative contribution of coccolithophore/coccolith scattering to total b . This is exactly what our statistical model predicted, with an increase in the influence of b_b'/b_b on δ as values of ℓ_b increase. The validity of this forward scattering mechanism is critically dependent on whether or not a component of linear polarization is preserved during small angle forward scattering by marine particles. If multiple forward scattering leads to a total disordering of the incident polarization state, then the rate of depolarization with depth would not be influenced by the polarized forward scattering properties of the particle assemblage, and would depend only on the proportion of multiply scattered photons detected from each depth. Measurements of polarized light scattering by cloud droplets and microspheres suggest that the incident polarization state is at least partially preserved in the multiply scattered return (Carswell and Pal 1980; Raković et al. 1999). To our knowledge, however, this has never been explored for the complex particle assemblages that occur in the marine environment.

Although my data suggest that forward scattering by coccolithophores/coccoliths plays an important role in driving changes in δ , the measurements required to test this hypothesis have not

been made, preventing us from explaining the behavior of δ mechanistically. The ambiguity of the depolarization mechanism that contributed to the behavior of δ observed here has major implications for the interpretation of polarized oceanographic lidar return signals, as forward scattering and backward scattering depolarization mechanisms should have disparate sensitivities to changes in particle properties, water column IOPs, and the lidar detector geometry. For instance, many of the techniques used to separate the single and multiple scattering components of the lidar return signal assume that the rate of depolarization with depth is primarily dependent on b (Vasilkov et al. 2001; Churnside 2008; Lu et al. 2014). If scattering by coccolithophores/coccoliths leads to a substantial increase in the rate of depolarization with depth due to enhanced forward scattering depolarization, then measurements made in regions of high [PIC] would violate this assumption. If instead, patterns in δ resulted from an increase in the cross-polarized component of backscatter from coccolithophores/coccoliths, profiles of δ could provide a straightforward pathway for characterizing the fractional contribution of scattering by PIC to $\beta(\pi)$, which could then be used to estimate both [PIC] and [POC] from a single profile of δ and $\beta(\pi)$. This type of approach would be especially sensitive to accurate retrievals of $\beta(\pi)$, either by inversion (Churnside and Marchbanks 2017) or the HSRL technique (Schulien et al. 2017), as well as separation of the multiple scattering component of depolarization from the single scattering component (Churnside 2008; Liu et al. 2019b). Furthermore, the extent to which coccolithophores and detached coccoliths depolarize light is likely to depend on factors such as particle size, morphology, calcification state, and orientation (von Dassow et al. 2012). The extent to which variability in the morphological features of coccolithophores and detached coccoliths translates into variability in their polarized scattering properties is yet to be determined, presenting a promising direction for future research.

CHAPTER IV

THE INFLUENCE OF PARTICLE CONCENTRATION AND BULK CHARACTERISTICS ON POLARIZED OCEAN LIDAR MEASUREMENTS

INTRODUCTION

In addition to revealing the vertical structure of particle concentration in the upper ocean, oceanographic lidar can provide information on the bulk properties of particle assemblages by analysis of the polarization of the backscattered pulse. The typical application of this technique involves the emission of a linearly polarized pulse, and detection of the parallel and orthogonal polarization components of the backscattered return. In the single scattering domain, the linear depolarization ratio (δ), (i.e., the ratio of the cross- to co-polarized returns) can be defined in terms of the reduced scattering matrix [$\mathbf{M}(\theta = \pi)$]:

$$\delta = \frac{1 - \mathbf{M}_{22}(\pi)}{1 + \mathbf{M}_{22}(\pi)} \quad \text{Eq. 6}$$

where π is the scattering angle sampled by lidar in radians (van de Hulst 1957). $\mathbf{M}_{22}(\pi)$ is an inherent optical property (IOP) that describes the change in the degree of linear polarization after a scattering event, and exhibits dependencies on the shape, size, and composition of the particle population. It can be estimated from δ in the single scattering domain by rearranging Eq. 6:

$$\mathbf{M}_{22}(\pi) = \frac{1 - \delta}{1 + \delta} \quad \text{Eq. 7}$$

Relationships established between $\mathbf{M}_{22}(\pi)$ and intensive particle properties (e.g. size, shape, and composition) thus provide a framework for retrieving bulk particle properties from lidar measurements of δ that are relevant to their functional role in biogeochemical ocean processes. Beyond the single scattering domain, multiple scattering leads to an increase in δ with distance at

a rate that depends on the magnitude of the scattering coefficient (b), the shape of $\mathbf{M}_{22}(\theta)$ at near-forward scattering angles, and the geometry of the lidar system [field of view (FOV), working distance, and spot size] (Zege and Chaikovskaya 1999; Vasilkov et al. 2001). Thus, multiple scattering gives δ additional sensitivities to the intensive and extensive properties of the particle assemblage that must be accounted for when using δ to estimate bulk particle properties. This represents an important distinction between $\mathbf{M}_{22}(\pi)$ (an IOP that is uninfluenced by multiple scattering and instrument geometry) and δ (a lidar-measured parameter that is sensitive to $\mathbf{M}_{22}(\pi)$, multiple scattering, and instrument geometry).

Churnside (2008) was the first to suggest that the polarization lidar technique could be used analogously to derive the intensive properties of aquatic particles after showing that lidar measurements of δ exhibited patterns that were spatially consistent with expected shifts in particle composition and morphology between coastal and offshore waters. Subsequent studies used lidar measurements of δ with *in situ* and remote estimates of bulk particle properties to develop empirical relationships between δ and the shape, size, and composition of marine particle assemblages (Collister et al. 2018; Collister et al. 2020; Dionisi et al. 2020; Schulien et al. 2020). These studies provide additional evidence that particle intensive properties could be retrieved from lidar estimates of $\mathbf{M}_{22}(\pi)$, but the empirical relationships developed therein offer limited insight into the sensitivities of $\mathbf{M}_{22}(\pi)$ to particle shape, size, and composition. For instance, variability in $\mathbf{M}_{22}(\pi)$ was not dominated consistently by any single particle property across multiple investigations, with some suggesting that $\mathbf{M}_{22}(\pi)$ is primarily an indicator of particle composition (Collister et al. 2018; Collister et al. 2020; Dionisi et al. 2020) and others suggesting that it is more sensitive to particle shape and size (Schulien et al. 2020). Particles that contribute to light scattering in natural waters are composed of a diversity of organic and inorganic matrices with a large degree

of structural and morphological complexity, challenging our ability to explore the response of $M_{22}(\pi)$ to particle shape, size, and composition *in silico* using models of polarized light scattering. Calculations that resolve this complexity have only recently been developed for a select few marine particles [e.g. coccoliths (Zhai et al. 2013; Bi and Yang 2015), colony-forming *Microcystis* sp. (Zhai et al. 2020), and chain forming diatoms (Sun et al. 2016)], but the simplifying assumptions required to make them tractable have yet to be validated against light scattering measurements at angles relevant to the lidar sampling geometry, in part due to the difficulty of measuring polarized light scattering in the near-forward and exact-backscattering directions.

Additionally, oceanographic lidar studies have struggled to account for the influence of multiple scattering on profiles of δ (Collister et al. 2018; Schulien et al. 2020). If left unaccounted for, the nonlinear concentration dependence imparted on δ by multiple scattering can result in inconsistent relationships developed between δ and the bulk properties of the particle assemblage, especially in regions of the ocean where particle concentration and bulk characteristics covary. Several Monte Carlo radiative transfer models have been developed for the purpose of exploring this effect in atmospheric and oceanographic lidar measurements (Platt 1981; Poole et al. 1981; Liu et al. 2019b), but optical closure studies required to investigate the influence of water column IOP and system geometry on profiles of δ have been difficult to perform given challenges associated with measuring profiles of δ from airborne lidar systems and in-water IOPs at similar time and space scales. Shipboard lidar systems have recently permitted some of the first studies of this kind (Liu et al. 2019b), but the Monte Carlo technique used for this purpose is computationally expensive and is of limited utility for exploring single and multiple scattering effects on δ across large parameter spaces.

This study addresses these knowledge gaps by using a combination of laboratory, field, and modeling experiments to explore the contribution of multiple scattering and changes in the bulk marine particles to measurements of δ made using a shipboard oceanographic lidar system. Linear depolarization measurements performed in the laboratory for several distinct particle assemblages allowed me to explore the influence of shape, size, and composition on values of $\mathbf{M}_{22}(\pi)$. A simple bio-optical model based on the small-angle solution to the vector lidar radiative transfer equation (Zege and Chaikovskaya 1999; Vasilkov et al. 2001) and parameterized with *in situ* measurements of water column IOPs then allowed me to explore the influence of particle concentration and composition on measurements of δ using a model sensitivity experiment.

METHODS

Scattering Measurements

To explore the sensitivity of $\mathbf{M}_{22}(\pi)$ to the intensive properties of marine particles, I measured the linear depolarization ratio for several morphologically and compositionally distinct marine particles. Three phytoplankton cultures were grown for this purpose: a marine cyanobacterium *Synechococcus* sp. (CCFWC 502; Florida Wildlife Research Institute), a marine centric diatom *Thalassiosira weissflogii* (inoculum obtained from Dr. Alexander Bochdansky; Old Dominion University), and a calcifying strain of the coccolithophore *Emiliana huxleyi* (CCMP371; National Center for Marine Algae and Microbiota). All cultures were incubated at 22°C with a 13:11 hour light:dark cycle and 60 $\mu\text{mol photons m}^{-2} \text{ s}^{-1}$ incident irradiance provided by two 40 W fluorescent-gas bulbs. *Synechococcus* sp. and *T. weissflogii* were grown in L1 medium, and *E. huxleyi* was grown in L1-Si/25 medium to promote coccolith production (Guillard

and Hargraves 1993). Cells were grown in batch-cultures and harvested for measurement toward the end of the exponential phase.

In addition to the three phytoplankton cultures, two particle suspensions were prepared that served as analogs for mineral phytoplankton tests. An analog for diatom frustules was prepared using food-grade diatomaceous earth that consisted of intact centric diatom frustules and fragmented diatom debris (P.F. Harris Mfg.; SKU: DE-FG8). A coccolith analog was prepared from reagent-grade powdered calcite (J.T. Baker). The calcite powder was ground using a mortar and pestle and sifted through a 30 μm sieve prior to being suspended in calcium-saturated ultrapure water (Barnstead Nanopure®; 18 M Ω). The particle size distribution (PSD) of the stock calcite suspension was further reduced to a median particle diameter of 1.9 μm by allowing the suspension to settle for ~15 minutes in a 500 mL graduated cylinder and retrieving the supernatant (upper 400 mL of the suspension) with a large volume pipette.

The beam attenuation coefficient for each stock particle suspension (c_{pg}) was measured at 532 nm using a Shimadzu 2700i spectrophotometer with a 1 cm cuvette. Particle concentrations were determined for each suspension using a Neubauer counting chamber, and calcified cells and detached coccoliths in the *E. huxleyi* culture were identified using cross-polarized light microscopy (Olympus BH2 microscope; linear polarizers installed after the illuminator and the objective). Particle sizes were determined manually from microscope images of each particle suspension by measuring along the major and minor axes of an aliquot of particles. An equivalent spherical diameter (ESD) corresponding to the average projected area of each particle was determined by applying a particle shape model and using Cauchy's theorem that relates the surface area (A_s) of a three-dimensional convex shape to its average projected area (A_p) in two dimensions ($A_p = 0.25 A_s$). A cylindrical particle model was assumed for *Synechococcus* sp., *T. weissflogii*, and detached

coccoliths, and a spherical model was assumed for whole *E. huxleyi* cells and laboratory calcite. For the *E. huxleyi* coccoliths, a value of 0.07 μm was used for the height dimension of the cylindrical model as this dimension was too small to measure for coccoliths using visible light microscopy (Linge Johnsen et al. 2019).

Scattering Measurement Procedures

Linear depolarization measurements were made at a scattering angle of 178.5° using a modular benchtop laboratory optical assembly (Figure 18). The light source consisted of a 532 nm collimated diode-pumped solid state laser module (LM; Thorlabs CPS532; 4.5 mW; 3.55 mm diameter; < 0.5 mrad divergence) aligned such that the major polarization axis was parallel to the benchtop reference plane. A fraction of the beam was diverted by a beam sampler, positioned directly after the laser, to a power meter (Thorlabs S130C) that served as a reference detector. A linear polarizer (170:1 extinction ratio) positioned after the beam sampler was used to clean up the source polarization, and a pair of steering mirrors oriented the beam orthogonal to the face of a glass aquarium (76 cm x 30 cm x 30 cm) positioned 1 m from the detection optics that served as a sample cuvette. A beam dump was positioned in the water at the rear of the aquarium to eliminate specular reflection of the beam from the back wall of the glass aquarium.

The receiver assembly consisted of a collecting lens (Thorlabs LA1608; $f=75.0$ mm), a 0.5 mm aperture positioned at the focal point of the lens, a 532 nm bandpass filter (Semrock LL01-532-12.5) to reject ambient light, and a photomultiplier tube (PMT; Hamamatsu H10721-20). The full-angle receiver field of view (FOV) was constrained by the collection optics to be 7 mrad. A linear polarizer (170:1 extinction ratio) fixed to an indexed rotation mount was positioned in front of the detector assembly to serve as a polarization analyzer. A multi-channel power supply

(Keithley 2231A-30-3) provided 5 V to the PMT module and 0.9 V to the PMT gain control. The PMT output was connected to an oscilloscope (Tektronix TDS2024C) with a 50 Ω termination. Signals were recorded and averaged over 200 ms for each measurement.

Vertical alignment of the detector to the scattering volume was achieved by temporarily placing a diffuse white target in the beam path at the center of the tank (38 cm from the front face) and adjusting the height of the detector assembly to maximize the signal recorded by the PMT. The detector assembly was then set to view at an in-air angle of 178° (178.5° in-water) from the source beam using an alignment jig. The detector was then aligned horizontally by translating the detector assembly along a rail mounted behind the mirror assembly until the detector viewed the laser spot projected on the alignment target and the signal recorded by the PMT was maximized. Correct alignment was confirmed by viewing the image of the alignment spot projected by the collection lens onto the receiver aperture.

Depolarization measurements were made after serial additions of scattering material to the aquarium filled with a background of filtered water. For the laboratory calcite measurements, the background consisted of ultrapure water (Barnstead Nanopure®; 18 M Ω) amended with calcium chloride (10 mM) and sodium bicarbonate (2 mM), and buffered with sodium hydroxide to a pH of 8.2. For all measurements involving live phytoplankton and the diatomaceous earth, artificial seawater (Instant Ocean®; salinity = 32) filtered through a 0.2 μm cartridge filter (Pall AcroPak 500) was used in place of pure water to prevent osmotic cell lysis.

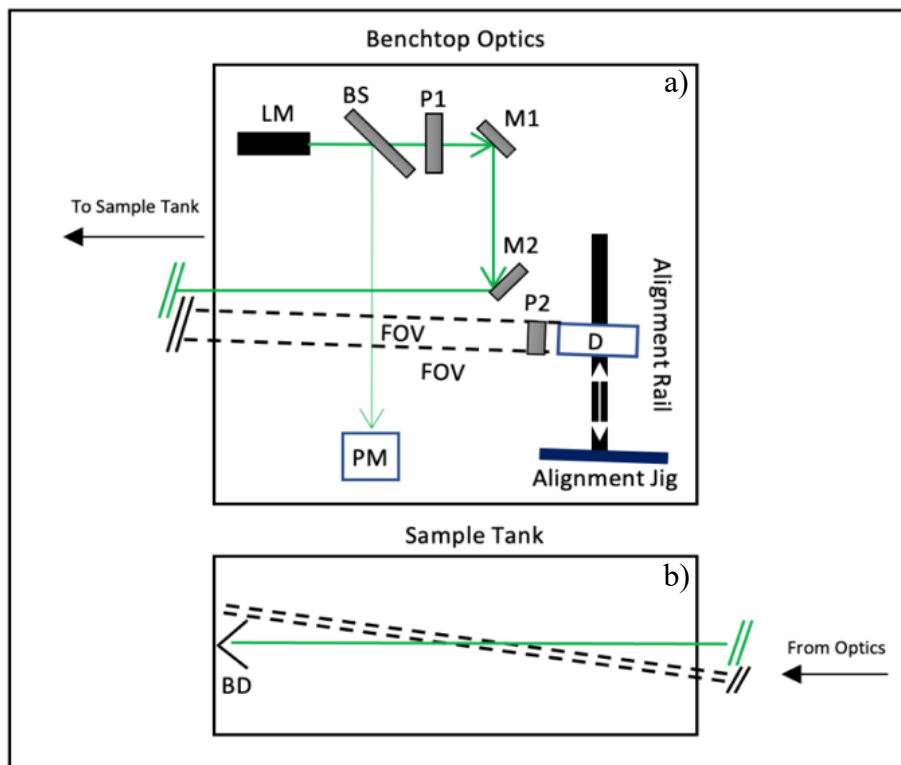


Figure 18. Plan view schematic showing the benchtop optical configuration for the depolarization measurement. a) Source optics consisted of a 532 nm laser module (LM), beamsplitter (BS), linear polarizer (P1), and two beam-steering mirrors (M1 and M2). The detector module (D) consisted of a collecting lens, 0.8 μm aperture, and a photomultiplier tube mounted to an optical rail, allowing it to be translated (white arrows) between an alignment jig (blue bar) and the measurement position. A second linear polarizer (P2) was positioned in front of the detector module to serve as a polarization analyzer. A reference detector (PM) sampled the split beam to measure temporal variations in beam energy. The beam path is shown in green and the FOV is shown by dashed black lines. b) The beam and FOV overlapped in the center of the sample tank, which was positioned down-range from the optical bench. The beam was terminated by a beam dump (BD) positioned at the rear of the tank to prevent specular reflection off the back wall of the aquarium. Drawings are not to scale; angles are exaggerated for illustration purposes.

The co- and cross-polarized returns were measured for the background water ($S_{\parallel}^{\text{blank}}$ and S_{\perp}^{blank}) and each sample addition ($S_{\parallel}^{\text{sample}}$ and $S_{\perp}^{\text{sample}}$) by rotating the linear polarizer (P2) placed in front of the detector between the co- and cross-polarized orientations. PMT dark counts were measured by obscuring the collection optics and subtracted from each measurement of S_{\parallel} and S_{\perp} . The particulate depolarization ratio (δ_p) was then calculated as:

$$\delta_p = \frac{S_{\perp}^{\text{sample}} - S_{\perp}^{\text{blank}}}{S_{\parallel}^{\text{sample}} - S_{\parallel}^{\text{blank}}} \quad \text{Eq. 8}$$

To ensure that measurements were made within the single scattering domain, δ_p was calculated only for regions of the serial addition where δ_p was independent of particle concentration and where the optical depth traveled by the measured beam was less than 1 (i.e., $c < 0.74 \text{ m}^{-1}$). δ_p was averaged over the single scattering domain for each measurement, and particulate $\mathbf{M}_{22}(178.5^\circ)$ was estimated from δ_p using Eq. 7. Since my measurements were not in the exact backscattering direction, our calculations of $\mathbf{M}_{22}(178.5^\circ)$ assume that the off-diagonal Mueller matrix elements had a negligible influence on δ_p at scattering angles very close to 180° . Previous light scattering studies suggest that this is a reasonable assumption, with $\mathbf{M}_{12}(\theta)$ for a variety of marine and atmospheric particles approaching zero as scattering angles increased toward the measurement angle of 178.5° (Voss and Fry 1984; Quinby-Hunt et al. 1989; Svensen et al. 2011; Järvinen et al. 2016; Miffre et al. 2019). For comparison with lidar measurements of δ and light scattering calculations of $\mathbf{M}_{22}(\pi)$, I also assumed that there were no strong variations in $\mathbf{M}_{22}(\theta)$ at angles very close to 180° , such that our measurements at 178.5° closely approximate values in the exact backscattering direction. Several modeling studies suggest that this is a reasonable assumption within the uncertainty of my measurements, as the polydisperse nature of marine

particles acts to suppress strong oscillations in $\mathbf{M}_{22}(\theta)$ that can often occur in monodisperse particle populations (Miffre et al. 2019). For simplicity, I will refer to our measurements of $\mathbf{M}_{22}(\theta)$ at 178.5° as $\mathbf{M}_{22}(\pi)$ throughout the remainder of the manuscript.

For the *E. huxleyi* culture in logarithmic growth, $\mathbf{M}_{22}(\pi)$ was partitioned into an acid-labile component consisting of attached and detached coccoliths [$\mathbf{M}'_{22}(\pi)$] and an acid-stable component consisting of un-plated cells [$\mathbf{M}_{22}^{\text{acid}}(\pi)$]. This was accomplished at the end of the serial addition by adjusting the pH of the sample to 5.5 using glacial acetic acid to dissolve the calcite and measure the change in S and $\mathbf{M}_{22}(\pi)$. $\mathbf{M}_{22}^{\text{acid}}(\pi)$ and S_{acid} then represented the post-acidification values of $\mathbf{M}_{22}(\pi)$ and S . $\mathbf{M}'_{22}(\pi)$ was calculated by assuming a linear contribution of $\mathbf{M}'_{22}(\pi)$ and $\mathbf{M}_{22}^{\text{acid}}(\pi)$ to $\mathbf{M}_{22}(\pi)$ that was proportional to the contribution of scattering by each material to S :

$$\mathbf{M}_{22}(\pi) = \frac{\mathbf{M}'_{22}(\pi)S' + \mathbf{M}_{22}^{\text{acid}}(\pi)S_{\text{acid}}}{S} \quad \text{Eq. 9}$$

For these measurements, standard additions were continued beyond the initial acidification while maintaining a pH of 5.5 to confirm that the measurements remained within the single scattering domain.

Unexpectedly low values of $\mathbf{M}_{22}(\pi)$ measured for *T. weissflogii* prompted me to conduct particle mixing experiments at the conclusion of the *T. weissflogii* and diatomaceous earth measurements to explore why the living diatom culture was so depolarizing. *E. huxleyi* culture was added serially at the end of the *T. weissflogii* experiment, and *T. weissflogii* culture was added serially at the end of the diatomaceous earth experiment. A least-squares linear mixing model was used to estimate $\mathbf{M}_{22}(\pi)$ for the added particle suspension from the change in bulk $\mathbf{M}_{22}(\pi)$ with each mixing addition. The cultures used for the mixing experiment portions of the *T. weissflogii* and diatomaceous earth measurements were left over from the initial light scattering experiments

(i.e. they were 2-3 weeks old and in stationary or senescent phases), so values for $\mathbf{M}_{22}(\pi)$ for the mixed in particle suspensions are not necessarily representative of healthy cultures. Nonetheless, the particle mixing experiments were useful measurement validation exercises and they are presented here alongside measurements made using the healthy cultures.

Model framework

To explore the sensitivity of δ to changes in particle intensive and extensive properties, I constructed a simple model to account for the influence of single and multiple scattering by multiple particle types on lidar measurements of δ made in the field. The model was based on an analytical solution to the lidar radiative transfer equation that uses the small-angle approximation to solve for the vertical distribution of energy and the polarization characteristics of a backscattered laser pulse (Zege and Chaikovskaya 1999; Vasilkov et al. 2001). For an initially linearly polarized pulse, the depth (z) dependent solution for the degree of linear polarization (*DoLP*) takes the form:

$$DoLP(z) = \mathbf{M}_{22}(\pi)\exp(-2\phi bz) \quad \text{Eq. 10}$$

where $\mathbf{M}_{22}(\pi)$ represents the 2,2-element of the reduced scattering matrix for whole seawater and ϕ is a depolarization factor that controls the exponential decay of *DoLP* with scattering optical depth (bz) due to multiple forward scattering, that depends on the shape of $\mathbf{M}_{22}(\theta)$ in the near-forward direction and the sampling geometry of the lidar system (Vasilkov et al. 2001). In practice, ϕ is treated as a fitting parameter due to challenges associated with measuring $\mathbf{M}_{22}(\theta)$ in the near-forward direction and sensitivities of ϕ to lidar source and detector geometries that are difficult to characterize (Vasilkov et al. 2001; Chaikovskaya 2006). $\mathbf{M}_{22}(\pi)$ was deconstructed into contributions from m scattering components as:

$$\mathbf{M}_{22}(\pi) = \sum_{n=1}^m \mathbf{M}_{22}^n(\pi) \frac{\beta_n(\pi)}{\beta(\pi)} \quad \text{Eq. 11}$$

where $\mathbf{M}_{22}^n(\pi)$ is the 2,2-element of the normalized scattering matrix element for component n , $\beta_n(\pi)$ is the volume scattering by component n at π , and $\beta(\pi)$ is the volume scattering of the bulk medium at π . The forward scattering depolarization parameter was deconstructed in a similar manner as:

$$\phi = \sum_{n=1}^m \phi_n \frac{b_n}{b} \quad \text{Eq. 12}$$

where ϕ_n and b_n are the depolarization factor and scattering coefficient for component n .

Two model sensitivity experiments were conducted to explore the role of particle type and multiple scattering in measurements of δ . For the first experiment, we tested whether patterns in δ could be explained by assuming a single particle type. $\mathbf{M}_{22}(\pi)$ was parameterized as:

$$\mathbf{M}_{22}(\pi) = \frac{1}{2\pi\beta(\pi)} [\mathbf{M}_{22}^p(\pi) \frac{b_{bp}}{\chi_p(\pi)} + \mathbf{M}_{22}^w(\pi) \frac{b_{bsw}}{\chi_{sw}(\pi)}] \quad \text{Eq. 13}$$

where the $\chi(\pi)$ factors convert between total hemispherical backscatter and backscatter at π for the particulate and pure seawater components respectively, b_{bp} is the particulate backscattering coefficient, and b_{bsw} is the backscattering coefficient of pure seawater. ϕ was parameterized for these components using Eq. 12:

$$\phi = \phi_p \frac{b_p}{b} + \phi_{sw} \frac{b_{sw}}{b} \quad \text{Eq. 14}$$

where b_p and b_{sw} are the particulate and seawater components of the scattering coefficient. For the second experiment, I explored the influence of scattering by coccoliths on $\mathbf{M}_{22}(\pi)$ by assuming three distinct scattering populations, acid-labile particles [$\mathbf{M}'_{22}(\pi)$], acid-stable particles [$\mathbf{M}_{22}^{\text{acid}}(\pi)$], and pure seawater [$\mathbf{M}_{22}^{\text{sw}}(\pi)$]. Substituting these terms into Eq.11 gives:

$$\mathbf{M}_{22}(\pi) = \frac{1}{2\pi\beta(\pi)} [\mathbf{M}'_{22}(\pi) \frac{b'_b}{\chi'(\pi)} + \mathbf{M}_{22}^{\text{acid}}(\pi) \frac{b_{\text{bp}} - b'_b}{\chi_{\text{acid}}(\pi)} + \mathbf{M}_{22}^{\text{sw}}(\pi) \frac{b_{\text{bsw}}}{\chi_{\text{sw}}(\pi)}] \quad \text{Eq. 15}$$

where the $\chi(\pi)$ factors convert between total hemispherical backscatter and π backscatter for the acid-labile, acid-stable, and pure seawater components respectively. ϕ was parameterized for these three components using Eq. 12:

$$\phi = \phi' \frac{b'}{b} + \phi_{\text{acid}} \frac{b_{\text{acid}}}{b} + \phi_{\text{sw}} \frac{b_{\text{sw}}}{b} \quad \text{Eq. 16}$$

where b' is the scattering coefficient for acid-labile particles, b_{acid} is the scattering coefficient for acid-stable particles ($b_{\text{acid}} = b_{\text{p}} - b'$), and b_{sw} is the scattering coefficient for pure seawater.

Model Parameterization

I parameterized the above model using a dataset of *in situ* IOPs that were collected concurrently with oceanographic lidar measurements of δ during the CoccoMix research expedition in the North Atlantic aboard R/V *Endeavor* cruise #616 [see Collister et al. (2020) for more details of the cruise]. For the duration of the expedition, δ was measured at a distance along the beam of 6.5 m from the sea surface using a shipboard lidar system designed to sample at spatial and temporal scales similar to traditional in-water oceanographic measurement techniques. An underway flow-through system was used to sample water continuously from the ship's seawater intake, and a WetLABS *ac-9* spectrophotometer was plumbed into the system to measure the particulate absorption and attenuation coefficients (a_{p} and c_{p}) at the surface throughout the expedition. The particulate scattering coefficient (b_{p}) was calculated as $b_{\text{p}} = c_{\text{p}} - a_{\text{p}}$, and the total scattering coefficient (b) was calculated as $b = b_{\text{p}} + b_{\text{sw}}$, where b_{sw} is the scattering coefficient for pure seawater calculated from surface measurements of temperature and salinity (Zhang et al. 2009). The particulate backscattering coefficient (b_{bp}) was measured using a Wyatt EOS light

scattering detector, and the acid-labile backscattering coefficient (b_b') was measured as the difference between total b_{bp} and measurements of backscattering from a sample that was acidified to dissolve all particulate calcite. The total backscattering coefficient was calculated as $b_b = b_{bp} + b_{bsw}$, where b_{bsw} was also calculated from surface measurements of temperature and salinity (Zhang et al. 2009).

Values used to parameterize the lidar depolarization model are summarized in Table 6. Backscattering coefficients in Eq. 13 and Eq. 15, and scattering coefficients in Eq. 14 and Eq. 16, were parameterized for each component using the *in situ* measurements described above. Since measurements of b' were not available, b' was parameterized from measurements of b_b' by assuming a constant backscattering ratio of 0.025 for coccoliths (Voss et al. 1998). I assumed a value of 0.5 for $\chi_p(\pi)$, $\chi'(\pi)$, and $\chi_{acid}(\pi)$, and a value of 0.68 for $\chi_{sw}(\pi)$ (Zhang et al. 2009; Schulien et al. 2017). $\mathbf{M}_{22}^w(\pi)$ and ϕ_{sw} were set to 1 and 0 respectively, as molecular scattering by water does not result in linear depolarization (Zhang et al. 2009). In the first experiment, two free-parameters remained, $\mathbf{M}_{22}^p(\pi)$ and ϕ_p . The model was solved for values of $\mathbf{M}_{22}^p(\pi)$ that ranged from 0.5 to 1 and values of ϕ_p that ranged from 0 to 0.4. For the second experiment, $\mathbf{M}_{22}'(\pi)$ was parameterized from laboratory measurements of depolarization by the acid labile fraction of the *E. huxleyi* culture (0.78; cf. Figure 22), leaving three free parameters in the model: $\mathbf{M}_{22}^{acid}(\pi)$, ϕ' , and ϕ_{acid} . A model sensitivity analysis was performed by solving for $DoLP$ using values of $\mathbf{M}_{22}^{acid}(\pi)$ ranging from 0.5 to 1, and values of ϕ_{acid} and ϕ' ranging from 0 to 0.4. Model predictions of δ for each combination of $\mathbf{M}_{22}'(\pi)$, ϕ_{acid} , and ϕ' were compared with field measurements of δ using r^2 and root-mean square error (RMSE).

Table 6. Model parameterizations

Single-Particle Experiment			
Parameter	Values	Units	Source
$\mathbf{M}_{22}^{\text{sw}}(\pi)$	1	dimensionless	Zhang et al. (2009)
$\mathbf{M}_{22}^{\text{p}}(\pi)$	0.5 - 1	dimensionless	free parameter
ϕ_{sw}	0	dimensionless	Zhang et al. (2009)
ϕ_{p}	0	dimensionless	free parameter
χ_{sw}	0.68	sr	Zhang et al. (2009)
χ_{p}	0.5	sr	Schulien et al. (2017)
Two-Particle Experiment			
Parameter	Values	Units	
$\mathbf{M}_{22}^{\text{sw}}(\pi)$	1	dimensionless	Zhang et al. (2009)
$\mathbf{M}_{22}'(\pi)$	0.78	dimensionless	Figure 22
$\mathbf{M}_{22}^{\text{acid}}(\pi)$	0.5-1	dimensionless	free parameter
ϕ_{sw}	0	dimensionless	Zhang et al. (2009)
ϕ'	0-0.4	dimensionless	free parameter
ϕ_{acid}	0-0.4	dimensionless	free parameter
χ_{sw}	0.68	sr	Zhang et al. (2009)
$\chi_{\text{p}} = \chi' = \chi_{\text{acid}}$	0.5	sr	Schulien et al. (2017)
b_{b}'/b'	0.025	dimensionless	Voss et al. (1998)

RESULTS

Particle Characteristics

Synechococcus sp. cells were cylindrical in shape with a median aspect ratio of 3.6, a median ESD of 2.3 μm , and a standard deviation of 0.38 μm (Figure 19 and Figure 20; Table 7). *T. weissflogii* cells were cylindrical in shape with a median aspect ratio of 2.0, and were the largest particles measured here with a median ESD of 16.2 μm and a standard deviation of 2.2 μm (Figure 19 and Figure 20; Table 7). The *E. huxleyi* culture was composed of detached coccoliths and

calcified spherical cells with a free-coccolith to calcified cell ratio of 13:1 (Figure 19). All cells had intact coccospheres at pH 8.2, and acidification of the culture to pH 5.5 resulted in complete dissolution of suspended and attached coccoliths that was confirmed by cross-polarized microscopy. The size distribution of calcified *E. huxleyi* cells was approximately normal with a median ESD of 6.6 μm and a standard deviation of 0.88 μm (Figure 20; Table 7). Detached coccoliths were the smallest particles measured here with a median ESD of 1.5 μm and a standard deviation of 0.24 μm . The PSD of the diatomaceous earth suspension was right skewed with a median ESD of 4.6 μm and individual particle sizes that ranged between 2 and 25 μm (Figure 20, Table 7). The PSD of the laboratory calcite suspension was also right skewed, with a median ESD of 1.9 μm and individual particle sizes that ranged between 1 to 13 μm (Figure 20; Table 7).

Table 7. Morphological and optical characteristics of particle suspensions used in light scattering experiment

Particle	Shape Model:	Median ESD (μm)	Median Aspect Ratio	Undiluted Stock Concentration (particles ml^{-1})	δ_p $\pm 95\% \text{ CI}$	M_{22} $\pm 95\% \text{ CI}$
<i>Synechococcus</i> sp.	cylinder	2.3	3.6	1.7×10^9	0.026 (0.003)	0.95 (0.005)
<i>Thalassiosira weissflogii</i>	cylinder	16.2	2.0	3.2×10^6	0.16 (0.003)	0.73 (0.005)
<i>Emiliania huxleyi</i> naked cells	sphere	-	1	9.7×10^5	0.034 (0.005)	0.93 (0.008)
cells + coccospheres	sphere	6.6	1	9.7×10^5	0.087 (0.001)	0.84 (0.002)
coccoliths	cylinder	1.5	-	1.3×10^7	0.12 (0.001)	0.78 (0.002)
diatomaceous earth	cylinder	4.6	1.5	7.4×10^7	0.053 (0.004)	0.90 (0.006)
laboratory calcite	sphere	1.9	1	3.6×10^7	0.25 (0.006)	0.60 (0.008)

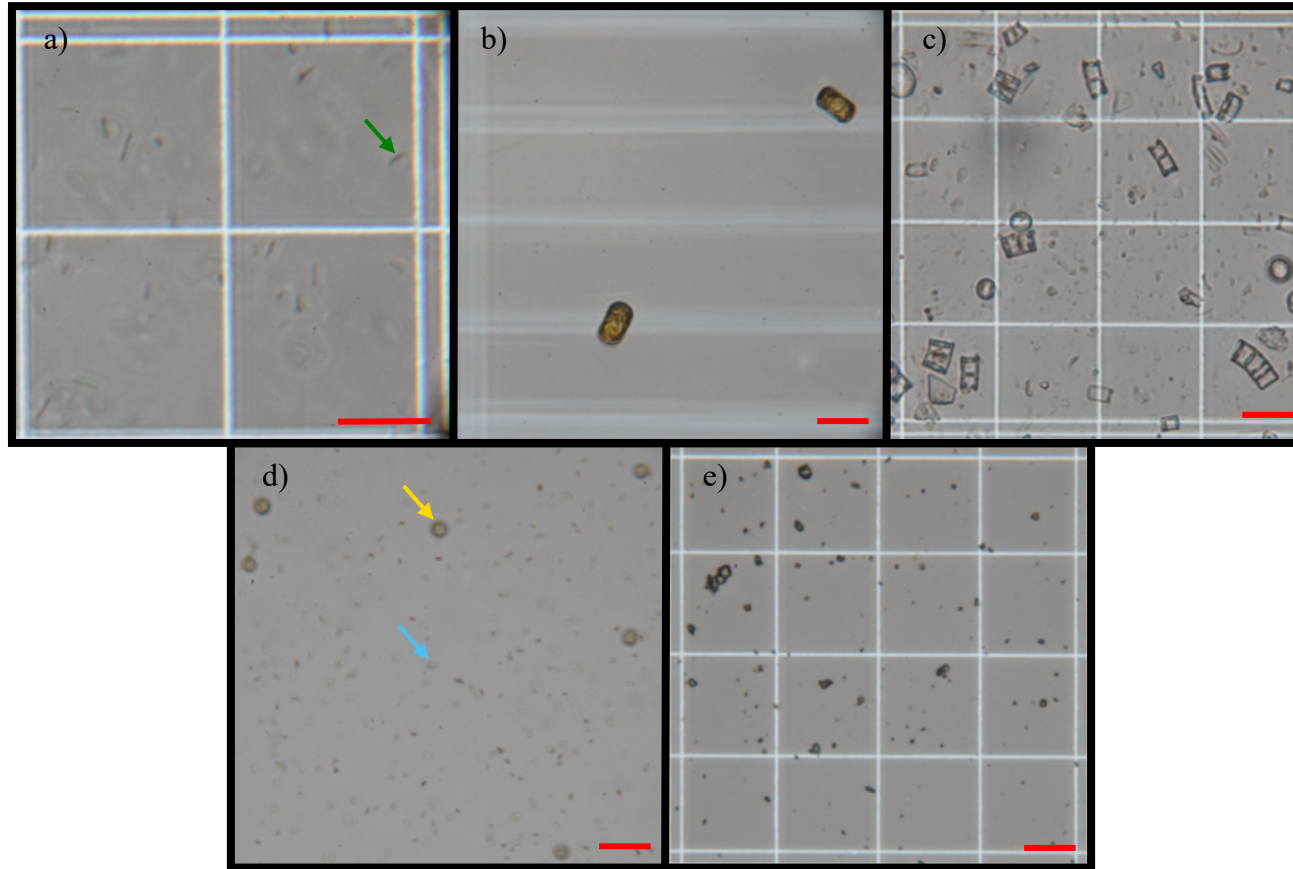


Figure 19. Microscope images of particle suspensions used in light scattering experiment. a) *Synechococcus* sp., b) *Thalassiosira weissflogii*, c) diatomaceous earth, d) *Emiliana huxleyi* with attached and detached coccoliths, and e) laboratory calcite. Arrows are used to highlight examples of a rod-shaped *Synechococcus* sp. cell (white), a calcified *E. huxleyi* cell (yellow), and a free suspended coccolith (blue). Red scale bars are all 25 μm in length.

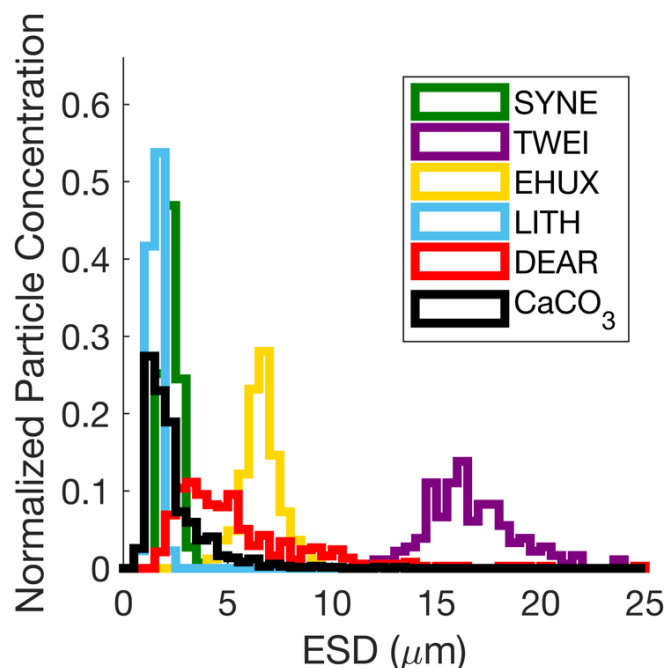


Figure 20. Histograms showing particle size distributions, expressed as equivalent spherical diameter (ESD), for each particle suspension. *Synechococcus* sp. (green; SYNE), *Thalassiosira weissflogii* (purple; TWEI), *Emiliana huxleyi* (gold; EHUX), *Emiliana huxleyi* coccoliths (cyan; LITH), diatomaceous earth (red; DEAR), and laboratory calcite (black; CaCO₃). Particle size distributions were normalized such that each histogram of ESD sums to one.

Scattering Measurements

Measurements of δ showed no linear dependence on c_{pg} , providing confidence that our measurements of δ were well within the single scattering domain (Figure 21a). δ ranged from a minimum of 0.02 for *Synechococcus* sp. to a maximum value of 0.25 for the laboratory calcite suspension. (Figure 21a). Values of δ measured for *T. weissflogii* ($\delta = 0.16$) were unexpectedly high relative to our measurements of δ for the diatomaceous earth suspension ($\delta = 0.053$) that contained diatom frustules similar in morphology to those of the living diatom, as well as the

coccolithophore culture ($\delta = 0.087$) that contained a large concentration of birefringent and high refractive index calcite coccoliths. Measurements of δ from the particle mixing experiments confirmed the elevated depolarization by *T. weissflogii* relative to *E. huxleyi* and diatomaceous earth; δ decreased asymptotically with the addition *E. huxleyi* culture to the *T. weissflogii* experiment and increased asymptotically with the addition of *T. weissflogii* culture to the diatomaceous earth experiment (Figure 21b). A least-squares linear mixing model predicted that the *E. huxleyi* and *T. weissflogii* cultures used in the mixing experiment were somewhat less depolarizing than the corresponding healthy cultures, with a value of $\delta = 0.15$ for *T. weissflogii* (compared to $\delta = 0.16$ for the healthy culture) and $\delta = 0.059$ for *E. huxleyi* (compared to $\delta = 0.087$ for the healthy culture). For the *E. huxleyi* acidification experiment, the slope of S versus the concentration of stock particle solution decreased from 3.50×10^4 to 1.33×10^4 mV L-seawater L-stock⁻¹ when the pH was lowered to 5.5, suggesting that calcite contributed to 62% of the scattered flux at π for the coccolithophore culture (Figure 21c). After the sample chamber was acidified, δ of *E. huxleyi* decreased from 0.087 to 0.034 (Figure 21d).

Small phytoplankton lacking mineral tests were the least depolarizing, with *Synechococcus* sp. having an $\mathbf{M}_{22}(\pi)$ value of 0.95 and the acidified *E. huxleyi* culture having an $\mathbf{M}_{22}(\pi)$ value of 0.93 (Figure 22; Table 7). $\mathbf{M}_{22}(\pi)$ was not a strong predictor of shape for these small, optically soft particles as both particle suspensions were weakly depolarizing despite the strong deviation of *Synechococcus* sp. cell shape from sphericity (Figure 19 and Figure 22; Table 7). $\mathbf{M}_{22}(\pi)$ for the acid labile fraction of *E. huxleyi* was 0.78, with the presence of coccoliths decreasing the value of $\mathbf{M}_{22}(\pi)$ for the bulk culture from 0.93 for decalcified cells to 0.84 for a mixture of free coccoliths and cells with intact coccospheres (below). The laboratory calcite suspension was a stronger depolarizer than coccolith calcite, with an $\mathbf{M}_{22}(\pi)$ value of 0.60 that was substantially lower than

any of the particles measured here. *T. weissflogii* was the most depolarizing of the phytoplankton species measured, with an $\mathbf{M}_{22}(\pi)$ value of 0.73. The suspension of diatomaceous earth was less depolarizing than the *T. weissflogii* culture, with an $\mathbf{M}_{22}(\pi)$ value of 0.90.

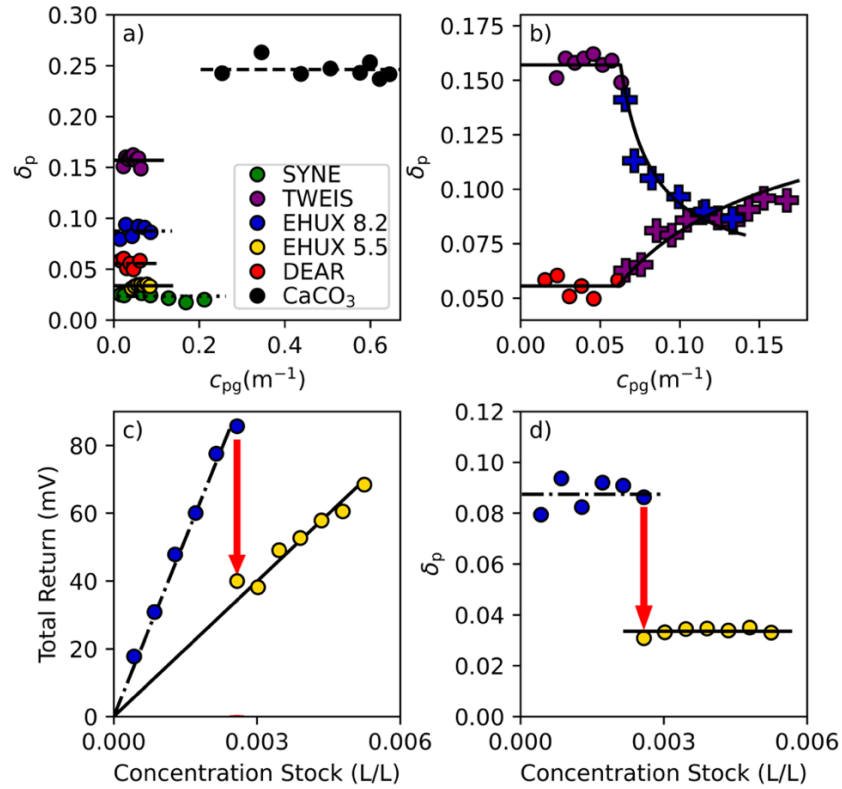


Figure 21. Laboratory depolarization experiment results. a) Plot of δ versus c_{pg} for each experiment [*Synechococcus* sp. (green; SYNE), *Thalassiosira weissflogii* (purple; TWEI), *Emiliana huxleyi* at pH 8.2 (gold; EHUX 8.2), *Emiliana huxleyi* at pH 5.5 (blue; EHUX 5.5), diatomaceous earth (red; DEAR)], and laboratory calcite (black, CaCO_3). b) Particle mixing experiments. Marker colors are consistent with the legend in a). Mixing additions are plotted as “pluses”. Black lines represent least-squares fits to a linear mixing model used to estimate the $\mathbf{M}_{22}(\pi)$ for the added particle suspension. c) S and d) δ from the *E. huxleyi* acidification experiment plotted against the concentration of stock algal culture. Red arrows highlight the change in S and δ after acidification.

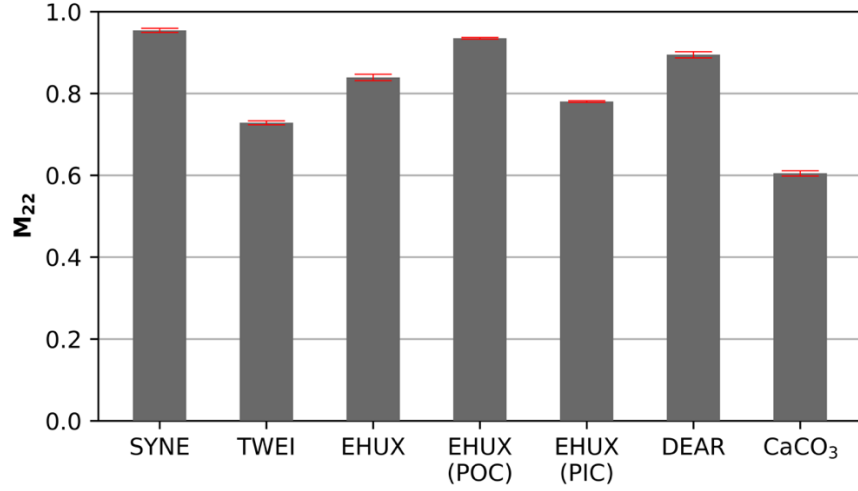


Figure 22. Bar graph showing estimates of $M_{22}(\pi)$ in the near backwards direction for *Synechococcus* sp. (SYNE), *Thalassiosira weissflogii* (TWEI), whole *Emiliana huxleyi* (EHUX), acid-stable *Emiliana huxleyi* [EHUX (POC)], acid-labile *Emiliana huxleyi* [EHUX (PIC)], laboratory calcite (CaCO₃), and diatomaceous earth (DEAR). Error bars show 95% confidence limits of the mean. For values in this figure, refer to Table 7.

Model Sensitivity Analysis

In Figure 23a, b contours of r^2 , and RMSE calculated between modeled and measured values of δ are shown as a function of $M_{22}^p(\pi)$ and ϕ_p values used for each model parameterization. Both model evaluation metrics exhibited similar patterns, with an elongation of contours in the positive $M_{22}^p(\pi)$ versus ϕ_p direction that resulted from shifts in single scattering depolarization being compensated for in the model by shifts in multiple scattering depolarization (Figure 23a, b). Optimized model solutions with respect to r^2 and RMSE reproduced many of the broad-scale patterns found in measurements of δ , with values generally tracking patterns in b across the timeseries [cf. Figure 23d with Figure 2 in Collister et al. (2020)]. However, the single-particle

model overestimated δ in the region of strong scattering near the coast where b_{bp} and b_b' became decoupled, with increasing values of $\mathbf{M}_{22}^p(\pi)$ and ϕ_p leading to an increase in this overestimation (Figure 23c, d). The RMSE optimized solution exhibited the least overestimation in this region, but these improvements were compensated for by an underestimation of δ in the region of high scattering that was dominated by suspended particulate calcite (Figure 23c, d).

The two-particle model was more sensitive to the parameterization of ϕ_{acid} than to ϕ' , and there were no model solutions that resulted in an r^2 of 0.75 or higher for values of ϕ_{acid} greater than 0.14 (Figure 24). For $\mathbf{M}_{22}^{acid}(\pi)$ and ϕ' , solutions existed for the entire range of values within the $r^2 \geq 0.75$ criterion. Increasing values of ϕ_{acid} resulted in optimum values of ϕ' and $\mathbf{M}_{22}^{acid}(\pi)$ (as determined from a maximum in r^2 or minimum in RMSE for a particular value of ϕ_{acid}) that were inversely related, where a decrease in $\mathbf{M}_{22}^{acid}(\pi)$ (i.e. an increase in the backscattering depolarization by the acid-stable particle population) was compensated for by an increase in ϕ' (i.e. increase in the forward scattering depolarization by coccolith calcite, Figure 24a, b). For values of ϕ_{acid} greater than 0.1, optimum values of $\mathbf{M}_{22}^{acid}(\pi)$ and ϕ' were constrained to their maximum and minimum values respectively, resulting in a rapid decrease in model fitness with increasing ϕ_{acid} (Figure 24a, b). For the two-particle model solutions, values of r^2 and RMSE were minimally improved relative to the single-particle model (Table 8), but the two-particle model was able to better resolve the behavior of δ within the coastal scattering region where b_{bp} and b_b' became decoupled (c.f. Figure 23c, d, Figure 24c, d, and Figure 2 in Collister et al. (2020)).

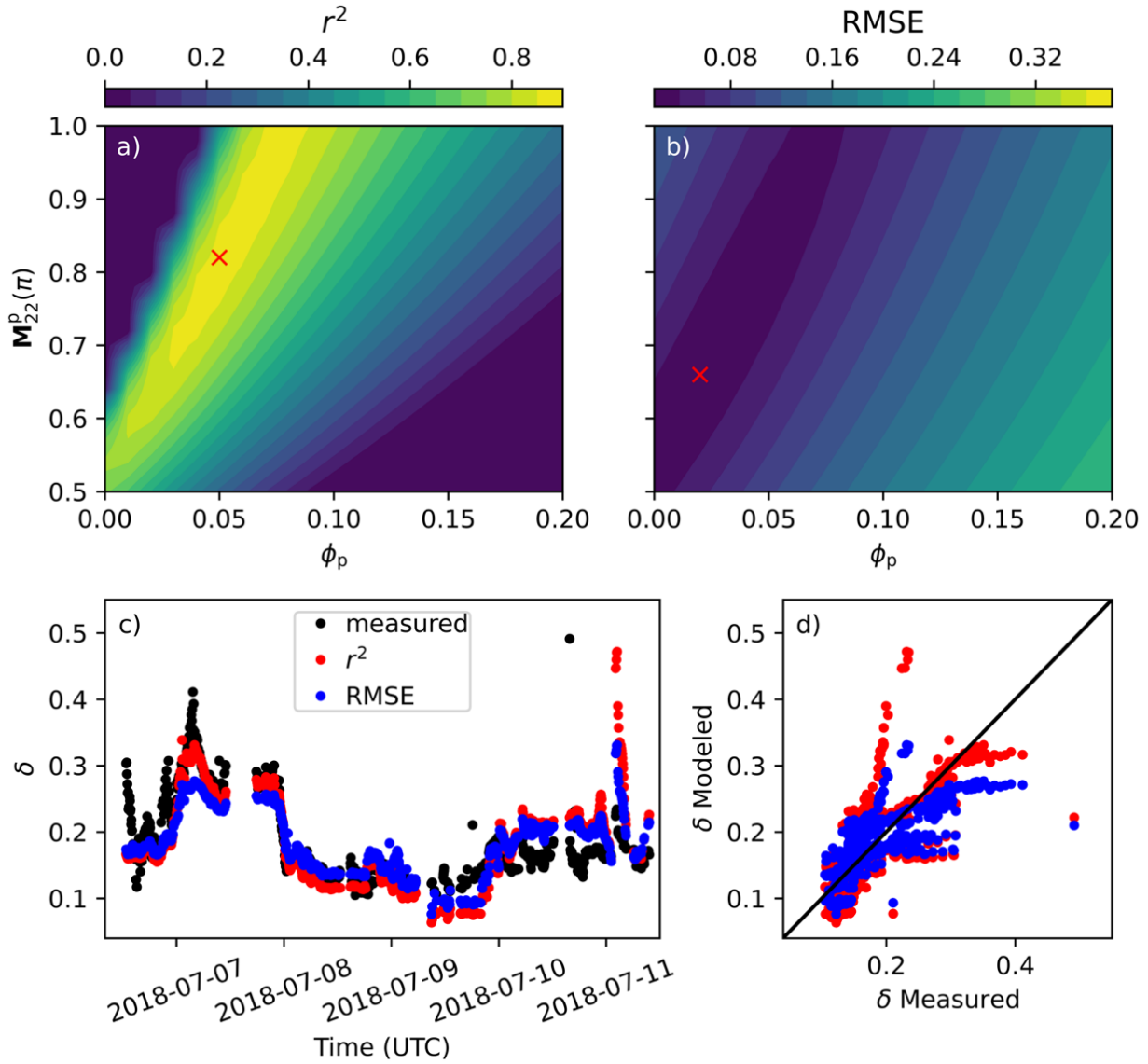


Figure 23. Plots showing results from the single-particle model sensitivity experiment. Contours of a) r^2 and b) RMSE are plotted as a function of model input parameters $\mathbf{M}_{22}^p(\pi)$ and ϕ_p . The red 'x' in each contour plot represents the optimum model solution with respect to each fit criterion. c) Model estimates of δ from the r^2 (red) and RMSE (blue) optimized solutions are plotted as timeseries alongside lidar measurements of δ from Collister et al. (2020). d) Modeled values of δ from the r^2 (red) and RMSE (blue) optimized solutions plotted as cross-plots against measured values of δ .

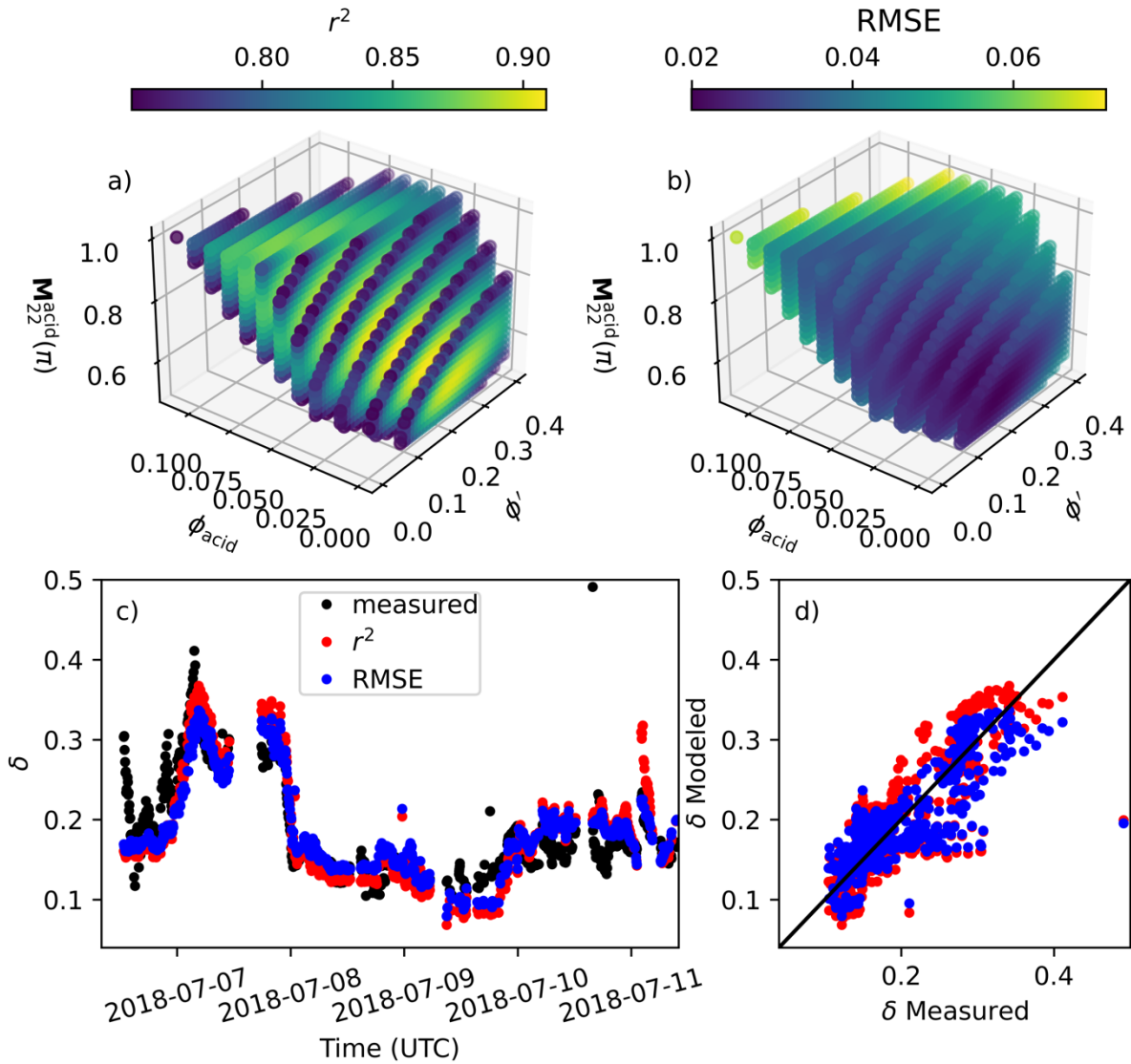


Figure 24. Plots showing results from the two-particle model sensitivity experiment. r^2 a) and RMSE b) are shown by the colormap, with the location of each point representing the model input parameters ϕ' , ϕ_{acid} , and $M_{22}^{POC}(\pi)$ used for each solution. c) Model estimates of δ from the r^2 (red) and RMSE (blue) optimized solutions are plotted as timeseries alongside lidar measurements of δ from Collister et al. (2020). d) Modeled values of δ from the r^2 (red) and RMSE (blue) optimized solutions plotted as cross-plots against measured values of δ .

Table 8. Model sensitivity experiment results

Single-Particle Experiment					
Optimization	r^2	RMSE	\mathbf{M}_{22}^p	ϕ_p	
r^2	0.88	0.028	0.82	0.05	
RMSE	0.84	0.024	0.66	0.02	
Two-Particle Experiment					
Optimization	r^2	RMSE	$\mathbf{M}_{22}^{\text{POC}}$	ϕ_{acid}	ϕ'
r^2	0.91	0.022	0.70	0.020	0.18
RMSE	0.89	0.020	0.58	0.0	0.19

Model fitness decreased with decreasing values of $\mathbf{M}'_{22}(\pi):\mathbf{M}_{22}^{\text{acid}}(\pi)$ and $\phi':\phi_{\text{acid}}$ (Figure 25). Decreases in the forward scattering depolarization by coccolith calcite relative to the acid-stable particle population were compensated for by an increase in the single scattering depolarization of calcite relative to the background (Figure 25). The two-particle model offered improved model fitness over the single particle model only within the parameter space where calcite was more depolarizing in the forward direction than the background, acid-stable particle population (i.e. $\phi':\phi_{\text{acid}} > 1$). All optimum model solutions where $\phi':\phi_{\text{acid}} < 1$ required that coccolithophore calcite was more depolarizing in the backwards direction (i.e. $\mathbf{M}'_{22}(\pi):\mathbf{M}_{22}^{\text{acid}}(\pi) < 1$) than the acid-stable particle population. Importantly, there are no optimum model solutions where the acid-stable population is a stronger depolarizer than PIC in both the forward and backwards directions.

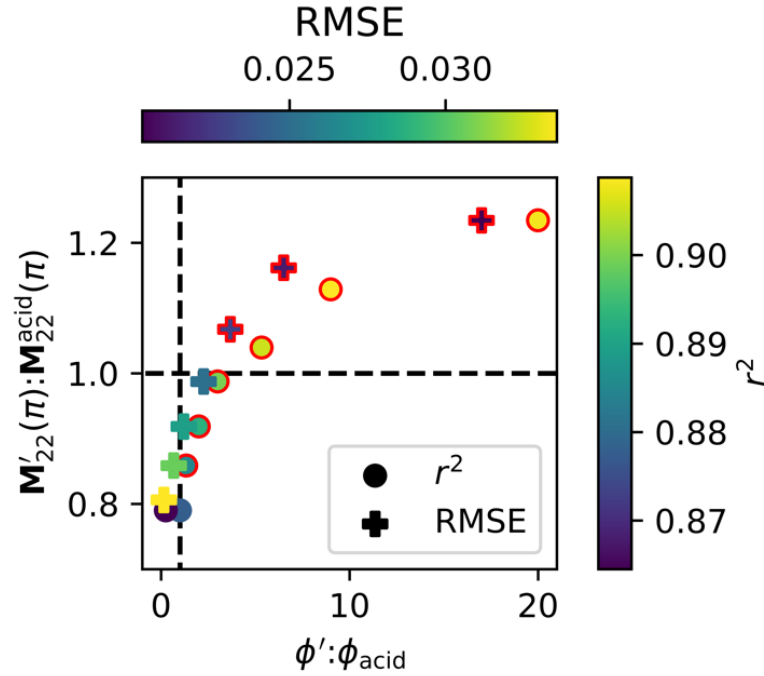


Figure 25. Plot of $\mathbf{M}'_{22}(\pi):\mathbf{M}_{22}^{acid}(\pi)$ versus $\phi':\phi_{acid}$ for non-zero values of ϕ_{acid} that resulted in a non-zero optimum value of ϕ' . Solutions for r^2 and RMSE optimizations are shown as colored spheres and crosses respectively. Colormaps show the values of r^2 and RMSE for each model solution, and symbols outlined in red denote solutions that offer improvements in adjusted- r^2 or RMSE relative to the single-particle model.

DISCUSSION

The results of our measurements and modeling analyses presented here show that ocean lidar measurements of δ exhibit complex, and sometimes counterintuitive dependencies on particle size, shape, composition, and concentration that will likely complicate efforts to use polarized oceanographic lidar as a tool for characterizing particles in the ocean. Laboratory measurements of $\mathbf{M}_{22}(\pi)$ for several morphologically and compositionally distinct marine particles exhibited a large degree of variability, bolstering the idea that spatiotemporal gradients in marine particle characteristics are detectable using polarized oceanographic lidar. However, the behavior of $\mathbf{M}_{22}(\pi)$ with respect to particle size, shape, and composition was complex, and $\mathbf{M}_{22}(\pi)$ was not a straight-forward predictor of any single particle intensive property. The interacting effects of particle shape, size, and composition on $\mathbf{M}_{22}(\pi)$ likely explain some of the disparity in the polarized oceanographic lidar literature, where variability in δ has not been consistently attributed to changes in any single particle property across multiple investigations (Churnside 2008; Collister et al. 2018; Collister et al. 2020; Dionisi et al. 2020; Schulien et al. 2020). Modeling results suggest that particle concentration can also be an important source of variability in lidar measurements of δ through the influence of multiple scattering and through shifts in the relative contribution of particulate versus molecular scattering to the lidar return signal. The influence of molecular scattering by seawater on δ can be accounted for in a straightforward manner by modeling the contribution of β_{sw} to total β , but correcting for the influence of multiple scattering on δ requires information on the depth distribution of b and the shape of the $\mathbf{M}_{22}(\theta)$ in the forward direction that cannot be independently retrieved from the lidar signal. These results have important implications for current and future lidar missions that rely on polarization information to retrieve the optical and biogeochemical properties of marine particles.

Although laboratory measurements of $\mathbf{M}_{22}(\pi)$ were not driven predominantly by any single particle intensive property, the behavior of $\mathbf{M}_{22}(\pi)$ with respect to particle shape, size, and composition agreed qualitatively with theoretical models of polarized light scattering by non-spherical particles. Small, optically-soft particles approaching the Rayleigh-Gans limit are expected to be weak depolarizers, with $\mathbf{M}_{22}(\pi)$ having a muted sensitivity to particle shape (Mishchenko et al. 2002; Mukherjee et al. 2018). This is consistent with our measurements of $\mathbf{M}_{22}(\pi)$ for small, low refractive index phytoplankton cells. *Synechococcus* sp. and decalcified *E. huxleyi* cells were weak depolarizers, and large deviations of *Synechococcus* sp. from sphericity did not result in a reduced value of $\mathbf{M}_{22}(\pi)$ relative to the spherical *E. huxleyi* cells. For a constant particle composition, non-spherical light scattering simulations predict a rapid increase in depolarization with particle size in the transition between the Rayleigh-Gans and resonant scattering domains (Mishchenko et al. 2002; Mukherjee et al. 2018). This phenomenon likely accounts for some of the differences in $\mathbf{M}_{22}(\pi)$ between the laboratory and coccolith calcite suspensions. Despite having a similar median ESD to the suspension of coccolith calcite, the laboratory calcite suspension was right-skewed, and scattering contributions from large particles could have contributed to a decrease in $\mathbf{M}_{22}(\pi)$ for the bulk suspension. As particle size increases into the resonant scattering domain, $\mathbf{M}_{22}(\pi)$ becomes less sensitive to particle size and exhibits an increased sensitivity to particle morphology and refractive index (Mishchenko et al. 2002; Mukherjee et al. 2018). Consistent with these predictions, large particles and particles containing high refractive index minerals (coccoliths, laboratory calcite, *T. weissflogii*, and diatomaceous earth) were more depolarizing than optically soft phytoplankton cells, and particle composition and morphology appeared to have played an increased role in determining $\mathbf{M}_{22}(\pi)$.

The *T. weissflogii* culture produced an unexpectedly strong depolarization response, with a value of $\mathbf{M}_{22}(\pi)$ that was substantially lower than the compositionally and morphologically similar suspension of diatomaceous earth particles. One possible explanation for this behavior of $\mathbf{M}_{22}(\pi)$ is related to differences in the size distributions of the two diatom derived suspensions. Although intact diatomaceous earth frustules were similar in shape and composition to the *T. weissflogii* frustules, small silica debris particles were a large component that reduced the median PSD of the diatomaceous earth suspension (4.6 μm) relative to the live culture (16.2 μm), potentially causing an increase in $\mathbf{M}_{22}(\pi)$ for the bulk suspension. This difference could also explain why *T. weissflogii* was a stronger depolarizer than the birefringent and highly refractive coccoliths, given that live diatom cells were larger than coccoliths by more than a factor of eight and that coccoliths were likely small enough to occupy the size sensitive domain of $\mathbf{M}_{22}(\pi)$ (Zhai et al. 2013; Bi and Yang 2015). The presence of high refractive index intracellular structures within the live diatom cells but lacking in the diatomaceous earth frustules could have also contributed to enhanced depolarization by *T. weissflogii*. Scalar light scattering experiments suggest that intracellular structures can play an important role in determining the backscattering efficiency of phytoplankton, but very little is known about the influence of refractive index inhomogeneities caused by intracellular lipid globules on the polarized light scattering properties of marine particles (Whitmire et al. 2010; Zhou et al. 2012). One of the few manipulative experiments to explore this topic (Witkowski et al. 1998) suggests that the presence of intracellular structures does not necessarily translate into enhanced depolarization in the backscattering direction for cultures of *Chlorella vulgaris*, *Chlorella kesleri*, and *Chroococcus minor*. However, it is possible that the accumulation of high refractive index intracellular lipids within diatoms during periods of nutrient stress (Jung et al. 2018; Leyland et al. 2020) could account for the anomalously high backscattering

efficiencies that have been reported for diatoms (Whitmire et al. 2010; Zhou et al. 2012), as well as the strong depolarization by *T. weissflogii* observed here. Depolarization experiments that explicitly control for particle size or the presence/absence of intracellular structures would be highly informative with respect to these hypotheses.

E. huxleyi coccoliths are among the few morphologically complex marine particles for which polarized light scattering calculations have been performed. These models predict a wide range of values for $M_{22}(\pi)$ (0.67 - 0.98) that exhibit strong sensitivities to particle size and morphology (Zhai et al. 2013; Bi and Yang 2015). Our measurement of $M_{22}(\pi)$ for the acid labile fraction of the *E. huxleyi* culture was well within the range of values predicted by the Zhai et al. (2013), but was more depolarizing than values predicted by Bi and Yang (2015), which returned a minimum value of 0.86. Given that the Bi and Yang (2015) invariant imbedding T-matrix method validated well against the DDA technique used by Zhai et al. (2013), differences between the two studies likely resulted from the use of morphologically distinct coccolith models rather than from differences in the computational techniques used to solve for the scattering matrix. Coccolith morphologies are species-specific and highly diverse (Young et al. 1999), and the sensitivity of these calculations to subtle differences in the coccolith model geometry likely translates into large interspecies variability in the relationships between $M_{22}(\pi)$, b_b'/b_b , and the concentration of particulate inorganic carbon ([PIC]) (Gordon and Du 2001). Although this sensitivity to coccolith geometry may further complicate efforts to develop polarization based lidar retrievals of [PIC], it could present an opportunity to use species specific relationships between [PIC] and δ to distinguish monospecific *E. huxleyi* blooms from those with higher coccolithophore diversity.

The interacting effects of particle shape, size, and composition on M_{22} will complicate efforts to develop techniques for retrieving particle intensive properties from oceanographic lidar

measurements of δ . For natural particle populations, the sensitivity of $\mathbf{M}_{22}(\pi)$ to several particle intensive properties is likely to result in regionally specific behaviors of $\mathbf{M}_{22}(\pi)$ that depend strongly on local modes of particle variability in size, composition, and intracellular packaging. In coastal waters where high refractive index minerals and organic detritus are important contributors to backscattering and particle composition is highly variable, $\mathbf{M}_{22}(\pi)$ may be driven predominantly by changes in bulk particle refractive index (Aas 1996; Twardowski et al. 2001). In the open ocean, where bulk refractive index is typically less dynamic, shifts in particle shape and size may be the dominant source of variability in $\mathbf{M}_{22}(\pi)$ (Aas 1996; Twardowski et al. 2001). Additionally, natural particle assemblages occupy a broader spectrum of sizes, shapes, and compositions than the laboratory generated particle assemblages measured here. The wide range of particle characteristics represented in natural particle assemblages, combined with the interacting effects of particle shape, size, and composition on $\mathbf{M}_{22}(\pi)$ can result in an ambiguous response of $\mathbf{M}_{22}(\pi)$ to changes in the bulk particle characteristics that we often aim to retrieve (e.g. average particle size, average particle aspect ratio, bulk refractive index). For instance, morphological shifts that occur at opposite ends of the particle size spectrum will have very different effects on $\mathbf{M}_{22}(\pi)$, even if they result in identical changes to the bulk shape of the particle assemblage. Particle intensive property retrievals that combine polarized oceanographic lidar and passive ocean color or polarimetry could help to constrain some of these ambiguities by providing independent estimates of particle characteristics as well as light scattering information at angles that are inaccessible to the lidar sampling geometry (Ibrahim et al. 2016). However, additional information on the behavior of $\mathbf{M}_{22}(\pi)$ with respect to changes in the bulk characteristics of natural particle populations is required before these capabilities can be explored further.

The model results presented here suggest that multiple scattering and shifts in the relative contribution of particulate versus molecular scattering can play a dominant role in controlling patterns in lidar measurements of δ from bulk seawater. This was the case for the CoccoMix expedition (Collister et al. 2020), where a single particle model for $\mathbf{M}_{22}(\pi)$ and ϕ accounted for as much as 88% of the variability in δ . These results suggest that the strong correlation between δ and b_b'/b_b within the coccolithophore bloom was driven predominantly by the covariation between calcite concentration and particulate backscatter, rather than by coccoliths having a substantially lower value of $\mathbf{M}_{22}(\pi)$ relative to the background, acid-stable particle population. This is consistent with the conclusions drawn in Collister et al. (2020), where a statistical model applied to measurements of δ showed that an increase in b_b'/b_b at small optical depths did not result in an increase in δ that would be expected if $\mathbf{M}_{22}(\pi)$ for calcite was substantially lower than the acid-stable particle population present within the coccolithophore bloom. However, despite resolving much of the variability in δ throughout the CoccoMix expedition, a single particle model of depolarization could not reproduce the behavior of δ when backscattering became uncoupled from scattering by calcite (Collister et al. 2020). The two-particle model accounted for this bifurcation with several configurations of particle depolarization characteristics, but patterns in r^2 and RMSE for these solutions point strongly to this pattern resulting from calcite being a stronger depolarizer in the forward direction than the particles that composed the acid-stable fraction of the particle assemblage. This is consistent with observations of strong forward depolarization that are commonly used to identify birefringent calcite particles in applications of polarized light microscopy and flow-cytometry (Balch et al. 1999; Guay and Bishop 2002; von Dassow et al. 2012)

Previous studies involving polarized oceanographic lidar have struggled to separate the effects of single and multiple scattering on δ . Schulien et al. (2020) used the ratio $\delta:b_{bp}$, where b_{bp} is estimated from lidar measurements of $\beta(\pi)$, to account for the influence of multiple scattering contained in δ . However, this ratio primarily reflects changes in the relative contribution of particulate scattering to the total return signal, and does account for the depth dependence of multiple scattering. Changes in this ratio are difficult to interpret, as they can occur by several mechanisms, including changes in particulate $M_{22}(\pi)$, the shape of the scattering phase function, and the depth dependence of multiple scattering. Collister et al. (2020) were able to account for the depth dependence of multiple scattering by examining patterns of δ as a function of scattering optical depth, but had to resort to an empirical statistical model to separate out contributions of scattering from different components. The model presented here provides a generic framework that can be used to account for multiple scattering and shifts in particle composition in measurements of δ , given that b can be estimated or measured directly alongside of δ . Since b cannot be directly retrieved using lidar, routine application of this technique to oceanographic lidar measurements will require either bio-optical models, *in situ* measurements, or the development of techniques for retrieving b from other sensing platforms. Another critical limitation of the model is related to the parameterization of $\chi_p(\pi)$ for the different particle populations. The lack of information on the variability of $\chi_p(\pi)$ in the surface ocean represents a fundamental knowledge gap in the oceanographic lidar field that limits our ability to constrain the uncertainties associated with modeling δ from in-water IOPs or retrieving b_{bp} from lidar profiles of $\beta(\pi)$. Future efforts to constrain the variability of $\chi_p(\pi)$ in the global ocean, such as those recently published by (Hu et al. 2020), should be included in any future efforts to develop oceanographic lidar as a tool for remote sensing of aquatic ecosystems.

Variability in $\mathbf{M}_{22}(\pi)$ associated with shifts in the intensive properties of marine particles can also have an important influence on retrievals of b_{bp} made using the cross-polarized channel of the spaceborne lidar CALIOP. For these retrievals, estimates of $\mathbf{M}_{22}(\pi)$ are required to convert between measurements of cross-polarized and particulate backscatter at π ; typically this has been achieved using an empirical relationship between $\mathbf{M}_{22}(\pi)$ and K_d to either parameterize $\mathbf{M}_{22}(\pi)$ from independent measurements of K_d (Behrenfeld et al. 2013; Behrenfeld et al. 2017; Behrenfeld et al. 2019a; Lacour et al. 2020) or to justify the elimination of the K_d and $\mathbf{M}_{22}(\pi)$ terms from the retrieval (Bisson et al. 2021). These assumptions have produced reasonable retrievals of b_{bp} thus far, but the mechanistic link between $\mathbf{M}_{22}(\pi)$ (an intensive property, i.e. a property that varies independently of particle concentration) and K_d (an extensive property; i.e. a property that depends on particle concentration) remains unclear, making it difficult to predict when and where it may break down and contribute to systematic error in CALIOP retrievals of b_{bp} . This relationship could potentially result from the broad-scale covariation between particle concentration, size, and bulk refractive index in the ocean where highly attenuating waters are typically associated with suspended mineral sediments and large, bloom-forming phytoplankton that we showed here to be more depolarizing than the small, optically-soft species that predominate in the oligotrophic ocean (Sheldon et al. 1972). Multiple scattering could have also contributed to the relationship between $\mathbf{M}_{22}(\pi)$ and K_d , since lidar measurements of δ used to derive this relationship were uncorrected for the increase in δ with increasing optical depth (Behrenfeld et al. 2013). The broad-scale agreement found between CALIOP retrievals and *in situ* measurements of b_{bp} suggests that errors associated with multiple scattering either have a negligible influence on CALIOP measurements of δ or that the influence of multiple scattering on δ is compensated for by systematic error associated with another assumption in the model, for instance the parameterization of $\chi_p(\pi)$. The laboratory

measurements and modeling results presented here cannot reject either of these mechanisms, and a better understanding of the variability in $\mathbf{M}_{22}(\pi)$ and $\chi_p(\pi)$ in the global ocean as well as the influence of multiple scattering on in-water CALIOP measurements will be required to better constrain potential sources of systematic error in CALIOP retrievals of b_{bp} .

The dependence of δ on several intensive and extensive particle properties shown here is reminiscent of the chlorophyll retrieval problem for passive ocean color, where spatial variability in the relative contributions of phytoplankton, non-algal particles, and colored dissolved organic matter to remote sensing reflectance requires that regionally specific approaches are used for retrieving chlorophyll concentration in optically complex waters (Sathyendranath et al. 1989). Typically, PIC algorithms and chlorophyll algorithms designed for optically complex waters are developed by characterizing regional modes of optical variability using measured IOP and AOP spectra and developing look-up tables or modifying algorithm coefficients such that they reproduce the characteristic optical variability of the region (Balch et al. 2005; McKee et al. 2007; Van Der Woerd and Pasterkamp 2008). A conceptually similar regional approach may be useful for retrieving particle information from lidar measurements of δ and for parameterizing δ in CALIOP retrievals of b_{bp} , but this will likely require additional information from passive sensors to supplement the low degrees-of-freedom afforded by lidar measurements at a single wavelength. Just as regional passive ocean color algorithm development has relied on field measurements of water column optical and biogeochemical properties from a diversity of water types to constrain their influence on remote sensing reflectance spectra, regional polarized lidar retrievals of particle characteristics will require in-water measurements of $\mathbf{M}_{22}(\pi)$, $\beta(\pi)$, and the particle intensive properties that contribute to their variability. Instrumentation designed with these measurements

in mind is currently unavailable to the ocean science community, representing a major hurdle for the advancement of polarized oceanographic lidar as a routine remote sensing technique.

CHAPTER V

CONCLUSIONS AND FUTURE WORK

CONCLUSIONS

The studies presented here demonstrate the unique ability for shipboard oceanographic lidar to map the horizontal and vertical distribution of optical and biogeochemical properties in the upper ocean. Lidar measurements of α and δ resolved optical and biogeochemical gradients across a wide range of water types that were spatially consistent with simultaneously measured in-water optical and biogeochemical properties. Relationships developed between lidar, and in-water measurements permitted the mapping of particle distributions and their bulk characteristics at horizontal resolutions that cannot be achieved using standard in-water shipboard profiling techniques. Measurements of chlorophyll concentration and K_d were retrieved at sub-kilometer horizontal scales that revealed fine-scale optical structures associated with coastal fronts and mesoscale circulation features. In addition to providing information on the concentration of materials in the upper water column, measurements of δ provided insight into the nature of particles that could be used to better parameterize the role of ocean particles in models of upper-ocean biogeochemistry. As highlighted by others, extension of these measurement techniques to a spaceborne lidar system will be required fill the need for repeat global measurements of the vertical distribution of ocean ecosystems. Nevertheless, shipboard lidar profiling of the upper ocean can fill several important gaps in our ability to sample the ocean by offering improvements in sampling resolution over traditional in-water, ship-based profiling that is inherently coarse across time and horizontal space and by extending measurements from surface-restricted sampling schemes (e.g. ships-of-opportunity, surface AUVs, buoys, and moorings) to depth. These capabilities will be

especially useful for investigating sub-mesoscale ecosystem dynamics, where continuous underway sampling is required to resolve localized optical structures that can evolve rapidly over time.

The ability to measure lidar and in-water optical properties simultaneously at identical spatial and temporal scales resulted in an improved understanding of the complex response of the lidar return signal to water column optical properties. The shipboard lidar scheme allowed me to validate the relationship between α and K_d proposed by others for wide field-of-view lidar systems (e.g. Gordon 1982) by using an unprecedented number of coincident remote and *in situ* observations. Consistent with theoretical studies conducted more than 3 decades prior, these experimental results suggest that the relationship between α and K_d is fairly insensitive to changes in the shape of the volume scattering function, and that retrievals of K_d from α represent a promising technique for mapping the submarine light field and the concentration of materials in the upper water column (Gordon 1982). However, the relationship between α and K_d exhibited an apparent sensitivity to changes in the single scattering albedo that could result in systematic error in lidar retrievals of K_d , especially when measured across strong optical gradients. Although this behavior was predicted theoretically by Gordon (1982), it is often neglected in lidar retrievals of K_d without characterizing its potential to contribute to retrieval error. This behavior is reasonably simple to characterize experimentally for shipboard lidar systems, but the number of matchups required to characterize this response for airborne systems is prohibitively difficult to achieve. In bridging that gap, radiative transfer models validated against shipboard lidar measurements could provide an opportunity to determine the sensitivity of airborne retrievals of K_d to changes in the single scattering albedo *in silico* without the need for a large number of experimental matchups.

The strong correlation found between the δ and b_{bp}/b_p in Chapter II supports the idea that lidar profiles of the linear depolarization ratio (δ) can provide information on the material characteristics of scattering particles. However, a lack of information on the nature of polarized light scattering by marine particles and the influence of multiple scattering on lidar measurements of δ precluded a mechanistic explanation for the relationship that could be developed into a technique for retrieving particle-intensive properties remotely. These problems were addressed in Chapters III and IV using a combination of statistical and optical models parameterized from in-water IOP measurements that allowed me to separate the influence of particle concentration and bulk characteristics on measured values of δ . Particle concentration had a surprisingly large influence on measurements of δ through the influence of multiple scattering and through shifts in the relative contributions of particulate and molecular scattering to the total return signal. Previous studies that have explored the response of polarized oceanographic lidar to changes in bulk particle properties have never been able to properly account for these effects, which can result in relationships developed between δ and bulk properties of the particle assemblage that may be difficult to generalize when intensive and extensive particle properties covary (Collister et al. 2018; Schulien et al. 2020). The modeling exercise presented here represents a useful framework for untangling the single and multiple scattering contributions to lidar measurements of δ and should be broadly applicable to a variety of lidar sampling geometries.

The linear depolarization measurements performed in Chapter IV improved our understanding of the nature of polarized light scattering by marine particles. $\mathbf{M}_{22}(\pi)$ was found to vary as a complex function of particle shape, size, and composition, where reductions in particle size resulted in a muted sensitivity of $\mathbf{M}_{22}(\pi)$ to shape and composition. The complexity of this response likely resulted from the fact that micron-sized marine particles span the transition region between

the Rayleigh and geometric scattering domains where changes in size result in large changes in the relative contributions of diffraction, refraction, and reflection to total scattering. These results will serve as important points of comparison with theoretical models of polarized light scattering, and suggest that future efforts to develop polarization-based lidar retrievals will require additional measurement constraints on the behavior of $\mathbf{M}_{22}(\pi)$ in natural waters and independent estimates of particle size and/or composition.

FUTURE DIRECTIONS

Several important gaps remain in our ability to link the range-resolved structure of lidar return signals to the vertical distribution of biogeochemically relevant materials in the ocean. The first category of outstanding work pertains to the development of techniques for connecting lidar measured properties $[\alpha, \beta(\pi), \delta]$ to classical IOPs and AOPs, that allow us to exploit established frameworks for relating classical inherent and apparent optical properties to biogeochemical properties of ocean particles. For instance, similar to the single-angle backscattering detectors used to measure b_{bp} , a conversion factor $[\chi_p(\pi)]$ is required to estimate b_{bp} from lidar measurements of $\beta(\pi)$. The variability of this conversion factor within the ocean has never been measured and its potential to contribute error to lidar estimates of b_{bp} and radiative transfer calculations parameterized from measurements of b_{bp} remains uncharacterized. Further research on the variability of the relationship between a versus K_d should also be conducted to characterize the uncertainties associated with neglecting the influence of ω_0 in lidar retrievals of K_d . This behavior will likely vary with instrument geometry and should be assessed for each instrument and deployment scheme separately.

Although optical oceanographers have developed several excellent frameworks for relating scalar IOPs to biogeochemical properties of the water column, there is still much work to be done to understand how polarized light scattering properties can be used to understand relevant biogeochemical properties. For advancing ocean lidar, this involves establishing relationships between $\mathbf{M}_{22}(\pi)$ and bulk properties of the particle assemblage in natural waters. Light scattering models that can resolve the complex relationship between particle shape, size, and composition are drastically needed, not only to explore the variability of $\mathbf{M}_{22}(\pi)$ in ocean particles, but also to develop techniques to simplify the information they contain. The study presented in Mukherjee et al. (2018) provides one potential technique for distilling the information contained in $\mathbf{M}_{22}(\pi)$ into a single representative index (the degree of optical non-sphericity), but the behavior of this property in natural waters and its relationship to useful biogeochemical properties has not been established. To establish such a relationship, model comparisons between non-spherical polarized light scattering models and in-water measurements of linear depolarization and bulk properties of natural particle assemblages are required. The large database of simultaneous lidar and *in situ* measurements that this effort would require can only be accomplished using shipboard lidar.

The success of passive satellite ocean color remote sensing has depended critically on the widespread availability of commercial instrumentation for measuring ocean color and in-water optical and biogeochemical properties simultaneously from ships, buoys, and moorings. Measurements made using these systems have been critical for performing optical closure studies required to test models of radiative transfer and for developing empirical and semi-analytical retrieval algorithms. As the ocean science community pushes toward the implementation of a spaceborne lidar for mapping the vertical distribution of marine ecosystems at a global scale, portable shipboard oceanographic lidar systems such as the one developed here will provide a

critical link between lidar-measured optical properties and classical IOPs and AOPs that can be related to the biogeochemical characteristics of marine particles. The ability to directly compare the complex response of the lidar signal to in-water measurements made at identical scales will be critical for testing and developing lidar radiative transfer models and for developing new lidar capabilities that can be scaled up to air- and spaceborne systems.

REFERENCES

- Aas, E. 1996. Refractive index of phytoplankton derived from its metabolite composition. *Journal of Plankton Research* **18**: 2223-2249.
- Acharya, Y., S. Sharma, and H. Chandra. 2004. Signal induced noise in PMT detection of lidar signals. *Measurement* **35**: 269-276.
- Allocca, D., M. London, T. Curran, B. Concannon, V. Contarino, J. Prentice, L. Mullen, and T. Kane. 2002. Ocean water clarity measurement using shipboard LIDAR systems, p. 106-114. *In* G. Gilbert and R. Frouin [eds.], *Ocean Optics: Remote Sensing and Underwater Imaging*. SPIE.
- Ansmann, A., I. Mattis, D. Müller, U. Wandinger, M. Radlach, D. Althausen, and R. Damoah. 2005. Ice formation in Saharan dust over central Europe observed with temperature/humidity/aerosol Raman lidar. *Journal of Geophysical Research: Atmospheres* **110**.
- Ansmann, A., M. Tesche, P. Seifert, D. Althausen, R. Engelmann, J. Fruntke, U. Wandinger, I. Mattis, and D. Müller. 2009. Evolution of the ice phase in tropical altocumulus: SAMUM lidar observations over Cape Verde. *Journal of Geophysical Research: Atmospheres* **114**.
- Balch, W., D. Drapeau, B. Bowler, E. Booth, J. Goes, A. Ashe, and J. Frye. 2004. A multi-year record of hydrographic and bio-optical properties in the Gulf of Maine: I. Spatial and temporal variability. *Progress in Oceanography* **63**: 57-98.
- Balch, W., H. R. Gordon, B. Bowler, D. Drapeau, and E. Booth. 2005. Calcium carbonate measurements in the surface global ocean based on Moderate-Resolution Imaging Spectroradiometer data. *Journal of Geophysical Research: Oceans* **110**.
- Balch, W. M., D. T. Drapeau, T. L. Cucci, R. D. Vaillancourt, K. A. Kilpatrick, and J. J. Fritz. 1999. Optical backscattering by calcifying algae: Separating the contribution of particulate inorganic and organic carbon fractions. *Journal of Geophysical Research: Oceans* **104**: 1541-1558.

- Beaufort, L. 2005. Weight estimates of coccoliths using the optical properties (birefringence) of calcite. *Micropaleontology* **51**: 289-297.
- Behrenfeld, M. J. 2010. Abandoning Sverdrup's critical depth hypothesis on phytoplankton blooms. *Ecology* **91**: 977-989.
- Behrenfeld, M. J., P. Gaube, A. Della Penna, R. T. O'Malley, W. J. Burt, Y. Hu, P. S. Bontempi, D. K. Steinberg, E. S. Boss, D. A. Siegel, C. A. Hostetler, P. D. Tortell, and S. C. Doney. 2019a. Global satellite-observed daily vertical migrations of ocean animals. *Nature* **576**: 257-261.
- Behrenfeld, M. J., Y. Hu, C. A. Hostetler, G. Dall'Olmo, S. D. Rodier, J. W. Hair, and C. R. Trepte. 2013. Space-based lidar measurements of global ocean carbon stocks. *Geophysical Research Letters* **40**: 4355-4360.
- Behrenfeld, M. J., Y. Hu, R. T. O'Malley, E. S. Boss, C. A. Hostetler, D. A. Siegel, J. L. Sarmiento, J. Schulien, J. W. Hair, and X. Lu. 2017. Annual boom–bust cycles of polar phytoplankton biomass revealed by space-based lidar. *Nature Geoscience* **10**: 118.
- Behrenfeld, M. J., R. H. Moore, C. A. Hostetler, J. Graff, P. Gaube, L. M. Russell, G. Chen, S. C. Doney, S. Giovannoni, and H. Liu. 2019b. The North Atlantic Aerosol and Marine Ecosystem Study (NAAMES): Science Motive and Mission Overview. *Frontiers in Marine Science* **6**.
- Bi, L., and P. Yang. 2015. Impact of calcification state on the inherent optical properties of *Emiliania huxleyi* coccoliths and coccolithophores. *Journal of Quantitative Spectroscopy and Radiative Transfer* **155**: 10-21.
- Bisson, K. M., E. Boss, P. J. Werdell, A. Ibrahim, and M. J. Behrenfeld. 2021. Particulate Backscattering in the Global Ocean: A Comparison of Independent Assessments. *Geophysical Research Letters* **48**: e2020GL090909.
- Bissonnette, L. R. 2005. Lidar and multiple scattering, p. 43-103. *Lidar*. Springer.
- Boss, E., W. Pegau, M. Lee, M. Twardowski, E. Shybanov, G. Korotaev, and F. Baratange. 2004. Particulate backscattering ratio at LEO 15 and its use to study particle composition and distribution. *Journal of Geophysical Research: Oceans* **109**.

- Bragg, W. L. 1924. The refractive indices of calcite and aragonite. *Proceedings of the Royal Society of London. Series A, Containing Papers of a Mathematical and Physical Character* **105**: 370-386.
- Burton, S., R. Ferrare, M. Vaughan, A. Omar, R. Rogers, C. Hostetler, and J. Hair. 2013. Aerosol classification from airborne HSRL and comparisons with the CALIPSO vertical feature mask. *Atmospheric Measurement Techniques* **6**: 1397-1412.
- Cairo, F., F. Congeduti, M. Poli, S. Centurioni, and G. Di Donfrancesco. 1996. A survey of the signal-induced noise in photomultiplier detection of wide dynamics luminous signals. *Review of scientific instruments* **67**: 3274-3280.
- Carswell, A., and S. Pal. 1980. Polarization anisotropy in lidar multiple scattering from clouds. *Applied optics* **19**: 4123-4126.
- Chaikovskaya, L. 2006. The problem of retrieval of depth profiles of scattering coefficient from polarization of pulsed lidar return. *SPIE*.
- Chami, M., A. Thirouard, and T. Harmel. 2014. POLVSM (Polarized Volume Scattering Meter) instrument: an innovative device to measure the directional and polarized scattering properties of hydrosols. *Optics express* **22**: 26403-26428.
- Chase, A. S., D. Z. Chase, and A. F. Chase. 2017. LiDAR for archaeological research and the study of historical landscapes, p. 89-100. *Sensing the Past*. Springer.
- Churnside, J., and P. Donaghay. 2009. Thin scattering layers observed by airborne lidar. *ICS Journal of Marine Science* **66**: 778-789.
- Churnside, J., H, and L. Ostrovsky. 2005. Lidar observation of a strongly nonlinear internal wave train in the Gulf of Alaska. *International Journal of Remote Sensing* **26**: 167-177.
- Churnside, J. H. 2008. Polarization effects on oceanographic lidar. *Optics express* **16**: 1196-1207.
- Churnside, J. H., E. D. Brown, S. Parker-Stetter, J. K. Horne, G. L. Hunt, N. Hillgruber, M. F. Sigler, and J. J. Vollenweider. 2011. Airborne remote sensing of a biological hot spot in the southeastern Bering Sea. *Remote Sensing* **3**: 621-637.

- Churnside, J. H., and R. D. Marchbanks. 2015. Subsurface plankton layers in the Arctic Ocean. *Geophysical Research Letters* **42**: 4896-4902.
- Churnside, J. H., and R. D. Marchbanks. 2017. Inversion of oceanographic profiling lidars by a perturbation to a linear regression. *Applied optics* **56**: 5228-5233.
- Churnside, J. H., and R. E. Thorne. 2005. Comparison of airborne lidar measurements with 420 kHz echo-sounder measurements of zooplankton. *Applied Optics* **44**: 5504-5511.
- Codiga, D., W. Balch, S. Gallagher, P. Holthus, H. Paerl, J. Sharp, and R. Wilson. 2012. Ferry-based Sampling for Cost-Effective, Long-Term, Repeat Transect Multidisciplinary Observation Products in Coastal and Estuarine Ecosystems. Community White Paper, IOOS Summit, Herndon, VA (November, 2012).
- Collister, B. L., R. C. Zimmerman, V. J. Hill, C. I. Sukenik, and W. M. Balch. 2020. Polarized lidar and ocean particles: insights from a mesoscale coccolithophore bloom. *Applied Optics* **59**: 4650-4662.
- Collister, B. L., R. C. Zimmerman, C. I. Sukenik, V. J. Hill, and W. M. Balch. 2018. Remote sensing of optical characteristics and particle distributions of the upper ocean using shipboard lidar. *Remote Sensing of Environment* **215**: 85-96.
- Coops, N. C., T. Hilker, M. A. Wulder, B. St-Onge, G. Newnham, A. Siggins, and J. T. Trofymow. 2007. Estimating canopy structure of Douglas-fir forest stands from discrete-return LiDAR. *Trees* **21**: 295.
- Cross, J., C. Mordy, H. Tabisola, C. Meinig, E. Cokelet, and P. Stabeno. 2015. Innovative technology development for Arctic exploration, p. 1-8. OCEANS'15 MTS/IEEE Washington. IEEE.
- Dabrowska, D., O. Muñoz, F. Moreno, T. Nousiainen, E. Zubko, and A. Marra. 2013. Experimental and simulated scattering matrices of small calcite particles at 647 nm. *Journal of Quantitative Spectroscopy and Radiative Transfer* **124**: 62-78.

- David, G., B. Thomas, T. Nousiainen, A. Miffré, and P. Rairoux. 2013. Retrieving simulated volcanic, desert dust and sea-salt particle properties from two/three-component particle mixtures using UV-VIS polarization lidar and T matrix. *Atmospheric Chemistry & Physics* **13**.
- Davis, K. J., N. Gamage, C. Hagelberg, C. Kiemle, D. Lenschow, and P. Sullivan. 2000. An objective method for deriving atmospheric structure from airborne lidar observations. *Journal of Atmospheric and Oceanic Technology* **17**: 1455-1468.
- Dionisi, D., V. E. Brando, G. Volpe, S. Colella, and R. Santoleri. 2020. Seasonal distributions of ocean particulate optical properties from spaceborne lidar measurements in Mediterranean and Black sea. *Remote Sensing of Environment* **247**: 111889.
- Doney, S. C., R. Anderson, J. Bishop, K. Caldeira, C. Carlson, M.-E. Carr, R. Feely, M. Hood, C. H. MBL, and R. Jahnke. 2004. Ocean carbon and climate change (OCCC): An implementation strategy for US ocean carbon research. UCAR, Boulder, CO.
- Esselborn, M., M. Wirth, A. Fix, B. Weinzierl, K. Rasp, M. Tesche, and A. Petzold. 2009. Spatial distribution and optical properties of Saharan dust observed by airborne high spectral resolution lidar during SAMUM 2006. *Tellus B: Chemical and Physical Meteorology* **61**: 131-143.
- Fry, E., and K. Voss. 1985. Measurement of the Mueller matrix for phytoplankton. *Limnology and Oceanography* **30**: 1322-1326.
- Garver, S. A., and D. A. Siegel. 1997. Inherent optical property inversion of ocean color spectra and its biogeochemical interpretation: 1. Time series from the Sargasso Sea. *Journal of Geophysical Research: Oceans* **102**: 18607-18625.
- Gimmestad, G. G. 2008. Reexamination of depolarization in lidar measurements. *Applied optics* **47**: 3795-3802.
- Goldstein, J. I., D. E. Newbury, J. R. Michael, N. W. Ritchie, J. H. J. Scott, and D. C. Joy. 2017. *Scanning electron microscopy and X-ray microanalysis*. Springer.
- Gordon, H. R. 1982. Interpretation of airborne oceanic lidar: effects of multiple scattering. *Applied optics* **21**: 2996-3001.

- Gordon, H. R., G. C. Boynton, W. M. Balch, S. B. Groom, D. S. Harbour, and T. J. Smyth. 2001. Retrieval of coccolithophore calcite concentration from SeaWiFS imagery. *Geophysical Research Letters* **28**: 1587-1590.
- Gordon, H. R., and T. Du. 2001. Light scattering by nonspherical particles: application to coccoliths detached from *Emiliana huxleyi*. *Limnology and Oceanography* **46**: 1438-1454.
- Gordon, H. R., and W. McCluney. 1975. Estimation of the depth of sunlight penetration in the sea for remote sensing. *Applied optics* **14**: 413-416.
- Guay, C. K., and J. K. Bishop. 2002. A rapid birefringence method for measuring suspended CaCO₃ concentrations in seawater. *Deep Sea Research Part I: Oceanographic Research Papers* **49**: 197-210.
- Guillard, R., and P. Hargraves. 1993. *Stichochrysis immobilis* is a diatom, not a chrysophyte. *Phycologia* **32**: 234-236.
- Harding, L. W., A. Magnuson, and M. E. Mallonee. 2005. SeaWiFS retrievals of chlorophyll in Chesapeake Bay and the mid-Atlantic bight. *Estuarine, Coastal and Shelf Science* **62**: 75-94.
- Hewes, C. D., and O. Holm-Hansen. 1983. A method for recovering nanoplankton from filters for identification with the microscope: The filter-transfer-freeze (FTF) technique 1. *Limnology and Oceanography* **28**: 389-394.
- Hill, V. J., and R. C. Zimmerman. 2010. Estimates of primary production by remote sensing in the Arctic Ocean: Assessment of accuracy with passive and active sensors. *Deep Sea Research Part I: Oceanographic Research Papers* **57**: 1243-1254.
- Hoge, F., C. Wright, W. Krabill, R. Buntzen, G. Gilbert, R. Swift, J. Yungel, and R. Berry. 1988. Airborne lidar detection of subsurface oceanic scattering layers. *Appl. Opt.* **27**: 39969-33977.
- Hostetler, C. A., M. J. Behrenfeld, Y. Hu, J. W. Hair, and J. A. Schulien. 2018. Spaceborne lidar in the study of marine systems. *Annual review of marine science* **10**: 121-147.

- Hu, L., X. Zhang, Y. Xiong, D. J. Gray, and M.-X. He. 2020. Variability of relationship between the volume scattering function at 180° and the backscattering coefficient for aquatic particles. *Applied optics* **59**: C31-C41.
- Hu, Y. 2007. Depolarization ratio–effective lidar ratio relation: Theoretical basis for space lidar cloud phase discrimination. *Geophysical research letters* **34**.
- Hu, Y., M. Vaughan, Z. Liu, B. Lin, P. Yang, D. Flittner, B. Hunt, R. Kuehn, J. Huang, and D. Wu. 2007. The depolarization-attenuated backscatter relation: CALIPSO lidar measurements vs. theory. *Optics Express* **15**: 5327-5332.
- Hutt, D. L., L. R. Bissonnette, and L. Durand. 1994. Multiple field of view lidar returns from atmospheric aerosols. *Applied optics* **33**: 2338-2348.
- Ibrahim, A., A. Gilerson, J. Chowdhary, and S. Ahmed. 2016. Retrieval of macro- and micro-physical properties of oceanic hydrosols from polarimetric observations. *Remote Sensing of Environment* **186**: 548-566.
- Jamet, C., A. Ibrahim, Z. Ahmad, F. Angelini, M. Babin, M. J. Behrenfeld, E. Boss, B. Cairns, J. Churnside, and J. Chowdhary. 2019. Going Beyond Standard Ocean Color Observations: Lidar and Polarimetry. *Frontiers in Marine Science* **6**: 251.
- Järvinen, E., O. Kemppinen, T. Nousiainen, T. Kociok, O. Möhler, T. Leisner, and M. Schnaiter. 2016. Laboratory investigations of mineral dust near-backscattering depolarization ratios. *Journal of quantitative spectroscopy & radiative transfer* **178**: 192-208.
- Johnson, D., A. Weidemann, R. Arnone, and C. Davis. 2001. Chesapeake Bay outflow plume and coastal upwelling events: physical and optical properties.
- Jung, J., S.-J. Hong, H.-B. Kim, G. Kim, M. Lee, S. Shin, S. Lee, D.-J. Kim, C.-G. Lee, and Y. Park. 2018. Label-free non-invasive quantitative measurement of lipid contents in individual microalgal cells using refractive index tomography. *Scientific Reports* **8**: 6524.
- Kirk, J. 1994. *Light and Photosynthesis in the Sea*, 2nd ed. Cambridge University Press.

- Knap, A., A. Michaels, A. Close, H. Ducklow, and A. Dickson. 1996. Protocols for the joint global ocean flux study (JGOFS) core measurements.
- Kokhanovsky, A. A. 2003. Parameterization of the Mueller matrix of oceanic waters. *Journal of Geophysical Research: Oceans* **108**.
- Kouzoubov, A., M. J. Brennan, J. C. Thomas, and R. H. Abbot. 1999. Monte Carlo simulations of the influence of particle nonsphericity on remote sensing of ocean water. *Journal of Geophysical Research: Atmospheres* **104**: 31731-31737.
- Kovalev, V., and W. Eichinger. 2004. *Elastic Lidar. Theory, Practice and Analysis Methods*. Wiley-Interscience.
- Lacour, L., R. Larouche, and M. Babin. 2020. In situ evaluation of spaceborne CALIOP lidar measurements of the upper-ocean particle backscattering coefficient. *Optics Express* **28**: 26989-26999.
- Lee, J., J. Churnside, R. Marchbanks, P. Donaghay, and J. Sullivan. 2013. Oceanographic lidar profiles compared with estimates from *in situ* optical measurements. *Appl. Opt.* **52**: 786-794.
- Lee, Z. P., M. Darecki, K. L. Carder, C. O. Davis, D. Stramski, and W. J. Rhea. 2005. Diffuse attenuation coefficient of downwelling irradiance: An evaluation of remote sensing methods. *Journal of Geophysical Research: Oceans* **110**.
- Leyland, B., S. Boussiba, and I. Khozin-Goldberg. 2020. A review of diatom lipid droplets. *Biology* **9**: 38.
- Linge Johnsen, S. A., J. Bollmann, C. Gebuehr, and J. O. Herrle. 2019. Relationship between coccolith length and thickness in the coccolithophore species *Emiliana huxleyi* and *Gephyrocapsa oceanica*. *PloS one* **14**: e0220725.
- Liu, D., P. Xu, Y. Zhou, W. Chen, B. Han, X. Zhu, Y. He, Z. Mao, C. Le, and P. Chen. 2019a. Lidar Remote Sensing of Seawater Optical Properties: Experiment and Monte Carlo Simulation. *IEEE Transactions on Geoscience and Remote Sensing* **57**: 9489-9498.

- Liu, Q., X. Cui, W. Chen, C. Liu, J. Bai, Y. Zhang, Y. Zhou, Z. Liu, P. Xu, and H. Che. 2019b. A semianalytic Monte Carlo radiative transfer model for polarized oceanic lidar: experiment-based comparisons and multiple scattering effects analyses. *Journal of Quantitative Spectroscopy and Radiative Transfer* **237**: 106638.
- Liu, Q., D. Liu, J. Bai, Y. Zhang, Y. Zhou, P. Xu, Z. Liu, S. Chen, H. Che, and L. Wu. 2018. Relationship between the effective attenuation coefficient of spaceborne lidar signal and the IOPs of seawater. *Optics express* **26**: 30278-30291.
- Lofflus, K., M. Quinby-Hunt, A. Hunt, F. Livolant, and M. Maestre. 1992. Light scattering by *Prorocentrum micans*: a new method and results. *Applied optics* **31**: 2924-2931.
- Lu, X., Y. Hu, C. Trepte, S. Zeng, and J. H. Churnside. 2014. Ocean subsurface studies with the CALIPSO spaceborne lidar. *Journal of Geophysical Research: Oceans* **119**: 4305-4317.
- McKee, D., A. Cunningham, and A. Dudek. 2007. Optical water type discrimination and tuning remote sensing band-ratio algorithms: Application to retrieval of chlorophyll and $K_d(490)$ in the Irish and Celtic Seas. *Estuarine, Coastal and Shelf Science* **73**: 827-834.
- Mehri, T., O. Kemppinen, G. David, H. Lindqvist, J. Tyynelä, T. Nousiainen, P. Rairoux, and A. Miffré. 2018. Investigating the size, shape and surface roughness dependence of polarization lidars with light-scattering computations on real mineral dust particles: Application to dust particles' external mixtures and dust mass concentration retrievals. *Atmospheric Research* **203**: 44-61.
- Miffré, A., D. Cholleton, and P. Rairoux. 2019. Laboratory evaluation of the scattering matrix elements of mineral dust particles from 176.0° up to 180.0° -exact backscattering angle. *Journal of Quantitative Spectroscopy and Radiative Transfer* **222-223**: 45-59.
- Miller, S. D., and G. L. Stephens. 1999. Multiple scattering effects in the lidar pulse stretching problem. *Journal of Geophysical Research: Atmospheres* **104**: 22205-22219.
- Mishchenko, M. I., L. D. Travis, and A. A. Lacis. 2002. Scattering, absorption, and emission of light by small particles. Cambridge university press.

- Mobley, C. D. 1989. A numerical model for the computation of radiance distributions in natural waters with wind-roughened surfaces. *Limnology and Oceanography* **34**: 1473-1483.
- Montes, M. A., J. Churnside, Z. Lee, R. Gould, R. Arnone, and A. Weidemann. 2011. Relationships between water attenuation coefficients derived from active and passive remote sensing: a case study from two coastal environments. *Applied Optics* **50**: 2990-2999.
- Moore, T. S., J. H. Churnside, J. M. Sullivan, M. S. Twardowski, A. R. Nayak, M. N. McFarland, N. D. Stockley, R. W. Gould, T. H. Johengen, and S. A. Ruberg. 2019. Vertical distributions of blooming cyanobacteria populations in a freshwater lake from LIDAR observations. *Remote Sensing of Environment* **225**: 347-367.
- Mukherjee, L., P.-W. Zhai, Y. Hu, and D. M. Winker. 2018. Single scattering properties of non-spherical hydrosols modeled by spheroids. *Optics express* **26**: A124-A135.
- Munk, W. 2000. Oceanography before, and after, the advent of satellites. Elsevier Oceanography Series **63**: 1-4.
- Noel, V., and K. Sassen. 2005. Study of planar ice crystal orientations in ice clouds from scanning polarization lidar observations. *Journal of Applied Meteorology* **44**: 653-664.
- Nousiainen, T., and K. Kandler. 2015. Light scattering by atmospheric mineral dust particles, p. 3-52. *Light Scattering Reviews* 9. Springer.
- Nousiainen, T., E. Zubko, J. V. Niemi, K. Kupiainen, M. Lehtinen, K. Muinonen, and G. Videen. 2009. Single-scattering modeling of thin, birefringent mineral-dust flakes using the discrete-dipole approximation. *Journal of Geophysical Research: Atmospheres* **114**.
- O'Reilly, J. E., S. Maritorena, B. G. Mitchell, D. A. Siegel, K. L. Carder, S. A. Garver, M. Kahru, and C. McClain. 1998. Ocean color chlorophyll algorithms for SeaWiFS. *Journal of Geophysical Research: Oceans* **103**: 24937-24953.
- Olson, R., E. Zettler, and O. Anderson. 1989. Discrimination of eukaryotic phytoplankton cell types from light scatter and autofluorescence properties measured by flow cytometry. *Cytometry: The Journal of the International Society for Analytical Cytology* **10**: 636-643.

- Pettifer, R. 1975. Signal induced noise in lidar experiments. *Journal of Atmospheric and Terrestrial Physics* **37**: 669-673.
- Phinney, D., and C. Yentsch. 1985. A novel phytoplankton chlorophyll technique: toward automated analysis. *Journal of Plankton Research* **7**: 633-642.
- Platt, C. 1981. Remote sounding of high clouds. III: Monte Carlo calculations of multiple-scattered lidar returns. *Journal of the atmospheric sciences* **38**: 156-167.
- Poole, L. R., D. D. Venable, and J. W. Campbell. 1981. Semianalytic Monte Carlo radiative transfer model for oceanographic lidar systems. *Applied optics* **20**: 3653-3656.
- Pope, R., and E. Fry. 1997. Absorption spectrum (380-700 nm) of pure water. II. Integrating cavity measurements. *Appl. Opt.* **36**: 8710-8723.
- Poulton, A. J., A. Charalampopoulou, J. R. Young, G. A. Tarran, M. I. Lucas, and G. D. Quartly. 2010. Coccolithophore dynamics in non-bloom conditions during late summer in the central Iceland Basin (July-August 2007). *Limnology and Oceanography* **55**: 1601-1613.
- Quinby-Hunt, M., A. Hunt, K. Lofftus, and D. Shapiro. 1989. Polarized-light scattering studies of marine *Chlorella*. *Limnology and Oceanography* **34**: 1587-1600.
- Raković, M. J., G. W. Kattawar, M. Mehrübeoğlu, B. D. Cameron, L. V. Wang, S. Rastegar, and G. L. Côté. 1999. Light backscattering polarization patterns from turbid media: theory and experiment. *Applied optics* **38**: 3399-3408.
- Roddewig, M. R., N. J. Pust, J. H. Churnside, and J. A. Shaw. 2017. Dual-polarization airborne lidar for freshwater fisheries management and research. *Optical Engineering* **56**: 031221.
- Roy, G., L. Bissonnette, C. Bastille, and G. Vallée. 1999. Retrieval of droplet-size density distribution from multiple-field-of-view cross-polarized lidar signals: theory and experimental validation. *Applied optics* **38**: 5202-5211.
- Sanz, J. M., C. Extremiana, and J. Saiz. 2013. Comprehensive polarimetric analysis of Spectralon white reflectance standard in a wide visible range. *Applied optics* **52**: 6051-6062.

- Sassen, K. 2005. Polarization in Lidar. Lidar: range-resolved optical remote sensing of the atmosphere. Springer.
- Sassen, K., and G. C. Dodd. 1982. Lidar crossover function and misalignment effects. *Applied optics* **21**: 3162-3165.
- Sassen, K., and R. L. Petrilla. 1986. Lidar depolarization from multiple scattering in marine stratus clouds. *Applied optics* **25**: 1450-1459.
- Sathyendranath, S., L. Prieur, and A. Morel. 1989. A three-component model of ocean colour and its application to remote sensing of phytoplankton pigments in coastal waters. *International Journal of Remote Sensing* **10**: 1373-1394.
- Schofield, O., T. Bergmann, P. Bissett, J. F. Grassle, D. B. Haidvogel, J. Kohut, M. Moline, and S. M. Glenn. 2002. The long-term ecosystem observatory: an integrated coastal observatory. *Oceanic Engineering, IEEE Journal of* **27**: 146-154.
- Schulien, J. A., M. J. Behrenfeld, J. W. Hair, C. A. Hostetler, and M. S. Twardowski. 2017. Vertically-resolved phytoplankton carbon and net primary production from a high spectral resolution lidar. *Optics Express* **25**: 13577-13587.
- Schulien, J. A., A. Della Penna, P. Gaube, A. P. Chase, N. Haëntjens, J. R. Graff, J. W. Hair, C. A. Hostetler, A. J. Scarino, and E. S. Boss. 2020. Shifts in Phytoplankton Community Structure Across an Anticyclonic Eddy Revealed From High Spectral Resolution Lidar Scattering Measurements. *Frontiers in Marine Science* **7**: 493.
- Shaw, J. A., J. H. Churnside, J. J. Wilson, N. E. Lerner, R. R. Tiensvold, P. E. Bigelow, and T. M. Koel. 2008. Airborne lidar mapping of invasive lake trout in Yellowstone Lake, p. 905-908. *Proceedings of the 24th International Laser Radar Conference*. Citeseer.
- Sheldon, R., A. Prakash, and W. Sutcliffe Jr. 1972. The size distribution of particles in the ocean 1. *Limnology and Oceanography* **17**: 327-340.
- Siegel, D. A., K. O. Buesseler, M. J. Behrenfeld, C. R. Benitez-Nelson, E. Boss, M. A. Brzezinski, A. Burd, C. A. Carlson, E. A. D'Asaro, and S. C. Doney. 2016. Prediction of the export and fate of

- global ocean net primary production: the EXPORTS science plan. *Frontiers in Marine Science* **3**: 22.
- Sun, B., G. W. Kattawar, P. Yang, M. S. Twardowski, and J. M. Sullivan. 2016. Simulation of the scattering properties of a chain-forming triangular prism oceanic diatom. *Journal of Quantitative Spectroscopy and Radiative Transfer* **178**: 390-399.
- Svensen, Ø., J. J. Stamnes, M. Kildemo, L. M. S. Aas, S. R. Erga, and Ø. Frette. 2011. Mueller matrix measurements of algae with different shape and size distributions. *Applied optics* **50**: 5149-5157.
- Takano, Y., and K.-N. Liou. 1989. Solar radiative transfer in cirrus clouds. Part I: Single-scattering and optical properties of hexagonal ice crystals. *Journal of the Atmospheric Sciences* **46**: 3-19.
- Twardowski, M., E. Boss, J. MacDonald, W. Pegau, A. Barnard, and J. Zaneveld. 2001. A model for estimating bulk refractive index from the optical backscattering ratio and the implications for understanding particle composition in Case I and Case II waters. *J. Geophys. Res. - Oceans* **105**: 14129-14142.
- van de Hulst, H. C. 1957. *Light scattering by small particles*.
- Van Der Woerd, H. J., and R. Pasterkamp. 2008. HYDROPT: A fast and flexible method to retrieve chlorophyll-a from multispectral satellite observations of optically complex coastal waters. *Remote Sensing of Environment* **112**: 1795-1807.
- Vasilkov, A. P., Y. A. Goldin, B. A. Gureev, F. E. Hoge, R. N. Swift, and C. W. Wright. 2001. Airborne polarized lidar detection of scattering layers in the ocean. *Applied Optics* **40**: 4353-4364.
- Vaughan, M. A., K. A. Powell, R. E. Kuehn, S. A. Young, D. M. Winker, C. A. Hostetler, W. H. Hunt, Z. Liu, M. J. McGill, and B. J. Getzewich. 2009. Fully Automated Detection of Cloud and Aerosol Layers in the CALIPSO Lidar Measurements. *Journal of Atmospheric & Oceanic Technology* **26**: 2034-2050.
- von Dassow, P., G. van den Engh, D. Iglesias-Rodriguez, and J. R. Gittins. 2012. Calcification state of coccolithophores can be assessed by light scatter depolarization measurements with flow cytometry. *Journal of Plankton Research* **34**: 1011-1027.

- Voss, K. J., W. M. Balch, and K. A. Kilpatrick. 1998. Scattering and attenuation properties of *Emiliania huxleyi* cells and their detached coccoliths. *Limnology and Oceanography* **43**: 870-876.
- Voss, K. J., and E. S. Fry. 1984. Measurement of the Mueller matrix for ocean water. *Applied optics* **23**: 4427-4439.
- Vu, T. T., M. Matsuoka, and F. Yamazaki. 2004. LIDAR-based change detection of buildings in dense urban areas, p. 3413-3416. *IGARSS 2004. 2004 IEEE International Geoscience and Remote Sensing Symposium*. IEEE.
- Walker, R. E., and J. W. McLean. 1999. Lidar equations for turbid media with pulse stretching. *Applied Optics* **38**: 2384-2397.
- Wang, C., Q. Li, Y. Liu, G. Wu, P. Liu, and X. Ding. 2015. A comparison of waveform processing algorithms for single-wavelength LiDAR bathymetry. *ISPRS Journal of Photogrammetry and Remote Sensing* **101**: 22-35.
- Weston, K., L. Fernand, D. Mills, R. Delahunty, and J. Brown. 2005. Primary production in the deep chlorophyll maximum of the central North Sea. *Journal of Plankton Research* **27**: 909-922.
- Whitmire, A. L., W. S. Pegau, L. Karp-Boss, E. Boss, and T. J. Cowles. 2010. Spectral backscattering properties of marine phytoplankton cultures. *Optics Express* **18**: 15073-15093.
- Williamson, C. K., and R. J. De Young. 2000. Method for the reduction of signal-induced noise in photomultiplier tubes. *Applied optics* **39**: 1973-1979.
- Witkowski, K., T. Król, A. Zielirinki, and E. Kuteń. 1998. A light-scattering matrix for unicellular marine phytoplankton. *Limnology and Oceanography* **43**: 859-869.
- Young, J. R., S. A. Davis, P. R. Bown, and S. Mann. 1999. Coccolith Ultrastructure and Biomineralisation. *Journal of Structural Biology* **126**: 195-215.
- Zege, E. P., and L. I. Chaikovskaya. 1999. Polarization of multiply scattered lidar return from clouds and ocean water. *JOSA A* **16**: 1430-1438.

- Zhai, P. W., Y. Hu, C. R. Trepte, D. M. Winker, D. B. Josset, P. L. Lucker, and G. W. Kattawar. 2013. Inherent optical properties of the coccolithophore: *Emiliana huxleyi*. *Opt Express* **21**: 17625-17638.
- Zhai, S., M. Twardowski, J. D. Hedley, M. McFarland, A. R. Nayak, and T. Moore. 2020. Optical backscattering and linear polarization properties of the colony forming cyanobacterium *Microcystis*. *Optics Express* **28**: 37149-37166.
- Zhang, X., L. Hu, and M.-X. He. 2009. Scattering by pure seawater: effect of salinity. *Optics Express* **17**: 5698-5710.
- Zhou, W., G. Wang, Z. Sun, W. Cao, Z. Xu, S. Hu, and J. Zhao. 2012. Variations in the optical scattering properties of phytoplankton cultures. *Optics Express* **20**: 11189-11206.
- Zhou, Y., W. Chen, X. Cui, A. Malinka, Q. Liu, B. Han, X. Wang, W. Zhuo, H. Che, and Q. Song. 2019. Validation of the Analytical Model of Oceanic Lidar Returns: Comparisons with Monte Carlo Simulations and Experimental Results. *Remote Sensing* **11**: 1870.
- Zhou, Y., D. Liu, P. Xu, C. Liu, J. Bai, L. Yang, Z. Cheng, P. Tang, Y. Zhang, and L. Su. 2017. Retrieving the seawater volume scattering function at the 180° scattering angle with a high-spectral-resolution lidar. *Optics express* **25**: 11813-11826.
- Zimmerman, R., C. Sukenik, and V. Hill. 2013. Using oceanographic LIDAR to determine the vertical bio-optical structure of the upper ocean, p. 471-487. *In* J. Watson and O. Zielinski [eds.], *Subsea Optics and Imaging*. Woodhead.

VITA

Brian Leigh Collister

Department of Ocean and Earth Sciences
Old Dominion University
4600 Elkhorn Ave.
Norfolk, VA 23529-0276

EDUCATION

PhD, Oceanography, Old Dominion University, 2021
MS, Ocean and Earth Science, Old Dominion University, 2019
BS, Ocean and Earth Science (Chemistry minor), Old Dominion University, 2016

PUBLICATIONS

Collister, B. L., R. C. Zimmerman, V. J. Hill, C. I. Sukenik, and W. M. Balch. 2020. Polarized lidar and ocean particles: insights from a mesoscale coccolithophore bloom. *Applied Optics* **59**: 4650-4662.
Collister, B. L., R. C. Zimmerman, C. I. Sukenik, V. J. Hill, and W. M. Balch. 2018. Remote sensing of optical characteristics and particle distributions of the upper ocean using shipboard lidar. *Remote Sensing of Environment* **215**: 85-96.

PUBLICATIONS IN PREP

Collister, B. L., R. C. Zimmerman, V. J. Hill, C. I. Sukenik, and W. M. Balch. 2021. The Influence of Particle Concentration and Composition on Polarized Oceanographic Lidar Measurements. For submission to *Applied Optics*

AWARDS

2021 NASA Postdoctoral Program (NPP) Fellowship
2019 & 2020 Virginia Space Grant Graduate Student Research Fellowship
2018 Selected to Participate in the University of Washington *Oceanhackweek* event
2017 Neil and Susan Kelley Endowed Scholarship
2016 Old Dominion University Undergraduate Research Travel Award
2016 Old Dominion University Undergraduate Research Grant